
IAHR
AIRH
Supported by
Spain Water
and IWHR, China
IAHR
2017
37th IAHR
WORLD CONGRESS
13-18 August, 2017
Kuala Lumpur, Malaysia
SUSTAINABLE (RENEWABLE) ENERGY

EXPERIMENTAL STUDY OF THE EFFECTS OF A HORIZONTAL AXIS TIDAL STREAM TURBINE ON HYDRODYNAMIC PROCESSES

YALING CHEN(1), BINLIANG LIN(2) & JIE LIN(3)

(1,2,3)State Key Laboratory of Hydro-science and Engineering, Tsinghua University, Beijing 100084, China
kmlgya@126.com

ABSTRACT

As well as estimating the extractable potential of tidal stream energy, it is also important to analyse the influence of tidal stream turbine on hydrodynamic processes. Studies of the characteristics of turbine wake have been conducted by both physical experiments and numerical models. However, detailed experimental data were still limited to reveal the whole evolution process of the wake structure. A detailed experimental study on the effects of a horizontal axis turbine with three blades was conducted in a recirculating water flume. Acoustic Doppler Velocimeter was employed to measure the time varying velocities across the full width of the open flume, correspondingly the three-dimensional mean velocities and turbulent flow fields were obtained. Experimental results indicate that clear velocity deficit is observed in the wake flow, while velocity change is not significant upstream, and velocity deficit can be negligible over one diameter upstream. Immediately downstream, the maximum velocity deficit occurs at the wake core due to a lower Tip Speed Ratio of turbine rotor. With increasing downstream distance, the wake strip enlarges slightly with less diffusion in the transverse direction, while the wake zone shifts towards to water surface in the vertical direction. Furthermore, the wake turbulence of turbine is strong and anisotropy, this will impact on the behavior of other turbines located downstream in turbine arrays.

Keywords: Tidal stream turbine; velocity measurements; velocity deficit; turbulence fields.

1 INTRODUCTION

With the advantages of predictability, the clean renewable tidal energy has shown a great potential for development throughout the world (Lewis et al., 2015). The kinetic energy of tidal currents can be converted into electrical power by tidal stream turbine (Fernandez-Rodriguez et al., 2014). Indeed, the natural tidal flow fields are disturbed as the tidal turbines are installed in the flow, which has an impact on power extraction in turn (Chen et al., 2014; 2015).

Computational Fluid Dynamics (CFD) models have been employed to investigate the wake structure behind tidal current turbine (Pinon et al., 2012; Mycek et al., 2013). Lam et al. (2014; 2015) predicted the lateral velocity distribution based on Gaussian probability distribution. Morris et al. (2016) investigated the swirl characteristics of a turbine wake and pointed that the wake swirl was slightly affected by the blade number of turbine rotor. Shives and Crawford (2016) adapted the actuator disc-RANS simulation by including the turbulent kinetic energy to investigate the wake turbulence resulting from the breakdown of trailed vortices from blade tips.

Myers and Bahaj (2012) conducted experiments using a disc rotor to investigate the development of wake structure of a horizontal axis turbine. The results showed that the recovery rate of the wake was significantly affected by the ambient flow turbulence. Nguyen et al. (2016) compared the CFD simulation results to the experimental data measured behind a disc. It was found that the wake velocity deficit was well simulated in the far wake, while wake turbulence intensity was underestimated in the near wake. However, the wake rotation behind a horizontal axis turbine rotor cannot be shown by the experiments using a disc.

Stallard et al. (2013) used a scaled model turbine to investigate the wake recovery and lateral distribution along turbine axes. With detailed velocity measurement, Stallard et al. (2015) showed the characteristics of wake rotation within 2RD behind turbine rotor. Mycek et al. (2014a; 2014b) showed the distribution of the velocity deficit and wake turbulence on a plane across turbine centre within 10RD downstream. It was found that the wake shape and length were considerably influenced by the ambient turbulence intensity. Tedds et al. (2014) carried out experiments to study wake structure by employing a model turbine with Tip Speed Ratio (TSR) being 6.15. The largest velocity deficit behind turbine occurred at the tip of blades and the anisotropic wake turbulence was observed in the near due to swirl effects. Morandi et al. (2016) used a scaled model turbine to investigate the influence of TSR on the wake characteristics of the velocity deficit and wake turbulence at 0.125RD downstream.

The effects of tidal current energy extraction on wake structure have been investigated using both CFD models and experiments. However, the detailed experimental data are still limited to reveal the whole evolution process of the wake structure. In addition, the effects of tidal currents energy extraction on upstream

flow lack a good understanding. In the current study, experiments were carried out in an open flume to investigate the effects of tidal energy extraction by a horizontal axis turbine on the flow fields. The detailed velocities were measured at sixteen cross sections from 1RD upstream to 20RD downstream of the turbine rotor. The experimental results can provide reliable data for numerical model simulations to improve the understanding of the influence of horizontal axis turbines, and the study is also a foundation of theory to optimize the configuration of turbine array for power extraction in the next stage.

2 EXPERIMENTAL SET-UP

2.1 Flume configuration

The experiment was conducted in a re-circulating water flume, as shown in Fig.1. A porous plate with rectangular grids was fitted at the inlet to remove large scale eddies from the tank. A transition section was used to generate a smooth connection to the test section and to increase the flow velocity. The testing section of the flume was 14.4m long by 0.8m wide and 0.8m deep, with the water depth being 0.54m. The model turbine was located 10m from flume inlet and 10.4m from the flume outlet. A similar porous plate was located at the outlet to reduce water level oscillations downstream.

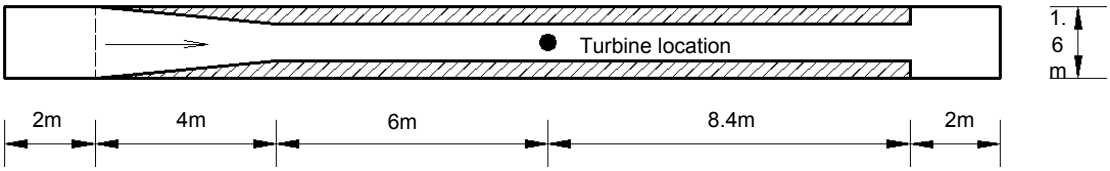

Figure1. The layout of re-circulating water flume

2.2 Flow velocity measurement

Time-varying velocities were measured by an Acoustic Doppler Velocimeter (ADV). The ADV was fixed on a platform that freely moves along the cross section of the flume. Velocity measurement were carried out at sixteen transverse sections from upstream to downstream of the turbine rotor, the longitudinal spacing between cross sections increased downstream. On each cross section, 435 velocity samples were collected, with lateral spacing and vertical spacing of 2.5cm and 3cm, respectively. Time-varying velocity data were recorded for 60s at each measurement location.

2.3 Ambient flow

Before tidal turbine rotor was installed, flow velocity at two cross-section (X= -4RD and 4RD) were measured to understand the spatial variation of the mean flow velocity and flow turbulence at the test area. Turbulence intensity is defined relative to the mean longitudinal velocity as follows:

$$I_x = \frac{\sqrt{\frac{1}{N}\sum_{i=1}^{N}(u_i - \overline{u_i})(u_i - \overline{u_i})}}{U} \times 100\% \qquad [1]$$

Where U=0.59m/s is mean flow velocity over the swept area.

The Reynolds shear stress Rxy is given by:

$$R_{xy} = \frac{\sqrt{\left|\frac{1}{N}\sum_{i=1}^{N}(u_i - \overline{u_i})(v_i - \overline{v_i})\right|}}{U} \qquad [2]$$

As seen in Fig. 2a, the distribution of time-averaged velocity on the cross section was not uniform, with lower velocity near the flume walls. While slight increase in the time-averaged velocity with the longitudinal distance was observed.

Turbulence intensity on the cross section was not constant, with stronger turbulence intensity close to channel walls (shown in Fig. 2b). Average turbulence intensity was about 2% in the middle channel. As a consequence, the recovery rate of turbine wake is expected to be slightly influenced by the ambient turbulence intensity

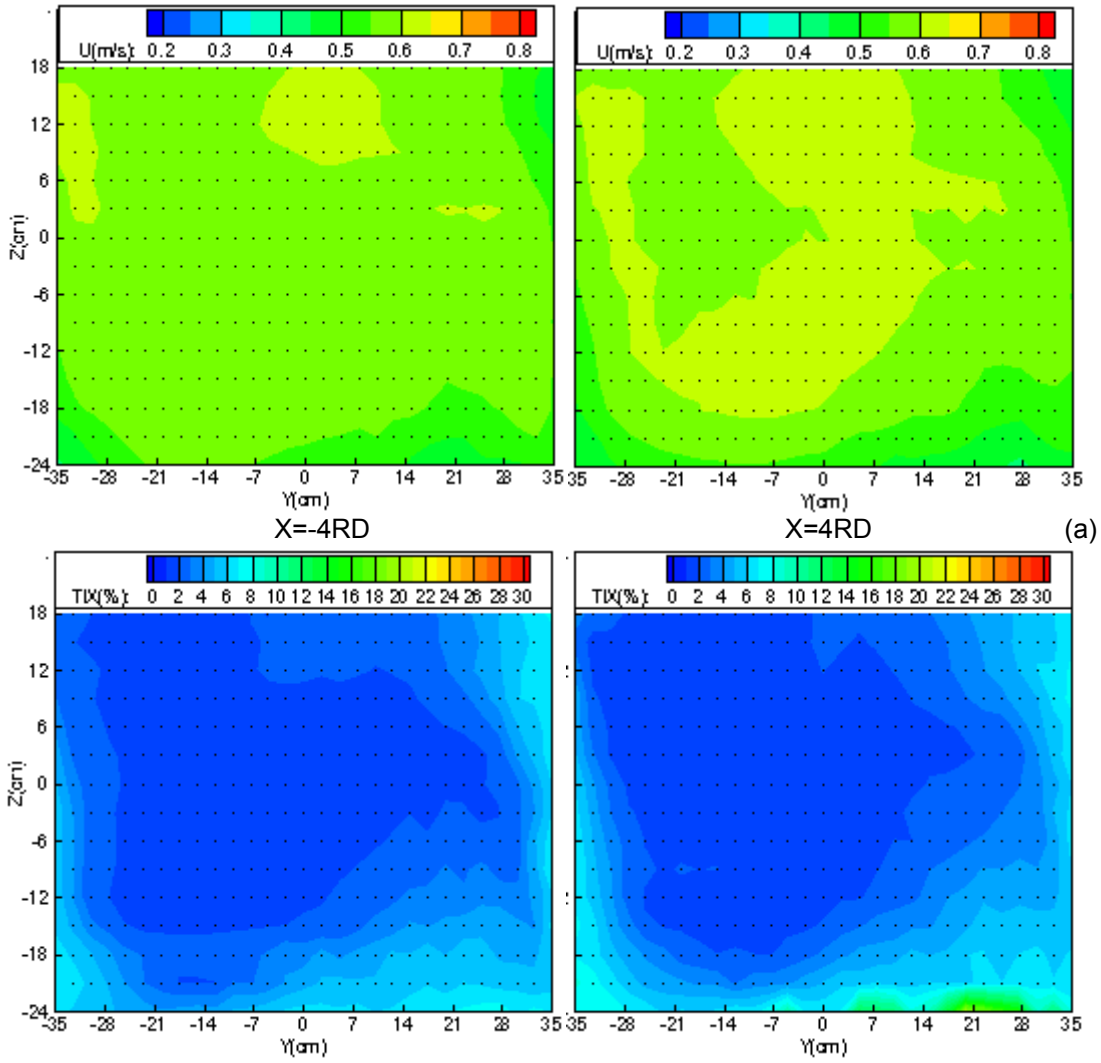

Figure 2. Profiles of (a) the time-averaged velocity and (b) turbulence intensity at upstream (-4RD) and downstream (4RD) of the turbine rotor

2.4 Turbine performance

A three-bladed horizontal axis turbine was employed to extract the kinetic energy of the flow passing through turbine rotor, with diameter of 0.3m. The turbine rotor was fixed on the centreline of the channel, and the hub height of the rotor was 0.29m above the channel floor. The blockage ratio of the turbine rotor was approximately 16.4%, and the TSR was about 3.47± 2.98%. In the study, a dynamic strain gauge was used to measure the thrust on turbine rotor, each record was collected for a 60s duration at 200Hz. The average thrust on turbine rotor was 5.12N as the mean velocity on the swept area was 0.59m/s, and the thrust coefficient was about 0.41.

3 FLOW FIELDS

A significant decrease of flow velocity was observed downstream, as seen in Fig. 3. The maximize wake velocity deficit occurred at wake centre (1RD downstream), with the minimum velocity about 0.29m/s. The wake deficit behind turbine rotor decayed with a depletion rate along longitudinal distance, while the lateral distribution of turbine wake approached approximately symmetry and spread slightly towards outsides (Fig.3a). An increase of flow velocity occurred at two sides of turbine rotor after 1RD downstream, with velocity above 0.6m/s. Due to flume walls limitation, the appearance of turbine rotor decreased the area for flow passing through and increases flow velocity. While no significant increase of flow velocity was observed in the vertical plane due to the existence of the free water surface (Fig.3 b). A smaller decrease of flow velocity appeared within 1RD upstream, and the influence of turbine rotor on water flow was limited. Although the blockage ration was high (16.4%), the changes of flow velocity were negligible at the cross section of turbine rotor. In the vertical direction, there were two wake cores behind both turbine rotor and the stanchion. By 3RD downstream, the two wake cores merged into a single wake. It means that turbine stanchion has a significant influence on the near wake.

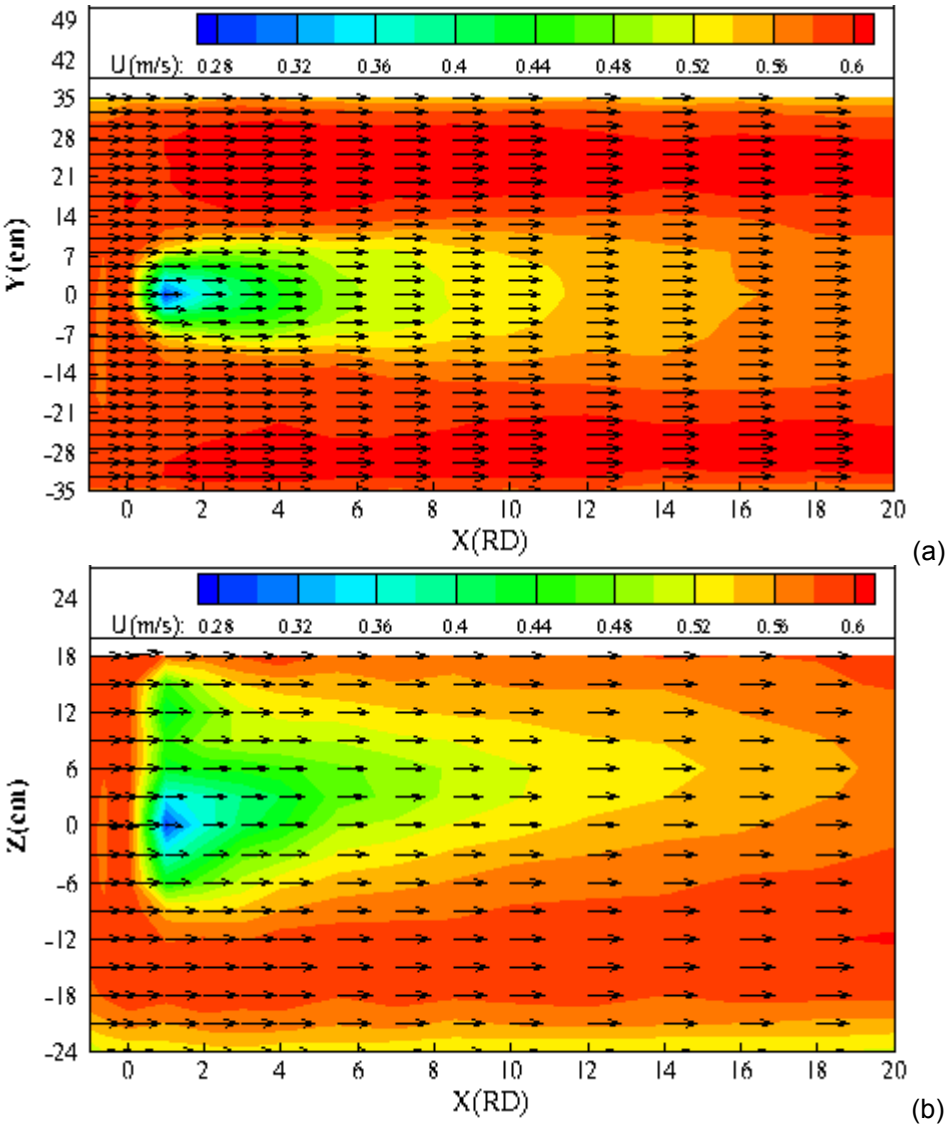

Figure 3. Velocity distribution at (a) xoy plane and (b) xoz plane over the range -1RD (upstream) ~20RD (downstream), the colour variance represents the magnitude of flow velocity and the arrowhead represents the velocity vector

4 TRUBULENCE FIELDS

4.1 Turbulence intensity

Turbulence fields over the range -1RD~20RD are shown in Fig.4. Immediately downstream, a band of turbulence was observed and the strongest turbulence was located at the wake core, the maximum turbulence intensity was about 25% at 1RD. With the distance increasing, the turbulence intensity decreased and enlarged slightly towards the two sides in the *xoy* plane (see Fig.4a). Compared with the turbulence intensity of ambient flow (Fig.2), the recovery distance of wake turbulence was longer than 20RD downstream. Turbulence intensity was not strengthened upstream of turbine rotor, and local turbulence intensity increased around turbine rotor tips at 0RD. In the vertical direction, two peaks of turbulence intensity occurred immediately downstream, the maximum turbulence intensity was up to 36.34%, close to water surface (shown in Fig.4b). The two peaks reduced rapidly within 2RD downstream, and further recovery of turbulence intensity was gradual afterwards, with the turbulence intensity of 6% by 20RD downstream.

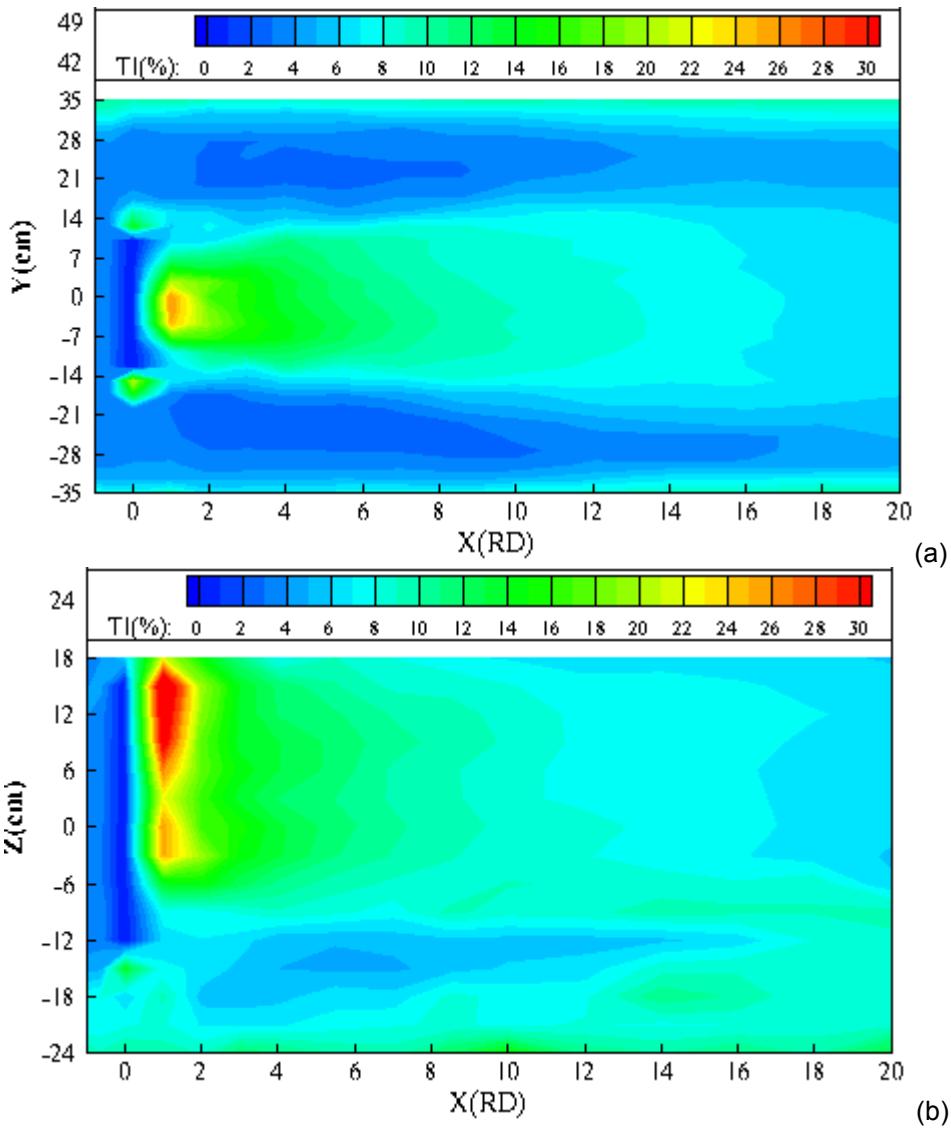

Figure 4. Turbulence intensity at (a) xoy plane and (b) xoz plane over the range -1RD (upstream) ~20RD (downstream)

4.2 Reynolds shear stress

As shown in Fig.5a, the distribution of Reynolds shear stress was approximately symmetrical about turbine central axis in the xoy plane. The layer of Reynolds shear stress was thin (almost half of the diameter of turbine rotor) immediately downstream, with two peaks of Reynolds shear stress located at the root of rotor blade. The layer of Reynolds shear stress expanded outwards with distance increasing downstream, and the layer was almost up to two times of rotor diameter by 20RD downstream without merging into a single layer of shear stress. Similar to turbulence intensity, the distribution of Reynolds shear stress was non-uniform in the vertical direction. Two peaks of shear stress appear immediately downstream, the maximum value of Reynolds shear number was about 0.11, located at Z=9cm, where the turbulence fields were influenced by both the turbine rotor and stanchion. The Reynolds shear stress below turbine rotor centre decreased to 0.025 within 4RD downstream, and the layers of shear stress merged into a single layer further downstream. Generally, the Reynolds shear stress upstream was very small. It seems that turbine rotor has no significant influence on the upstream turbulence fields.

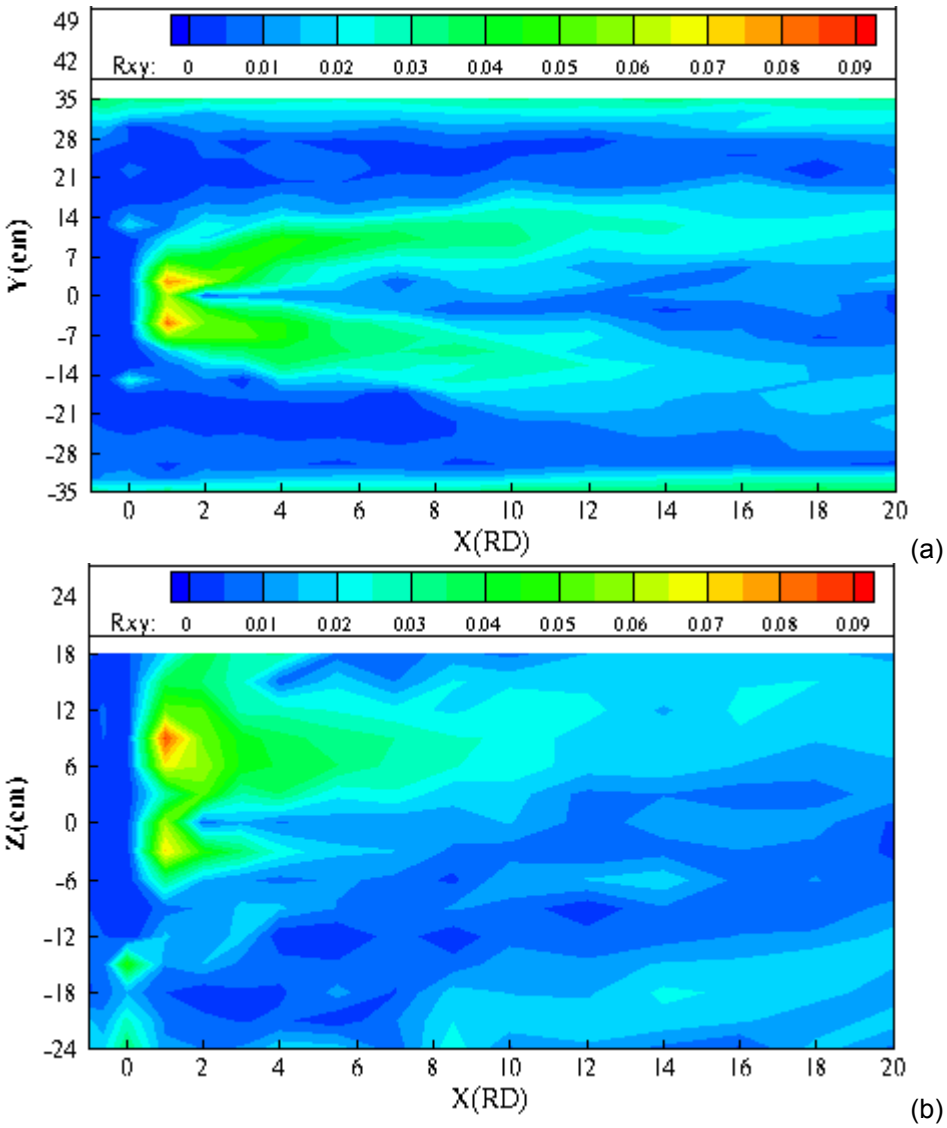

Figure 5. Reynolds shear stress at (a) xoy plane and (b) xoz plane over the range -1RD (upstream) ~20RD (downstream)

5 CONCLUSIONS

The influence of a horizontal axis turbine on hydrodynamics has been investigated experimentally in an open channel. The detailed three-dimensional velocities have been measured by ADV at sixteen cross sections over the range -1RD ~ 20RD. The structures of both flow field and turbulence field induced by the presence of turbine are revealed. Immediately downstream, a significant velocity deficit is caused by both kinetic energy extraction and blockage effects of turbine rotor. The wake band was approximately symmetrical and decayed with slightly expansion in lateral direction along longitudinal distance. Due to the restriction of channel walls, the mean flow velocity increased at two outsides of turbine rotor, with no visible increase of flow velocity along water depth. The turbulence field is significantly influenced by both turbine rotor and stanchion, especially in the near wake. The strongest turbulence induced by the combination effects of turbine rotor and stanchion was located above rotor central axis. Generally, the turbine has very small influence on flow and turbulence fields upstream.

ACKNOWLEDGEMENTS

This study was funded by the National High-tech Research and Development Program in China (863 Torch Program, 2012AA052602).

REFERENCES

Chen, Y., Lin, B. & Lin, J. (2014). Modelling Tidal Current Energy Extraction in Large Area Using a Three-Dimensional Estuary Model. *Computers & Geosciences*, 72, 76-83.

Chen, Y., Lin, B., Lin, J. & Wang, S. (2015). Effects of Stream Array Configuration on Tidal Current Energy Extraction near an Island. *Computers & Geosciences*, 77, 20-28.

Fernandez-Rodriguez, E., Stallard, T. & Stansby, P. (2014). Experimental Study of Extreme Thrust on a Tidal Stream Rotor Due to Turbulent Flow and with Opposing Waves. *Journal of Fluids and Structures*, 51, 354-361.

Lewis, M., Neill, S. & Robins, P. (2015). Resource Assessment for Future Generations of Tidal-Stream Energy Arrays. *Energy*, 83, 403-415.

Morandi, B., Felice, F. & Costanzo, M. (2016). Experimental Investigation of the Near Wake of a Horizontal Axis Tidal Current Turbine. *International Journal of Marine Energy*, 14,229-247.

Morris, C., O'Doherty, D. & Mason-Jones, A. (2016). Evaluation of the Swirl Characteristics of a Tidal Stream Turbine Wake. *International Journal of Marine Energy*, 14, 198-214.

Mycek, P., Gaurier, B., Germain, G., Pinon, G. & Rivoalen, E. (2013). Numerical and Experimental Study of the Interaction between Two Marine Current Turbines. *International Journal of Marine Energy*, 1, 70-83.

Mycek, P., Gaurier, B., Germain, G., Pinon, G. & Rivoalen, E. (2014a). Experimental Study of the Turbulence Intensity Effects on Marine Current Turbines Behavior. Part I: One Single Turbine. *Renewable Energy*, 66,729-746.

Mycek, P., Gaurier, B., Germain, G., Pinon, G. & Rivoalen, E. (2014b). Experimental Study of the Turbulence Intensity Effects on Marine Current Turbines Behavior. Part Ⅱ: Two Interacting Turbines. *Renewable Energy*, 68, 876-892.

Myers, L. & Bahaj, A. (2012). An Experimental Investigation Simulating Flow Effects in First Generation Marine Current Energy Converter Arrays. *Renewable Energy*, 37, 28-36.

Nguyen, V., Guillou, S. & Thiebot, J. (2016). Modelling Turbulence with an Actuator Disk Representing a Tidal Turbine. *Renewable Energy*, 97, 625-35

Pinon, G., Mycek, P., Germain, G. & Rivoalen, E. (2012). Numerical Simulation of the Wake of Marine Current Turbines with a Particle Method. *Renewable Energy*, 46, 111-126.

Shives, M. & Crawford, C. (2016). Adapted Two-Equation Turbulence Closures for Actuator Disk RANS Simulations of Wind and Tidal Turbine Wakes. *Renewable Energy*, 92, 273-92.

Stallard, T., Collings, R. & Feng, T. (2013). Interactions between Tidal Turbine Wakes: Experimental Study of a Group of Three-Bladed Rotors. *Philosophical Transactions of Royal Society A*, 14, 1-13.

Stallard, T., Feng, T. & Stansby, P.K. (2015). Experimental Study of the Mean Wake of a Tidal Stream Rotor in a Shallow Turbulent Flow. *Journal of Fluids and Structures*, 54, 235-246.

Proceedings of the 37th IAHR World Congress
August 13 – 18, 2017, Kuala Lumpur, Malaysia

AIR DEMAND OF HIGH-HEAD BOTTOM OUTLETS

BENJAMIN HOHERMUTH[(1)]

[(1)] Laboratory of Hydraulics, Hydrology and Glaciology (VAW), ETH Zurich, Zurich, Switzerland
hohermuth@vaw.baug.ethz.ch

ABSTRACT

Bottom outlets are key safety devices of high-head dams to control the reservoir water level. The high-speed free-surface flow downstream of the bottom outlet gate leads to considerable air entrainment and air transport. To avoid negative pressures at the bottom outlet and consequently prevent problems with gate vibrations, cavitation and flow chocking, a sufficient amount of air has to be supplied through an aeration chamber. Existing approaches to predict the air demand of bottom outlets show a large scatter and the knowledge on the transition from free-surface to fully pressurized flow is still scarce. Consequently, current design guidelines do not allow a coherent design. The goal of the present study is to improve the existing design guidelines by means of a systematic physical model investigation. The energy heads in the model are significantly larger than in previous studies and thus closer to prototype conditions. Furthermore, the effect of the aeration system, the tunnel length and the energy head on the air demand are quantified. The results show that the Froude number at the vena contracta has the largest effect on air demand. Short tunnels and large loss coefficients of the aeration system result in lower air demand values. Moderate tunnel fillings cause maximal air demand while both small and large fillings reduce the air demand. A new empirical relation for the air demand is presented considering all investigated parameters. The minimal negative pressures in the tunnel are calculated by applying the Bernoulli equation to the aeration system. The air pressure development along the tunnel is shown and the influence of the air flow from the downstream tunnel end is discussed.

Keywords: Air demand; bottom outlet; cavitation; hydraulic structures; two-phase flow.

1 INTRODUCTION

Bottom outlets are a key safety feature of high-head dams. Their main purpose is the regulation and – if required – a fast drawdown of the reservoir water level in case of floods, imminent danger, structural damage of the dam or maintenance works. Additional purposes include flood diversion or sediment flushing to prevent reservoir sedimentation.

The high energy heads at the gate lead to a high-speed free-surface flow in the bottom outlet tunnel with flow velocities up to some 50 m/s for high dams. The high flow velocities and turbulence levels lead to considerable air entrainment and air transport, possibly resulting in negative pressures at the bottom outlet. This causes problems with gate vibrations, cavitation and flow chocking associated with a rapid and unsteady transition from free-surface to pressurized flow. These problems can be mitigated by sufficient air supply via an aeration chamber. Despite the importance of bottom outlet structures, design recommendations and researches on high-speed tunnel flows are surprisingly scarce. Available recommendations for bottom outlet design are mostly qualitative and only state the following general requirements: (i) smooth flow for full gate opening, (ii) excellent performance for all flows under partial gate opening and (iii) effective energy dissipation at the terminal outlet (e.g. Vischer and Hager, 1998).

The first systematic study on air entrainment in closed conduits was presented by Kalinske and Robertson (1943). Since then, various field and model studies were performed (Table 1). Most of these studies related the air demand β, which is defined as $\beta = Q_{a,o}/Q_w$, with $Q_{a,o}$= air flow rate through the aeration chamber, Q_w= water discharge, to the Froude number at the vena contracta, $F_c = U_c / (gh_c)^{0.5}$, with U_c = flow velocity and h_c = flow depth at the vena contracta (subscript c), respectively. The large scatter of the existing approaches (Fig. 1) can be partly explained by different flow patterns (Sharma, 1973). Additional effects of both the aeration system and the tunnel geometry were partially considered in newer approaches (Table 1). Four contributions should be highlighted: (i) the extensive prototype measurements in the 1950s and 60s of the US Army Corps of Engineers (USCE), thus providing a basis for future investigations. (ii) Sharma (1973) distinguished six flow patterns in bottom outlets and developed an enveloping curve for the air demand of spray and free-surface flow. This is the up-to-date method of choice for the preliminary design of bottom outlet aeration systems. (iii) Rabben (1984) systematically investigated and described the influence of the aeration system on the air demand, leading to an improved understanding of the air and water flow interactions. (iv) Speerli (1999) performed an extensive model study including the measurement of two-phase air-water flow features. In his comprehensive analysis, he included the effects of the aeration system and tunnel length on the air demand. However, due to experimental limitations his results were limited to small gate openings.

Table 1. Overview of existing air demand equations, a= gate opening, A_a = air vent cross-sectional area, A_t = total tunnel area d/s of gate, A_c=flow area at the vena contracta, F_o=approach flow Froude number, h_t = tunnel height d/s of gate, L= tunnel length d/s of gate, U_i= flow velocity for the onset of aeration, U_c= flow velocity at vena contracta, W = tunnel width d/s of gate, σ_w = surface tension, η_w= dynamic viscosity, ρ_w, ρ_a= water and air density, ζ = air vent loss coefficient.

Authors	Equation	Flow pattern	Comment
Kalinske and Robertson (1943), Campbell and Guyton (1953)	$\beta = 0.0066(F_o - 1)^{1.4}$	Hydraulic jump	Model tests: L = 9.75 m, circular pipe, d = 0.15 m
	$\beta = 0.04(F_c - 1)^{0.85}$	Hydraulic jump at large gate openings	Prototype data from USCE, Denison, Hulah, Norfork, Pine Flat and Tygart dam
Wunderlich (1963)	$\beta = \frac{A_c^2}{A_t^2}\left(\frac{A_t}{A_c} - 1\right)\ A_t = h_t W, A_c = h_c W$	Free-surface flow	Prototype data of Lumiei (Dettmers, 1953), Mauvoisin (Schilling, 1963) and Norfork dam (USCE, 1954)
USCE (1964)	$\beta = 0.03\left(F_c - 1\right)^{1.06}$	Hydraulic jump / pressurized flow for large gate opening	Prototype data, additional data from Denison and Norfork dam
Levin (1965)	$\beta = 0.06\left(F_c - 1\right)$	Full flowing tunnel, smooth profile transition	Data from authors above (not specified)
Wisner (1967)	$\beta = 0.033\left(F_c - 1\right)^{1.4}$	Spray flow	Model tests from applied projects and prototype data from Campbell and Guyton (1953), Guyton (1958), Mura et al. (1959)
	$\beta = 0.024\left(F_c - 1\right)^{1.4}$	Free-surface flow	
	$\beta = 0.014\left(F_c - 1\right)^{1.4}$	Hydraulic jump (F_c> 8)	
	$\beta = 0.04\left(F_c - 1\right)^{0.85}$	Hydraulic jump (F_c< 8)	
Lynse and Guttormsen (1971)	$\beta = 1.2\left(\frac{A_t}{A_c}\right)^{0.2} - 1$	Hydraulic jump / pressurized flow for large gate opening	Two prototypes in Norway, data from USCE (1964)
Sharma (1973)	$\beta = 0.2F_c$	Spray flow	Model tests: $H_{E,max}$ = 20 m w.c. (at Q = 0 l/s), rectangular tunnel, L = 8 m, W = 0.1 m, h_t = 0.15 m Prototype data from authors cited above
	$\beta = 0.09F_c$	Free-surface flow	
	$\beta = 0.0066\left(F_c - 1\right)^{1.4}$	Hydraulic jump	
Ouazar (1983)	$\beta = 0.017\frac{\rho_a}{\rho_w}\frac{\eta_w(U_c - U_i)}{\sigma}\frac{A_c}{A_t}$	Free-surface flow	Model tests with reduced static pressure, rectangular channel, W = 0.1 m, h_t = 0.15 m
	$\beta = 0.012\left(F_c - 1\right)^{1.135}$	Hydraulic jump	Prototype data
Rabben (1984)	$\beta = \left(\frac{A_a^*}{A_t}\right)F_c,\quad A_a^* = \left(\frac{A_a}{\zeta + 1}\right)^{0.5}$	Spray flow	Model tests: $H_{E,max}$ = 20 m w.c. (at Q = 0 l/s), rectangular tunnel, L = 4 m, W = 0.15 m, h_t = 0.32 m, scale family (data for largest model)
	$\beta = 0.94\left(\frac{A_a^*}{A_t}\right)^{0.9} F_c^{0.62}$	Free-surface flow	
	$\beta = 0.019\left(\frac{A_a^*}{A_t}\right)^{0.099} F_c^{0.969}$	Hydraulic jump	
Speerli (1999)	$Q_a = 0.022H_E\left(\frac{L}{h_t}\right)^{0.167}\left(\frac{a}{a_{max}}\right)^{0.5}\left(gW^3\right)^{0.5}\zeta^{-0.43}$	Spray and free-surface flow	Model tests: $H_{E,max}$ = 25 m w.c. (at Q = 245 l/s), rectangular tunnel, L = 20 m, W = 0.3 m, h_t = 0.45 m

The present research project aims to investigate the influence of the aeration system and the tunnel length on the air demand and the air pressures for all possible flow types in bottom outlets.1

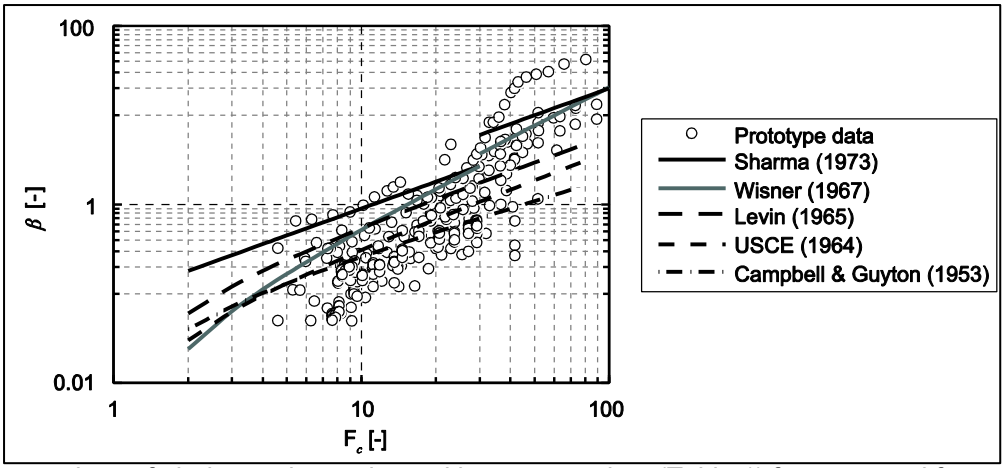

Figure 1. Comparison of air demand equations with prototype data (Table 1) for spray and free-surface flow. F_c = 30 is taken as the onset of spray flow.

2 PHYSICAL MODEL STUDY

2.1 Model and instrumentation

A physical bottom outlet model was built at the Laboratory of Hydraulics, Hydrology and Glaciology (VAW) at ETH Zurich (Fig. 2a).Two high-head pumps were connected to the gate chamber of the model. The resulting maximum energy head at the gate is H_E = 30 m w.c. at a discharge of $Q_w \approx$ 600 l/s. A sharp crested gate without gate slots was installed to control the discharge (Fig. 2b). The rectangular gate section is 0.2 m wide, 0.25 m high and extends to h_t = 0.3 m for the downstream tunnel section. The horizontal bottom outlet tunnel has a maximum length of L = 20.6 m. Detachable elements allow variation of the tunnel length in sections of 2 m intervals. The aeration chamber 0.29 m downstream of the gate was connected to a circular air vent of diameter d = 0.15 m. The air vent can be throttled with an orifice plate to vary the loss coefficient ζ of the whole aeration system. A similar air vent was located at the tunnel end to determine whether the air flows into or out of the tunnel. All channel walls consisted of PVC or acrylic glass with a hydraulic roughness of k = 0.003 mm (Bollrich, 2007).

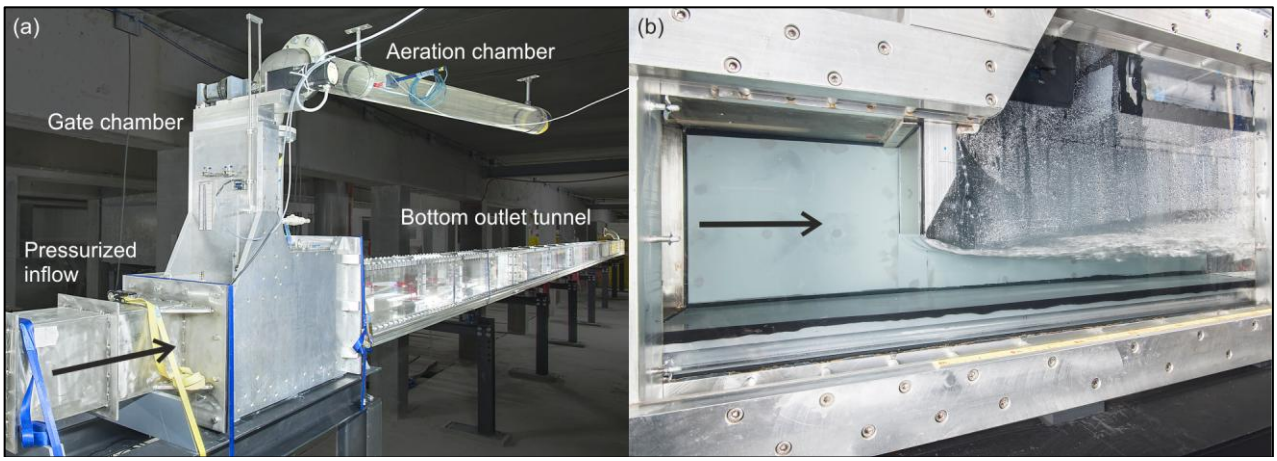

Figure 2. (a) Physical bottom outlet model at VAW, (b) gate chamber.

The water discharge, Q_w was measured with an inductive flow meter with an accuracy of ± 0.5% of measurement value and± 0.4 l/s absolute error. The air flow velocity in the air vent of the aeration chamber(subscript o) and at the tunnel end(subscript u) were measured with Schiltknecht vane anemometers of ± 3% accuracy. From the measured velocity, the flow rates $Q_{a,o}$ and $Q_{a,u}$ were computed, assuming a logarithmic velocity profile and using the corresponding cross-sectional areas. The cross section above the air-water mixture not occupied by the flow was blocked with a manually operated gate at the tunnel end. Consequently, the air had to be supplied through the second air vent which allowed precise measurements of $Q_{a,u}$. (Fig. 3). A total of 40 relative pressure sensors of type Keller PR23-S with a measurement range of ±100 mbar and an accuracy of ± 1 mbar were installed along the tunnel center line at the invert and at the soffit to

measure both the water and air pressures, respectively. The sensors were placed in intervals of 1 m along the first 12 m of the tunnel and 2 m intervals along the last 6 m, respectively. Additional sensors were installed in the gate and aeration chambers.

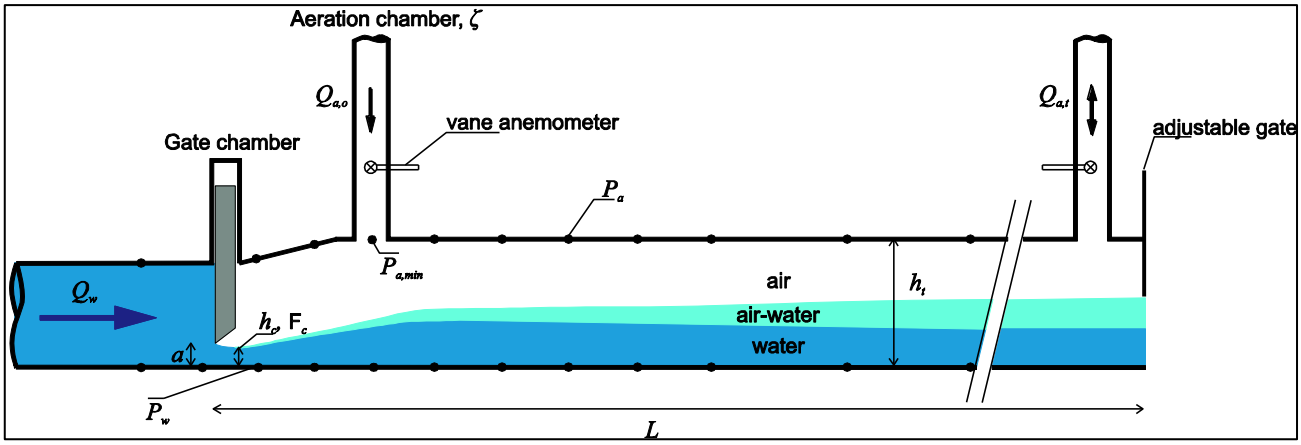

Figure 3. A sketch of the physical model, Q_w=water discharge, $Q_{a,o}$= air flow rate through aeration chamber, $Q_{a,u}$= air flow rate from/out of tunnel end, P_a= air pressure, P_w= water pressure, a= gate opening, h_t= tunnel height and L= tunnel length.

2.2 Test program

The following parameters were varied in the present study: energy head H_E, relative gate opening a/a_{max}, air vent loss coefficient, ζ and tunnel length, L. For a given tunnel length and air vent loss coefficient the relative gate opening was increased from 0.1 to 1 in steps of 0.1.For each gate opening, energy heads from 5 to 30 m w.c. in steps of 5 m w.c. were tested. Five air vent loss coefficients, ζ = 0.7, 2.9 10.1, 24 and 37 were tested. All parameter combinations were tested for tunnel lengths of L = 20.6, 12.6 and 6.6 m. Combinations of H_E>20 m w.c. and ζ > 10 could not be measured due to strong flow pulsations. Additionally, measurements with H_E> 25 m w.c. were not possible for L = 6.6 m due to splashing. The aeration chamber was drowned when a/a_{max}> 0.8 for all tested parameter combinations. This resulted in a total of 462 test runs.

3 RESULTS AND DISCUSSIONS

3.1 Flow pattern and basic observations

The flow detached at the sharp gate lip and shock waves were formed on both sides of the tunnel (Fig. 2b). These shock waves are induced by corner vortices upstream of the gate (Roth and Hager, 1999) and their heights increased with decreasing relative gate opening. For small relative gate openings and high energy heads, the shock waves generated an intense spray. The shock waves decayed some 5-6 m downstream of the gate. After the vena contracta, a backwater curve was observed in the air-water mixture. Flow aeration started shortly after the gate due to the high flow velocities and turbulence levels.

Spray flow was observed when a/a_{max}<0.2.However, due to the absence of gate slots and smaller absolute velocities, the spray was less pronounced than that in a prototype. For 0.2 ≤a/a_{max}< 0.6, free-surface flow occurred for all tested parameter configurations. At higher relative gate openings of 0.6 ≤a/a_{max} ≤ 0.8, the downstream end of the tunnel was almost full, corresponding to foamy flow according to Sharma (1973). A hydraulic jump with subsequent fully pressurized flow was observed once the mixture surface reached the tunnel soffit for a/a_{max}> 0.8. The hydraulic jump travelled upstream and resulted in fully pressurized flow with a drowned aeration chamber. The tunnel outlet was not submerged for all tests and a hydraulic jump with subsequent free-surface flow could not be observed in the model.

Throttling the aeration chamber (i.e. large loss coefficients ζ) led to unsteady flow pulsations, especially for large energy heads. Kelvin-Helmholtz instabilities were formed at the air-water interface and the mixture surface was sucked towards the tunnel soffit leading to foamy slugs, which completely filled the tunnel cross-section (Fig. 4a). Only one slug was formed at a time. These slugs travelled downstream along the entire tunnel and completely blocked aeration from the tunnel end (Fig. 4b-d). Stratified free-surface flow was observed behind these slugs (Fig. 4e, f). The slugs leaded to a large negative pressure in the tunnel section upstream of the slug. For large energy heads 20 m w.c. ≤H_E≤ 30 m w.c., these pressure drops were below the measurement limit of −1 m w.c. (approximately -100 mbar) in the model. In prototypes with higher H_E, slug flow can lead to severe cavitation damage and flow chocking and should be avoided.

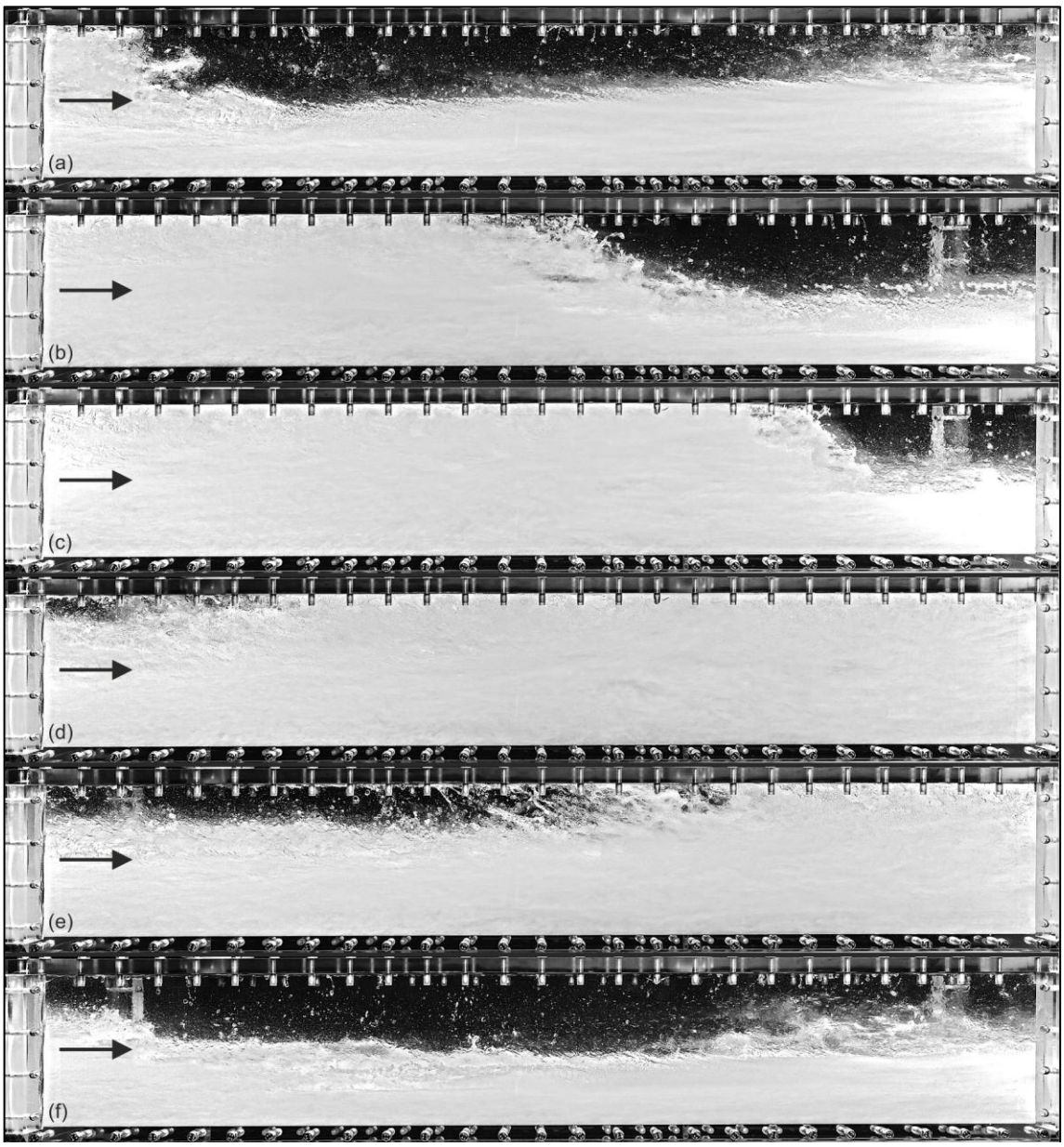

Figure 4. Photo sequence (a) to (f) of a foamy slug flowing from left to right for H_E = 25 m w.c., L = 20.6m, a/a_{max} = 0.4, ζ = 24. Photos were taken 10 m downstream of the gate (side view).

3.2 Air demand

3.2.1 Air flow through aeration chamber

The air flow rate through the aeration chamber $Q_{a,o}$ increased with increasing energy head H_E(Fig. 5). The maximum air flow rates can be observed for moderate relative gate openings, $0.4 \leq a/a_{max} \leq 0.6$.The maximum was shifted towards smaller relative gate openings for increasing H_E and decreasing L (Fig. 5a, d, g). The increase of $Q_{a,o}$ for very small relative gate openings $a/a_{max} \approx 0.05$ was caused by spray flow (Fig. 5a, b). At larger relative gate openings, the air flow rate decreased, especially for large energy heads. This is due to the transition to foamy flow with the tunnel almost full at the tunnel end. Therefore, the cross sectional area above the air-water mixture was small and less air can be transported above the mixture surface. Increasing the air vent loss coefficients decreased the air flow rate through the aeration chamber $Q_{a,o}$(Fig. 5a-c). Decreasing the tunnel length L also decreased $Q_{a,o}$. For short tunnels with increasing ζ, the air supply from the tunnel end increased.

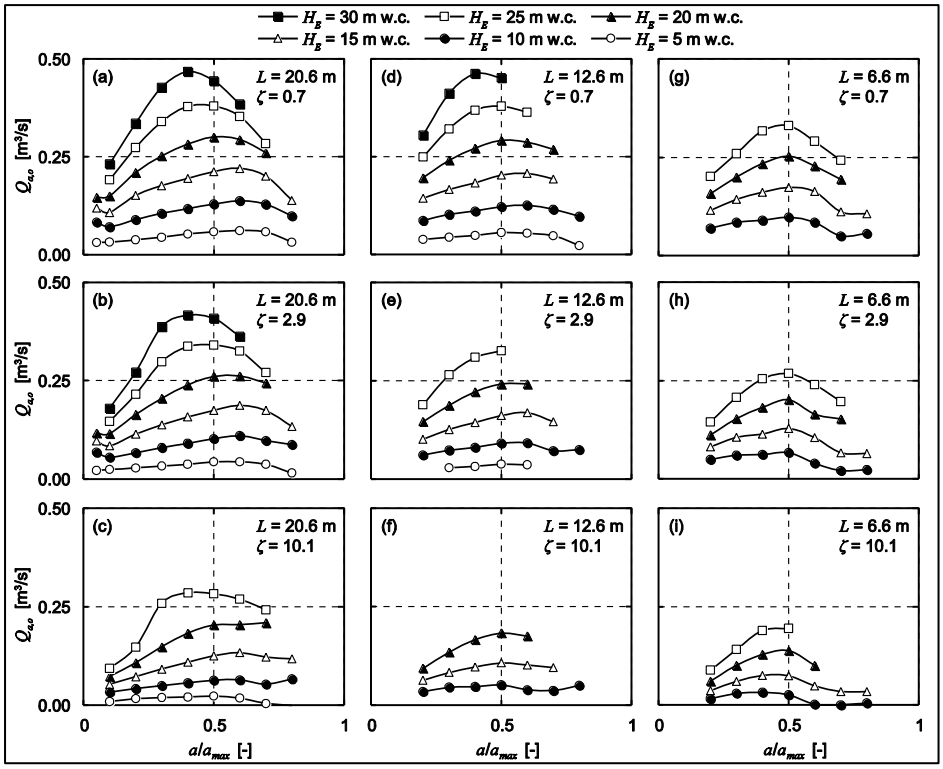

Figure 5. Air flow through aeration chamber $Q_{a,o}$ for different relative gate openings a/a_{max}, energy heads H_E, tunnel lengths L and air vent loss coefficients ζ. Missing measuring points are due to model limitations.

3.2.2 Air flow at the tunnel end

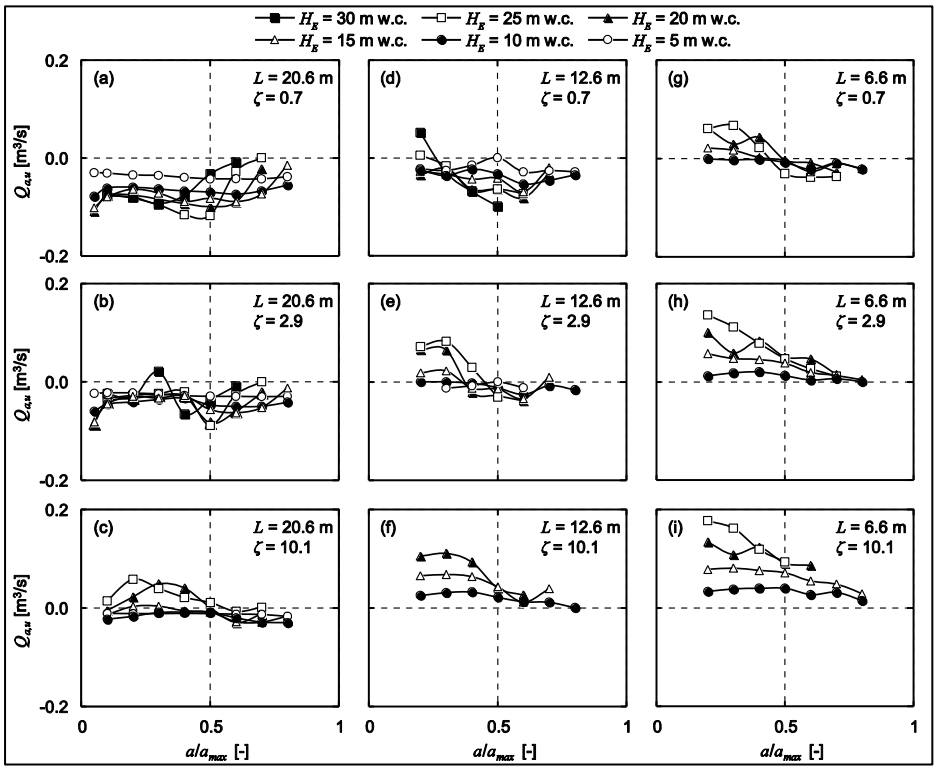

Figure 6. Air flow rate from/out of tunnel end, $Q_{a,u}$ for different relative gate openings, a/a_{max}, energy heads, H_E, tunnel lengths, L and air vent loss coefficients ζ, $Q_{a,u}$< 0 = air flow rate out of the tunnel, $Q_{a,u}$> 0 = air flow rate into the tunnel.

For long tunnels and small air vent loss coefficients, all air was supplied through the aeration chamber and air was flowing out of the tunnel end, i.e. $Q_{a,u}$< 0. (Fig. 6 a,b). At larger relative gate openings and large energy heads, $Q_{a,u}$ tended to zero as the tunnel was almost full at the downstream end. This coincides with

the decrease of $Q_{a,o}$ described in the previous section. When the loss coefficient of the aeration chamber was large enough, air was sucked into the tunnel at the tunnel end ($Q_{a,u}$> 0), especially for large H_E and small a/a_{max} (Fig. 6 c). This counter current air flow may trigger instabilities, which can lead to unsteady slug flow (section 3.1). With decreasing L and increasing ζ, more and more air was supplied from the downstream end until $Q_{a,u}$ was positive for all tested relative gate openings and energy heads (Fig. 6 f, h, i).

3.2.3 Air demand of bottom outlets

For the analysis of the air demand, only tests with free-surface flow were considered. Additionally, tests with Weber numbers W < 170 were excluded to avoid scale effects (Skripalle, 1994). The remaining parameter space covered 0.2 ≤a/a_{max}≤ 0.6, 0.7 ≤ζ≤ 60, 22 ≤L/h_t≤ 69 and 5 ≤ H_E ≤ 30, resulting in 8 ≤ F_c≤ 40.

The air demand is usually expressed as $\beta = Q_{a,o}/Q_w$, neglecting the air flow from the tunnel end. As shown in section 3.2.2, $Q_{a,o}$ depends on H_E, a/a_{max}, L and ζ. With these independent parameters, the following governing dimensionless parameters can be derived from a dimensional analysis: Relative tunnel filling a/h_t, relative tunnel length L/h_t, and $F_c = (2H_E/h_c)^{0.5}$. Using a non-linear least-square regression, the following best fit equation was found (Fig. 7):

$$\beta = 0.0076 F_c^{1.71} \zeta^{-0.22} \left(\frac{L}{h_t}\right)^{0.26} \left(\frac{a}{h_t} - 1.26\left(\frac{a}{h_t}\right)^2\right) \quad (1)$$

The comparison of calculated and measured β-values (Fig. 7) resulted in a coefficient of determination of R^2 = 0.96. With an exponent of 1.71, F_c has the largest effect on the air demand. The air vent loss coefficient and the relative tunnel length have an opposing effect of almost the same magnitude on β. Large ζ led to decreased β-values, while large L/h_t caused an increase in β. The relative tunnel filling was considered with a quadratic function as both small and large a/h_t led to small β-values. At small a/h_t (and thus a/a_{max} *for* h_t/a_{max} = *1.2 = const.*) values, $Q_{a,u}$ increased, thus leading to a decrease in $Q_{a,o}$ (Figs. 5, 6). For large a/h_t, the air flow rate through the aeration chamber was restricted by the small cross-sectional area above the mixture. The air demand was thus maximal for relative gate openings of 0.4 < a/a_{max} < 0.6 (Fig. 5), corresponding to relative tunnel fillings of 0.33 <a/h_t< 0.5. Figure 7 shows a good overall agreement with the measurement data. For air demand values β< 0.6, the scatter was comparably large. This can be partially attributed to viscosity effects for small $Q_{a,o}$-values, for which ζ depends on the Reynolds number and thus deviates from the constant ζ-values for fully turbulent-rough conditions. However, these small β-values are generally not relevant for design purposes. Eq. (1) can be considered as a first preliminary design equation, as the comparison with other model or prototype data has not been done yet.

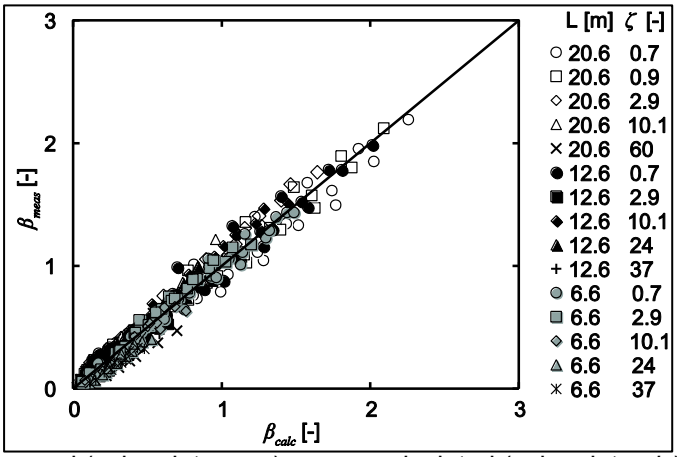

Figure 7. Comparison of measured (subscript *meas*) versus calculated (subscript *calc*) air demand from Eq. (1) for given L and ζ (symbols) for all tested H_E and a/a_{max} values.

3.3 Negative air pressures

3.3.1 Gate vibrations and incipient cavitation

Knowledge on the negative pressure development along the tunnel is of interest for problems regarding gate vibrations and incipient cavitation. The maximum negative values to avoid gate vibration in prototypes ranged from −0.3 to −1.5 m w.c. (Dettmers, 1953; Douma, 1955). The actual value depends on the given

outlet geometry and gate type. The ambient pressure in the tunnel was also used to calculate the cavitation index σ:

$$\sigma = \frac{h_p + h_{amb} - h_v}{U^2/2g} \tag{2}$$

where h_p= local water pressure [m w.c.], h_{amb}= ambient pressure [m w.c.], h_v= water vapor pressure [m w.c.] and U=mean water flow velocity [m/s]. For a computational example with prototype conditions, assuming h_p = 1 m w.c., h_v = 0.13 m w.c. (at 10° C) and U = 30 m/s, the cavitation index for h_{amb} = atmospheric pressure, P_{atm}(≈ 10 m w.c. at sea level) was σ = 0.237. A sub-atmospheric pressure of −2.0 m w.c. (h_{amb} = 8.0 m w.c.) resulted in σ = 0.193<σ_{crit} ≈ 0.20 = critical cavitation index for smooth inverts. Thus, severe cavitation damage was expected even for smooth inverts with minimum construction tolerances (Falvey, 1983).

3.3.2 Negative air pressure in the aeration chamber

As stated by Speerli (1999), the minimal negative relative air pressure in the aeration chamber $P_{a,min}$–P_{atm} just downstream of the gate (Fig. 3) can be calculated by applying the Bernoulli equation to the air vent:

$$\frac{P_{a,\min} - P_{atm}}{\rho_a g} = -(1+\zeta)\frac{\left(4Q_{a,o}/\left(d^2\pi\right)\right)^2}{2g} \tag{3}$$

Thus, P_a can be calculated from the properties of the aeration system (ζ, d) if $Q_{a,o}$ is known. The ζ-value can be calculated from the air vent geometry using e.g. Idel'cik (2005).

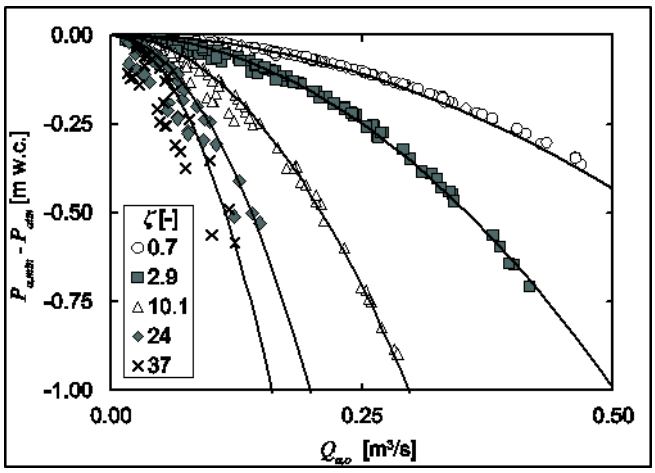

Figure 8. Negative relative air pressure in the aeration chamber $P_{a,min} - P_{atm}$ as a function of air flow rate $Q_{a,o}$ for different loss coefficients ζ. Solid lines represent Eq. (3) for the respective ζ.

The comparison of Eq. (3) with the physical model data of the present study shows a good agreement (Fig. 8). No additional effects of gate opening or tunnel length were observed, concluding that P_a seems to be independent of the air flow from the tunnel end. The deviation from Eq. (3) in Fig. 8 for small $Q_{a,o}$ and large ζ is caused by viscosity effects of the air vent loss coefficient (section 3.2.4).

3.3.3 Air pressure development along the tunnel

The air pressure P_a typically increased from its minimum in the aeration chamber to atmospheric pressure at the tunnel end (Fig. 9). For L = 20.6 m and ζ = 0.7, the relative pressure increased exponentially along the tunnel (Fig. 9a). At high energy heads, the relative pressure became positive at the tunnel end even though the mixture surface did not touch the tunnel soffit. The large amount of air dragged along with the two-phase flow was compressed in the downstream half of the tunnel, where the free cross-sectional area above the mixture decreased.

Higher ζ led to an almost linear increase of relative air pressure along the tunnel, especially for high energy heads (Fig. 9b). For H_E ≥ 20 m w.c. in Fig. 9b, a counter-current air flow was observed ($Q_{a,u}$>> 0) and for H_E< 20 m w.c. the air flow rate from the tunnel end was almost zero (see Fig. 6). A similar observation was made for L = 12.6 m and ζ = 2.9 (Fig. 9c), again $Q_{a,u}$ was almost zero for the shown configuration. In contrast to the configuration in Fig. 9a, there was a strong concurrent flow of air ($Q_{a,u}$<< 0). This demonstrates that the magnitude and direction of the air flow in the tunnel has a strong effect on the relative air pressure development along the tunnel.

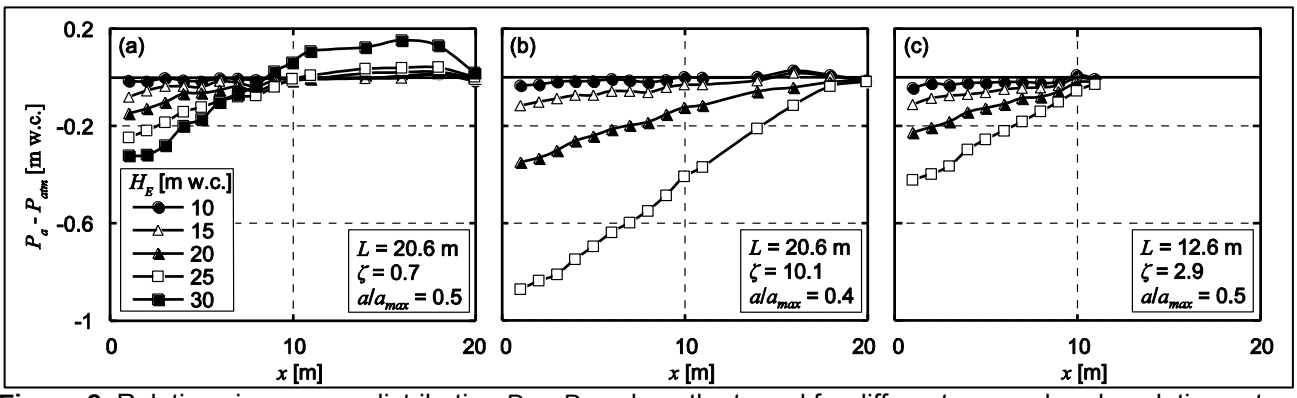

Figure 9. Relative air pressure distribution $P_a - P_{atm}$ along the tunnel for different energy heads, relative gate openings, air vent loss coefficients and tunnel lengths.

4 CONCLUSIONS AND OUTLOOK

Experiments on the air demand of bottom outlets were conducted using a new physical bottom outlet model with energy heads up to 30 m w.c. at full gate opening. The test range of the new physical model has exceeded previous studies and is relatively close to prototype conditions. All possible flow patterns in bottom outlets can thus be observed in the model. With increasing relative gate opening, the flow changed from spray to free-surface flow. For large relative gate openings, foamy flow and the transition to fully pressurized flow were observed. Unsteady flow transitions, so called slug flows, were observed for moderate relative gate openings, high energy heads and large air vent loss coefficients.

The air demand of a bottom outlet depended mainly on the Froude number at the vena contracta, where an increasing Froude number led to an increase in air demand. The relative tunnel length and the loss coefficient of the air vent affected the air demand to the same magnitude but opposing degree. Shorter tunnels led to a slight decrease in air demand, as more air was supplied from the tunnel end. Large air vent loss coefficients also reduced the air demand and consequently led to a lower pressure in the aeration chamber. The maximal air demand occurred for moderate relative tunnel fillings. Both small and large relative tunnel fillings led to a decrease in air demand. An empirical equation taking into account the above mentioned parameters is presented, thereby extending existing approaches which mostly considered only the Froude number as a relevant parameter.

The minimal negative pressure in the aeration chamber depended only on the air vent geometry and the air flow rate and can directly be calculated using the Bernoulli equation. Starting from the minimal value just downstream of the gate, the pressure increased to atmospheric pressure towards the tunnel end. The rate of pressure increase along the tunnel depended on the magnitude and direction of the air flow from the tunnel end. Further experiments are needed to describe the air pressure development along the tunnel in detail.

As a next step, the effect of the tunnel slope on flow pattern, air demand and air pressure will be investigated. Based on the new data to be collected, an updated empirical equation describing the air demand and a flow pattern map will be prepared. Additionally, the hydraulics of the two-phase air-water flow will be investigated with regards to flow velocity, mean and bottom air concentration.

ACKNOWLEDGEMENTS

This research project is funded by the Swiss National Science Foundation (SNF Grant No. 163415) and is part of the Swiss Competence Center for Energy Research (SCCER-SoE) framework. Prof. Dr. R. Boes and Dr. L. Schmocker are gratefully acknowledged for the project supervision and their invaluable contributions.

REFERENCES

Bollrich, G. (2007). *Technische Hydromechanik, Band 1*. sixth ed. Huss-Medien GmbH, Berlin (in German).

Campbell, F.B. & Guyton, B. (1953). Air demand in gated outlet works. *Proc. 5th IAHR Congress*, Minnesota, 529-533.

Dettmers, D. (1953). Beitrag zur Frage der Belüftung von Tiefschützen. *Mitteilungen der Hannoverschen Versuchsanstalt für Grundbau und Wasserbau*, Franzius-Institut der Technischen Hochschule Hannover. (in German)

Douma, H. (1955). Hydraulic Design Criteria for Reservoir Outlets. *Proc. 6th IAHR Congress*, The Hague, C 10, 1-20.

Falvey, H.T. (1983). *Prevention of Cavitation on Chutes and Spillways.* Frontiers in hydraulic engineering, 432-437, Massachusetts Institute of Technology, Cambridge.

Guyton, B. (1958). Field Investigation of Spillways and Outlet Works. *Journal of the Hydraulics Division* ASCE, 84(1), 1-21.

Idel'cik, I. E. (2005). *Handbook of Hydraulic Resistance*, 3rd edition, Jaico Publishing House Inc., India.
Kalinske, A.A. & Robertson, J.W. (1943). Closed Conduit Flow. *ASCE Transactions*, 108(2), 1435–1447.
Levin, L. (1965). Calcul hydraulique des conduits d'aération des vidanges de fond et dispositifs déversants (Hydraulic Calculation of Air Vents for Bottom Outlets and Diversion Tunnels). *La houille blanche*, No. 2, 121-127. (in French)
Lynse, D.K. & Guttormsen, 0. (1971). Air Demand in High Regulated Outlet Works. *Proc. 14th IAHR Congress*, Paris, 5, 77-80.
Mura, Y., Ijuin, S. & Nakagawa, H. (1959). Air Demand in Conduits Partly Filled with Flowing Water. *Proc. 8th IAHR Congress*, Montreal, 2(12), 1-14.
Ouazar, D. (1983). Prévention de l'érosion de cavitation par l'aération (Prevention of Caviation Erosion with Flow-Aeration). *Thèse de doctorat*, Collection des publications No. 91, Faculté des sciences appliquées, Université de Liège (in French).
Rabben, S.L. (1984). Untersuchung der Belüftung an Tiefschützen unter besonderer Berücksichtigung von Massstabseffekten (Investigation of Aeration of High-Head Gates under Special Consideration of Scale Effects). *Mitteilung Nr.* 53, Institut für Wasserbau und Wasserwirtschaft, RWTH Aachen (in German).
Roth, A. & Hager, W.H. (1999). Underflow of Standard Sluice Gate. *Experiments in Fluids*, 27(4), 339-350.
Schilling, H. (1963). Luftmengenmessungen in Grundablässen von Stauanlagen (Air-Flow Measurements in Bottom Outlets of Dams). *Escher Wyss Mitteilungen*, 36(2/3), 41-47. (in German)
Skripalle, J. (1994). Zwangsbelüftung von Hochgeschwindigkeitsströmungen an zurückspringenden Stufen im Wasserbau (Forced Aeration of High-Velocity Jets at Backward Facing Steps in Hydaulic Constructions). *Report Nr.* 124. Institute for Hydraulic Engineering and Water Management, Technical University Berlin. (in German)
Sharma, H.R. (1973). Air Demand for High Head Gated Conduits. *PhD thesis*. University of Trondheim, the Norwegian Institute of Technology, Trondheim.
Speerli, J. (1999). Strömungsprozesse in Grundablassstollen (Hydraulics of Bottom Outlets). *Mitteilung 163 (H.-E. Minor, ed.)*, Versuchsanstalt für Wasserbau, Hydrologie und Glaziologie VAW, ETH Zürich, Zurich. (in German)
US Corps of Engineers (USCE). (1954). *Slide Gate Tests, Norfork Dam North Fork River, Arkansas*, Technical Memorandum No. 2-389, Waterways Experiment Station, Vicksburg, Mississippi, USA.
US Corps of Engineers (USCE). (1964). *Air Demand – Regulated Outlet Works*, *Hydraulic Design Criteria*, sheet 050-1/2/3, 211-1/2, 212-1/2, 225-1. US Corps of Engineers. USA.
Vischer, D. & Hager W.H. (1998). *Dam Hydraulics*. Wiley: Chichester, New York, USA.
Wisner, P. (1967). Air Entrainment in High Speed Flows. *Proc. 9th ICOLD Congress*, Istanbul, 495-507.
Wunderlich, W. (1963). Die Grundablässe an Talsperren, Teil 2 (Bottom Outlets of Dams, Part 2). *Wasserwirtschaft*, 53(4), 106-114. (in German)

Proceedings of the 37th IAHR World Congress
August 13 – 18, 2017, Kuala Lumpur, Malaysia

RESONANCE WAVE PUMPING: MEAN WAVE MASS FLUX

REMI CARMIGNIANI[(1)], DAMIEN VIOLEAU[(2)] & MORTEZA GHARIB[(3)]

[(1)] Saint-Venant Laboratory for hydraulics, University Paris-Est Cretail, Chatou, France, rcarmi@me.com
[(2)] EDF & Saint-Venant Laboratory for hydraulics, University Paris-Est Cretail, Chatou, France
[(3)] Aeronautics and Bioengineering, California Institute of Technology, Pasadena, CA, USA.

ABSTRACT

Inspired by the valveless impedance pump of Liebau, a free-surface wave pump was designed and investigated experimentally: resonance wave pump. It consists of a rectangular tank with a centered submerged plate. It separates the tank into a free-surface section above the submerged plate and a rigid recirculation section under it. A paddle generates wave above the submerged plate at an off-centered position. It was reported by the authors (Carmigniani et al., 2017) that near certain frequencies (natural or resonance frequencies), a unidirectional pulsating flow was generated under the submerged plate. The pumping mechanism can be explained by the Stokes wave mass transport. To further understand the pumping dynamic, experiments with Particle Image Velocimetry (PIV) and Volume of Fluid (VOF) simulations were conducted to investigate the flow above the submerged plate. Good agreement was found between the experiments and the simulations mean mass flux field. The simulations were further used to evaluate the Stokes wave mass transport, which was compared to the second order wave mass transport model proposed in Carmigniani et al. (2017). This study confirms the importance of the wave mass transport in the pumping mechanism of the resonance wave tank.

Keywords: Wave-mean flow; PIV; waves/free-surface flows.

1 INTRODUCTION: RESONANCE WAVE TANK AND WAVE MASS TRANSPORT

Liebau (1954; 1955) showed the principle of valveless pumping produced by an oscillatory excitation (pinching) of a flexible tube at an off-centered position (Avrahami and Gharib, 2008; Hickerson and Gharib, 2006). It was observed that a unidirectional flow can arise from this alternative motion near certain frequencies: resonance frequencies. The authors showed that it was possible to design a similar kind of pump without the flexible tubes: a resonance wave pump (Carmigniani et al., 2017).

This system seems similar to the wave above a submerged plate case (Dick, 1968; Patarapanich, 1984; Carter et al., 2006; Poupardin et al., 2012; Murakami et al., 1992). This is the limit case of infinite openings and the paddle near one wall. It has been observed in numerous studies that a pulsating flow rose under the submerged plate due to wave action. The direction of the mean flow under the submerged plate was in the opposite direction to the incident wave. Similar behavior can be observed in the case of the close resonance wave tank.

The study of the resonance wave tank can give insight into the pumping mechanism of waves and enable optimization of such wave energy conversion devices from potential and kinetic energy near the free surface into under-water current. The goal of this study is to extract the mean flow dynamics above the submerged plate to understand its origin in the case of the resonance wave tank.

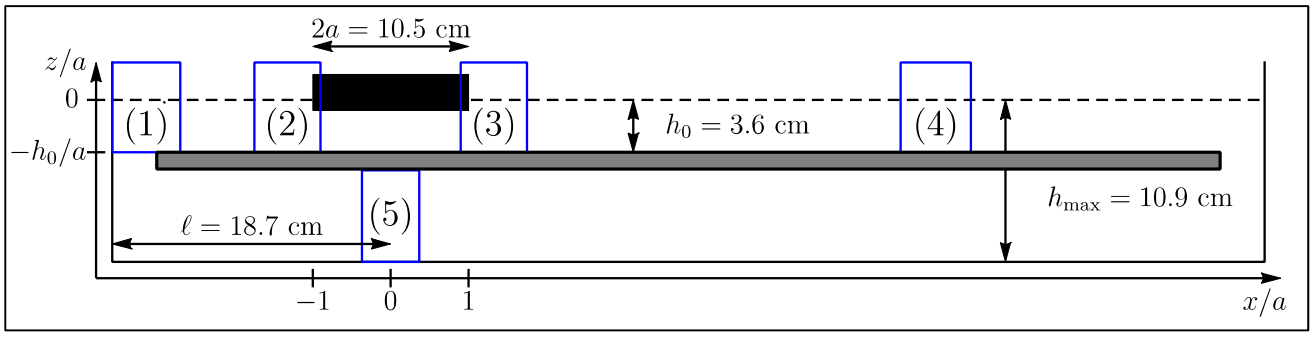

Figure 1. A sketch of the resonance wave tank and the outline of the different visualizations zones used in the PIV.

The resonance wave tank consisted of a 77.4x25x25 cm^3 rectangular tank filled with $h_{max} = 10.9$ cm of water. A rectangular plate spanning the entire tank width and almost all its length was placed at $h_0 = 3.6$ cm under the undisturbed water surface (defined here with the paddle at its mean draft position). The openings at the two extremities ($\Delta x = 3$ cm long) allowed recirculation under the submerged plate. A paddle of length $2a = 10.5$ cm oscillated vertically in a heaving motion with a forced frequency f_0 and amplitude S_0. Its mean horizontal position was such that the center of the paddle was located at $\ell = 18.7$ cm away from the left wall and its mean draft is $d = 0.7$ cm. Figure 1 shows a sketched representation of a cross section of the pump. As for the rest, it was assumed that the problem was 2 dimensional.

The authors measured the flow rate under the submerged plate ϕ using Particle Image Velocimetry (PIV). The main results are available in the reference study of Carmigniani et al. (2017). Starting from a quasi at rest tank, the flow rate under the submerged plate has a transitional stage before reaching an asymptotic regime. The flow rate under the submerged plate is plotted as a function of time in figure 2 for the case $S_0/h_0 = 19\%$ and $f_0 = 1.2$ Hz. The system reached an asymptotic pulse flow regime after 20 s. In this regime, the flow rate oscillated between zero and a negative value with a significant bulk component of about -10 cm^2.s^{-1}. There was a clockwise circulation around the submerged plate. Such behaviors are particularly interesting for future applications since the oscillatory motion of the paddle was converted into a quasi-continuous flow in time. The authors showed that this behavior occurs at resonance frequencies using a linear potential theory and eigenfunction expansions (Carmigniani et al., 2017).

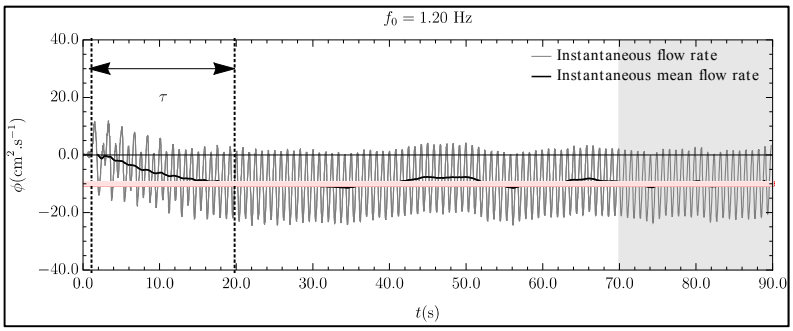

Figure 2. Instantaneous flow rate for $f_0 = 1.2$ Hz and $S_0 = 0.69$ cm.

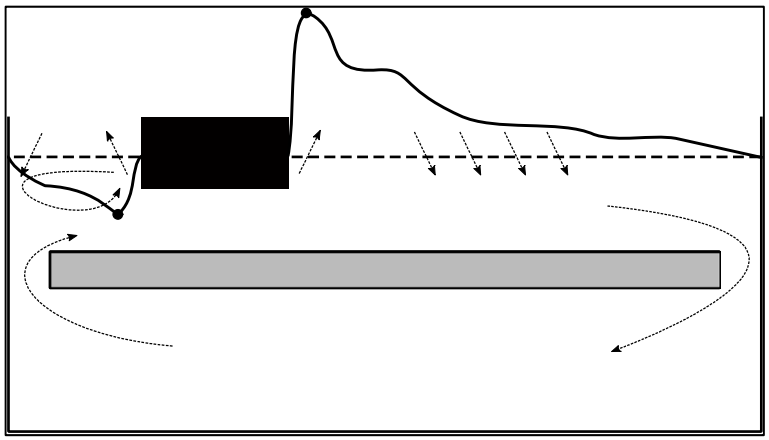

Figure 3. A sketch of the wave mass transport and mean flow generation.

At these frequencies, the waves were amplified and eventually break. To take into account this phenomenon, the authors proposed to add dissipation to the propagative terms of the eigenfunction expansion. To scale the dissipation, they used a wave-breaking criterion. The main result of the model was that the wave mass transport was not identically zero in the tank and led to circulation (see figure 3). In the non-dissipative linear theory, the solution was a standing wave. This implies that there is no wave mass transport.The wave mass transport appears in the mean flow second order kinematic free surface condition. Consider the kinematic free surface condition in the general potential theory:

$$\frac{\partial \eta}{\partial t} + \frac{\partial \varphi}{\partial x}\frac{\partial \eta}{\partial x} = \frac{\partial \varphi}{\partial z} \quad \text{at } z=\eta(x,t), \qquad [1]$$

where η is the free surface position and φ is the scalar velocity potential. The different functions are decomposed into:

$$a(t)= \bar{a}+a', \quad [2]$$

where $\bar{a}$ is the mean part (assumed steady) and a' is a rapidly varying part of typical time of a wave period. Assuming that $\|\bar{a}\| \ll \|a'\|$, and that $\overline{a'} = 0$, averaging over time (on a typical time scale of a wave period) leads to the mean free surface condition:

$$\frac{\partial \bar{\varphi}}{\partial z} = \frac{\partial M^w}{\partial x} \quad \text{at } z=\bar{\eta}(x), \quad [3]$$

where:

$$M^w = \overline{\eta' \frac{\partial \varphi'}{\partial x}\Big|_{z=0}}, \quad [4]$$

is the Stokes wave mass transport. This term can be derived from the averaged Navier-Stokes equations (Hasselmann, 1971). It corresponds to a surface current in the linear theory. In eq.3, a variation of the wave mass transport leads to a transfer of mass between the surface layer and the bulk part of the flow (or interior). This is sketched in figure 3 where the authors show the interaction between the wave mass transport and the bulk part of the flow. The solid black line represents the wave mass transport value: positive (to the right) above the undisturbed surface (dashed line) and negative otherwise. The arrows near the surface represent the exchange of mass between the surface layer and the bulk part of the flow. The goal of this study is to observe the predicted dynamics in the resonance wave tank.

2 MASS FLUX ABOVE THE SUBMERGED PLATE

In order to investigate the importance of the Stokes wave mass transport, we performed PIV measurements of the flow above the submerged plate and Volume of Fluid (VOF) simulations. In the first part, the experimental procedures are first described and the results are shown. The experiments were limited to small section of the tank and small amplitude to avoid wave breaking. To have a global view of the tank in the case of wave breaking, we ran numerical simulations of the entire experimental tank using OpenFOAM "interDyMFOAM" solver method in the second part. The numerical method was validated by comparing the frequency response to the experimental results and the mean mass flux was extracted. From the simulations, the wave mass transport was calculated and compared to the model proposed in Carmigniani et al. (2017).

2.1 PIV near the free surface

2.1.1 Experimental setup and data acquisition

The experiments were performed in the same resonance wave tank as described previously. In all these sections, the amplitude was fixed to $S_0 = 0.34 \pm 0.01$ cm and $f_0 = 1.2125$ Hz. At this frequency, the resonance wave tank was near a resonance but there was no wave breaking. The surface is not too highly deformed. Thus, measurement can be taken in the vicinity of the free surface. The Particle Image Velocimetry (PIV) was used for the visualization purpose of the present study. A 1W 532 nm green continuous laser (Wicked Laser) and cylindrical lens were used to create a laser sheet from under the tank. The fluid was seeded with fused borosilicate glass spherical particles of typical size $25\ \mu m$ and density 1.10 g/cc (Potters 110P8). A camera (NanoSense MkIII) was mounted with a Tamron 90mm lens and records videos at 400 frames per seconds (fps) for 10.8 seconds for the flow measurement above the submerged plate. The camera was moved to four different positions above the submerged plate (see figure 4 and zones (1) to (4)). The visualization zones are 4.5x 6.0 cm and have a resolution of 164 pixel/cm. The MATLAB PIVlab (Thielicke and Stamhuis, 2014a; 2014b) package was used to analyze the PIV data. The experiment was run twice per visualization zone. Prior to recording the data, we waited for at least 1 minute and 30 seconds where the system reaches an asymptotic regime. The sample was then cut into 30 phases evenly distributed over one period. For each phase, we have 13 sets of two images spaced by 1/400 s for each experiment. The results of each phase were thus averaged on 13 periods ($T = 1/f_0$) and the mean mass flux fields were obtained by averaging the 30 phases on the two experimental sets. The obtained velocity field resolution was 10 vectors/cm. The standard deviation was also obtained using this way. The camera was not synchronized with the paddle. The origin of time was thus chosen arbitrarily in the next section. The PIV was performed near the free surface. All the pixels above the surface were masked out to run the PIV. The surface might be difficult to detect automatically in all cases. The detection was performed manually and this justifies the limitation to 30 phases in the data while we recorded at 400 fps with a continuous laser. The camera also records the flow under the submerged plate in a similar manner at 100 frames per seconds for 16 seconds on two different experiments. Figure 1 shows the different visualization zones considered in the tank.

2.1.2 Experimental results and discussion

The flow rate under the submerged plate for this case had a mean value of -3.1 ± 0.05 cm^2.s^{-1} where the fluctuation represents the difference between the two experiments. Figure 4 shows the mean velocity profile averaged between the two experiments and the flow rate over a period for the two experiments separately. The configuration was close to a resonance and a clockwise circulation occurs. The origin of time $t/T = 0$ was defined here as the moment when the flow rate starts to be larger than the mean value. The flow rate was above the mean value for $t/T \approx 0.48$. This means that the solution was close to a sine function of time under the submerged plate with a small second order contribution.

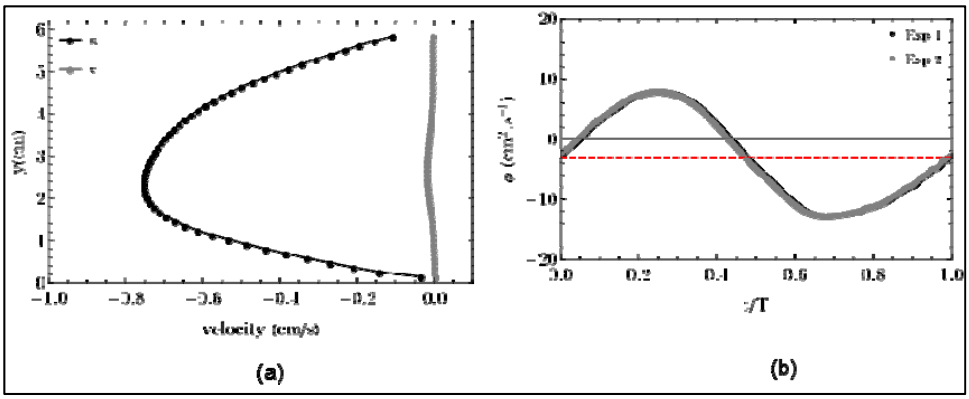

Figure 4. Velocity (horizontal u, and vertical v) profiles under the submerged plate (a) and flow rate in visualization zone (5) (see figure 1).

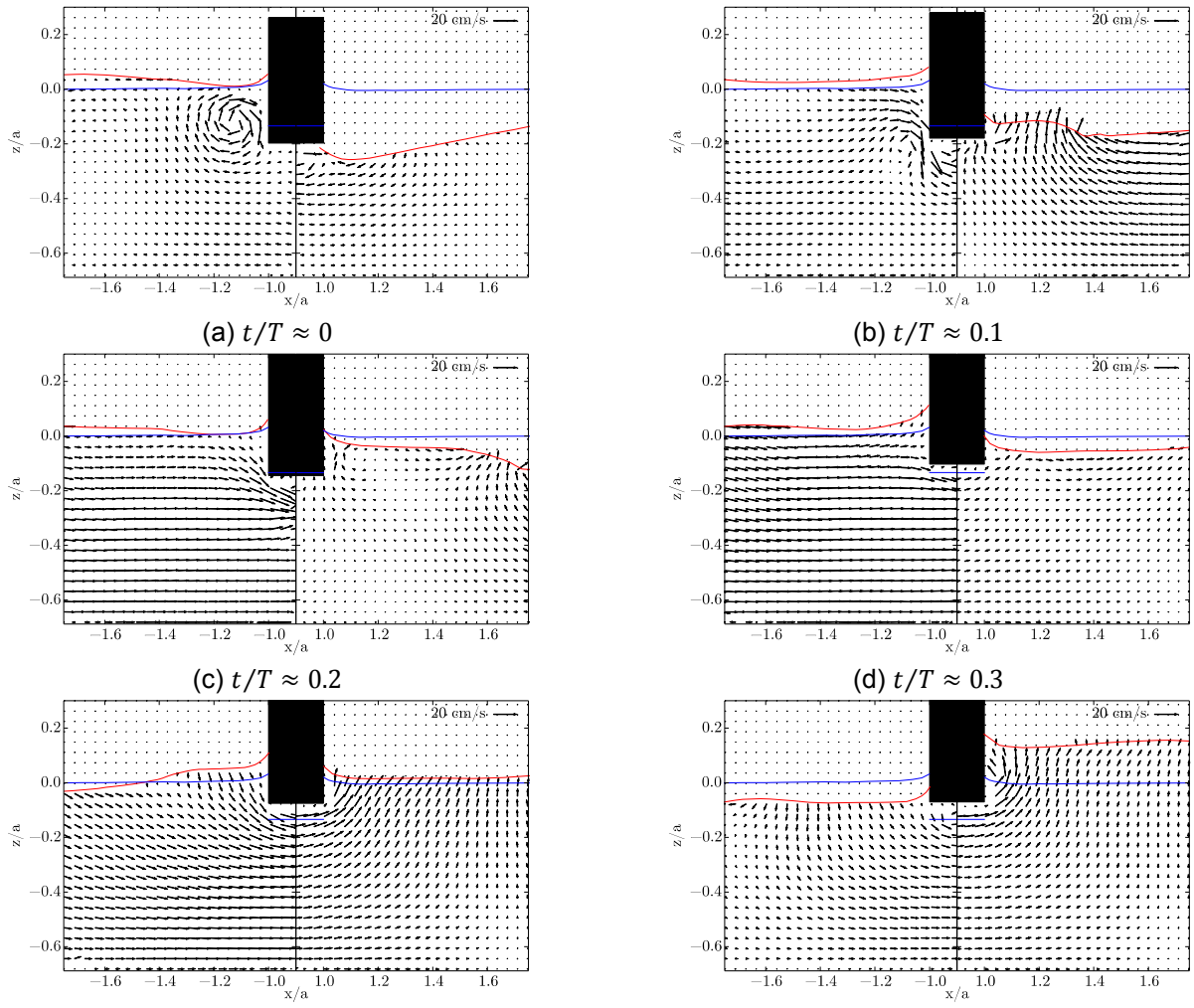

(a) $t/T \approx 0$ (b) $t/T \approx 0.1$

(c) $t/T \approx 0.2$ (d) $t/T \approx 0.3$

(e) $t/T \approx 0.4$ (f) $t/T \approx 0.5$

Figure 5. Instantaneous velocity field in zones (2) and (3) (see figure 1) at six instances in the upward paddle stroke.

Consider for now the instantaneous velocity near the paddle in visualization zones (2) and (3) of figure 1. We define the phase origin as the moment when the paddle is at its lowermost position. Figure 5 (figure 6) shows the velocity at six instances in an upward (downward) paddle stroke (respectively). The red solid line represents the instantaneous free-surface position. The paddle is represented by the black rectangles. The paddle is non-dimensionally located between -1 and 1. The quiver plots show only a quarter of the vectors for the sake of clarity. The data shows a single experimental set averaged on the 13 wave periods at 10 different paddle stroke instances.

During the upward part of the stroke (figure 5), the excess of water on the left side was discharged to the right. Note that if the tank were at rest and the paddle were moving up, one should expect the flow to be towards the paddle (suction). In here, the flow is from left to right. A strong traveling wave was generated on the right side of the paddle and the water level continued to rise. The wave is clearly visible in the instance $t/T \approx 0.1$ and $t/T \approx 0.2$, where it can be seen travelling to the right (away from the paddle). This would generate a forward mass transport in the surface layer, as we will see later.

During the downward motion (figure 6), the motion was reversed. The excess of water on the right was going to the left but the motion of the paddle limits this transfer. In the case of a tank starting at rest with a paddle moving down, one should expect the flow to travel away from the paddle. During an entire stroke (figure 5 and Figure 6), the surfaces on each side of the paddle are out-of-phase. This led to an optimal transfer of mass and an amplified wave on the right side.

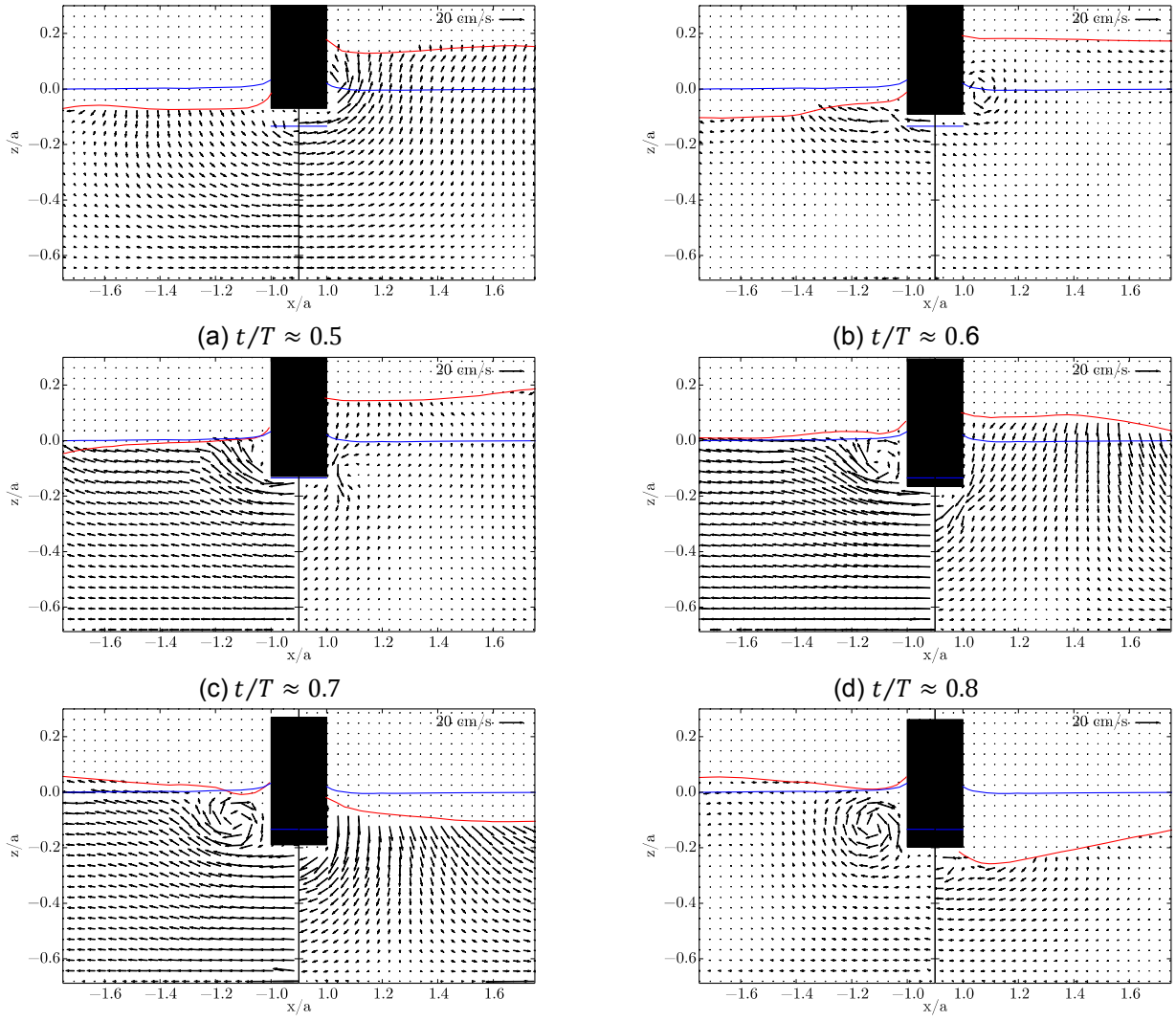

(a) $t/T \approx 0.5$ (b) $t/T \approx 0.6$

(c) $t/T \approx 0.7$ (d) $t/T \approx 0.8$

(e) $t/T \approx 0.9$ (f) $t/T \approx 1.0$

Figure 6. Instantaneous velocity field near the paddle in zones (2) and (3) (see figure 1) at six instances in the downward paddle stroke.

Averaging the flow on the 30 phases for the two sets of experiments gave the mean mass Eulerian flux field (figure 7 (a-d)). An instantaneous position in time in air has an attributed zero velocity. This is incorrect in the sense that the velocity of air is not zero. Thus, we consider the instantaneous mass flux $\rho \boldsymbol{u}$ and use the

assumption that $\rho_{air} \ll \rho_{water}$. In the part where the flow are always in the water, there is no difference between the mean mass flux and the mean velocity. For the surface layer, the Eulerian position will either be in the air (zero mass flux) or in the water at different times. In figures 7 (a-c) the momentum of air is neglected. The blue solid line represents the undisturbed free surface with the paddle at its mean draft position. The red solid line depicts the surface layer defined as the domain between the maximum and minimum surface elevation at a given horizontal position. The fluid domain spanned by the paddle is represented by the shaded gray rectangle. It is striking to see that the mean mass flux is not zero. Figure 7 (a,b) shows the mean mass flux near the paddle. On the left side, we see a forward mass flux underwater, a backward mass flux in the surface layer and a forward one near the paddle. There are two recirculation cells: one near the paddle and a second one in the opposite direction near position (-1.5,-0.15). On the right side, there is a strong mass flux in the surface layer and almost no flux below it. We can see two recirculation cells near the paddle. In the visualization zone (1), near the left edge of the submerged plate outlined by the dashed vertical line, we see a flux of mass travelling from under the submerged plate all the way up to the surface layer. The wave mass transport is thus toward the paddle. In the visualization zone (4), the flow was spread between the surface layer and the interior of the flow. The mass flux originally in the surface layer (zone 1) dived inside the interior of the fluid. In these experimental results, we observed the mean mass flux and could assess the fact that the dominant part of the flow came from the surface dynamic. The wave mass transport is an important part of the pumping mechanism.

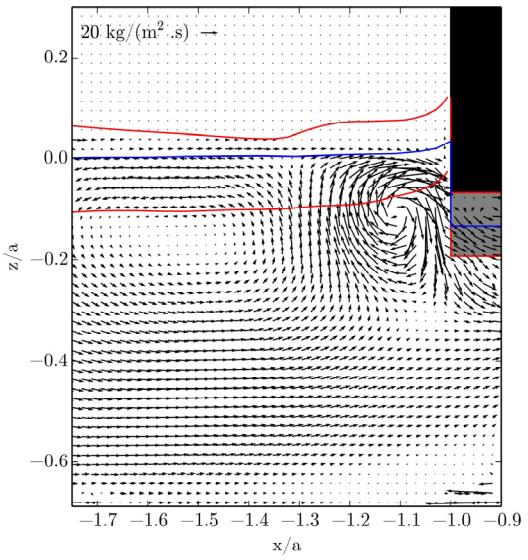

(a) visualization zone (2)

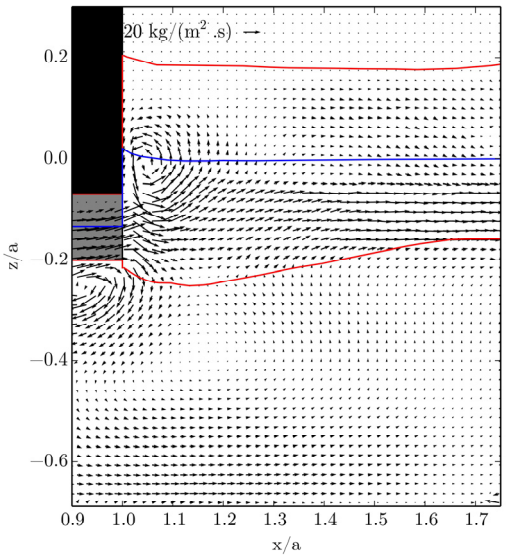

(b) visualization zone (3)

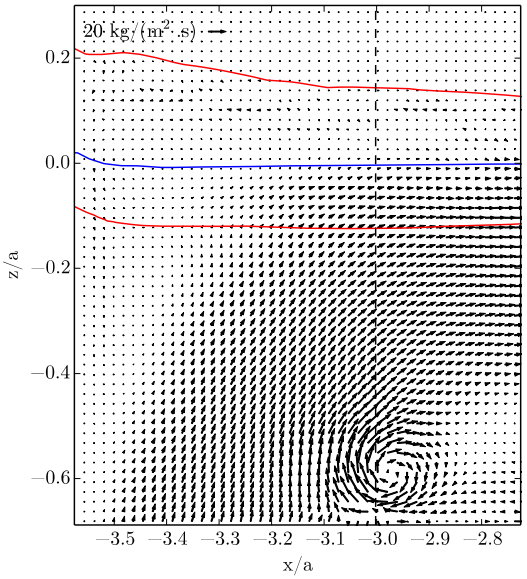

(c) visualization zone (1)

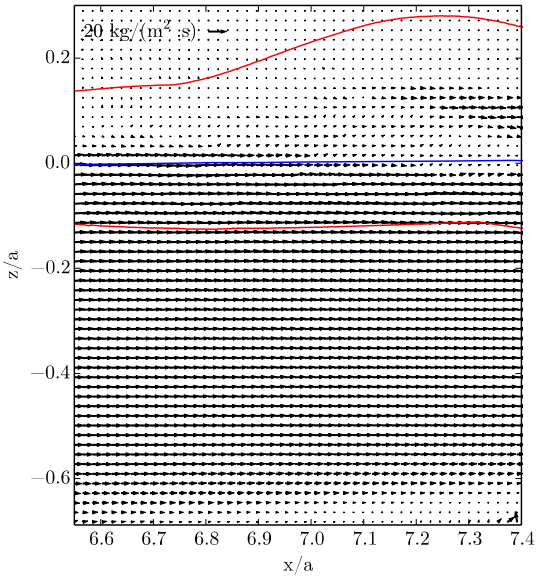

(d) visualizarion zone (4)

Figure 7. Mean mass flux in the different visualization windows.

2.2 Numerical simulations

2.2.1 Description and validation

To simulate the tank in 2D, we used the open source finite element code OpenFOAM and the built-in 'interDyMFOAM' solver. It allows mesh deformation and is used to control the paddle motion. The method used was a Volume of Fluid (VoF) method and both the air and water phases were simulated. A scalar function α represents the mixture. It is equal to 1 in the water and 0 in the air. A 77.4x25 cm^2 tank was simulated with a resolution of $\delta x = 0.1$ cm. The simulation was run for 120 seconds to reach the asymptotic regime. Then, 7 wave periods are sampled above the submerged plate and stored at a frequency of 200 Hz. The data was used to verify the flow rate and calculate the mean mass flux. We ran simulations for 14 frequencies (0.3 to 1.6 by 0.1 Hz) and stroke amplitude of $S_0 = 0.69$ cm. The wave-breaking threshold does not limit the simulation paddle stroke range, as it is the case for the PIV.

Figure 8 shows the mean flow rate measured in the simulation (solid red circles) and obtained by Carmigniani et al. (2017) (black, gray and light gray points). A good trend was obtained on the entire range of the simulation. The resonance near 1.2 Hz and 1.6 Hz were correctly captured. Note that the negative peak near 1.7 Hz was not visible here but this might be due to a small shift of the paddle position and the coarseness of the frequency steps used.

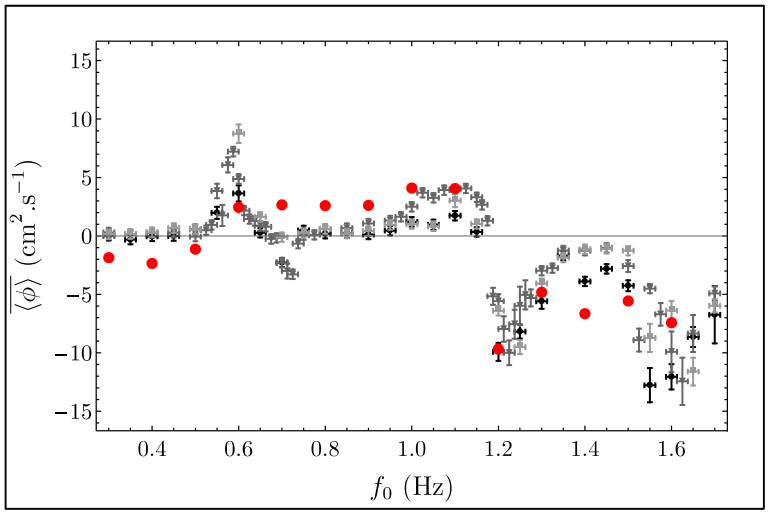

Figure 8. Comparison of the frequency response between the experiment (black, gray, light gray) and the simulations (solid red circles).

2.2.2 Mean flow above the submerged plate and wave mass transport

From the simulation, we evaluated the mean mass flux (defined here by $\overline{\alpha \boldsymbol{u}}$) above the submerged plate. The results are shown in figure 9 for the two resonance frequencies 1.2 Hz and 1.6Hz. The color map shows the magnitude of the velocity. The dashed white line shows the undisturbed water level and the solid white line shows the limits of the surface layer. The surface layer was obtained by looking at the mean transport scalar function. In the surface layer, the data varied between 1 and 0 strictly. The surface layer is defined here by:

$$0.02 < \bar{\alpha} < 0.98. \qquad [5]$$

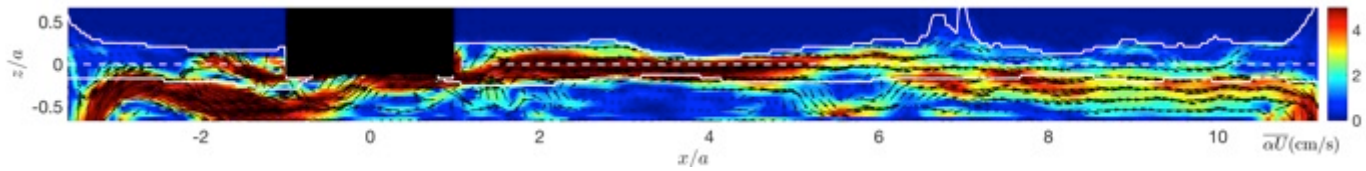

(a) $f_0 = 1.2$Hz

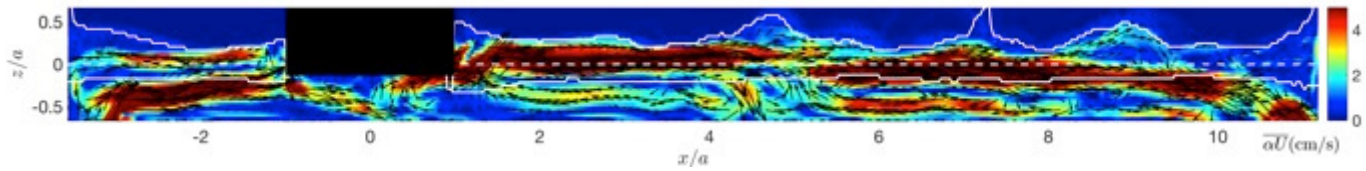

(b) $f_0 = 1.6$ Hz

Figure 9. Simulation of the mean mass flux ($\boldsymbol{\alpha u}$).

Figure 9 (a) is close to the frequency presented in the experiment and similar mean mass flux can be seen in the visualization zones (see figure 10 (a) where we emphasize zone 1 for $f_0 = 1.2$ Hz). Near the left submerged plate edge (see zoom figure 10 (a) too), there was a mass flux coming from under the submerged plate all the way up to the surface layer. It was then diving back into the interior of the flow before the paddle (below the surface layer level) near position -2. On the other side of the paddle, the mass flux was located almost completely in the surface layer between positions 1 and 5. It then started diving to circulate under the submerged plate.

In figure 9 (b) the dynamic is similar on the right side of the paddle but is different on the left. Indeed for this case, the mass flux is always negative in the surface layer (see also zoom figure 10 (b)). There is a large recirculation on the left side of the paddle. The mass flux coming from under the submerged plate did not reach the surface layer. This is close to the sketch proposed by Carmigniani et al. (2017) for this frequency (see figure 3). The pumping is less efficient for $f_0 = 1.6$ Hz as mass was pushed away from the paddle on both sides in average.

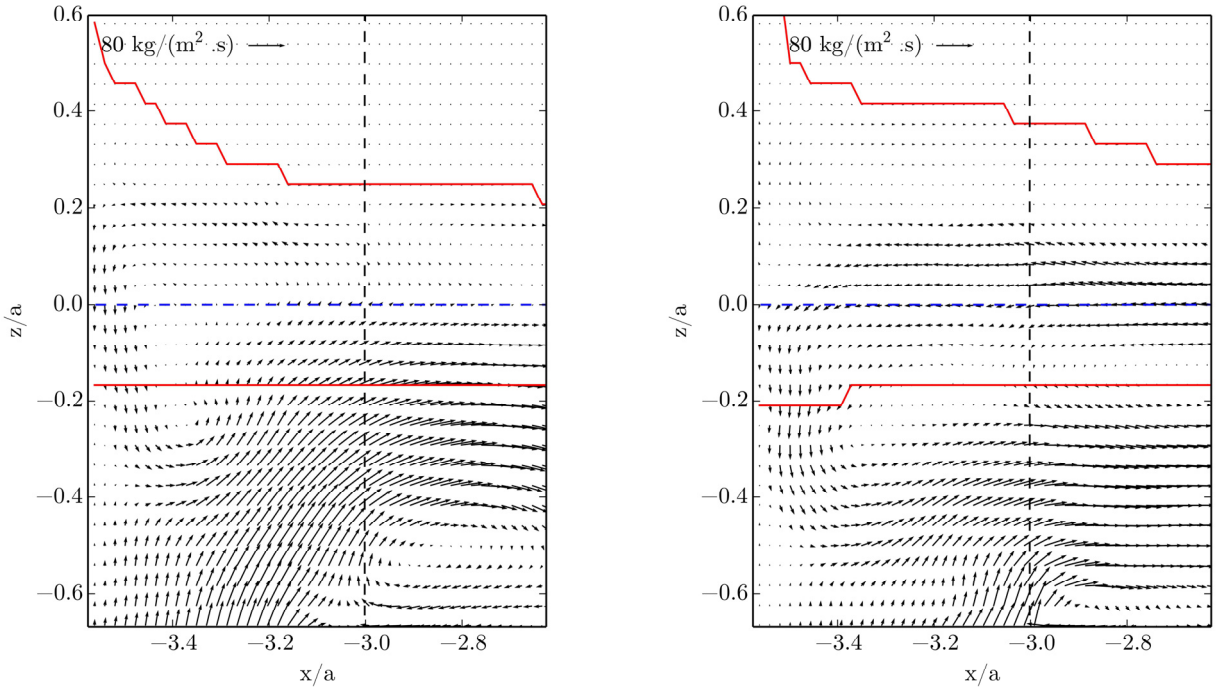

(a) $f_0 = 1.2$ Hz (b) $f_0 = 1.6$ Hz

Figure 10. Simulation zoomed on visualization zone 1 of the mean mass flux ($\overline{\rho \boldsymbol{u}}$).

In the simulations, we can further measure the wave mass transport and compare it to the model proposed in Carmigniani et al. (2017). This is done in figure 11 where we plotted the wave mass transport as a function of position. There is a good qualitative agreement with the model (red solid line). This confirms the importance of the wave mass transport in the pumping mechanism and validates the simple model proposed in Carmigniani et al. (2017).

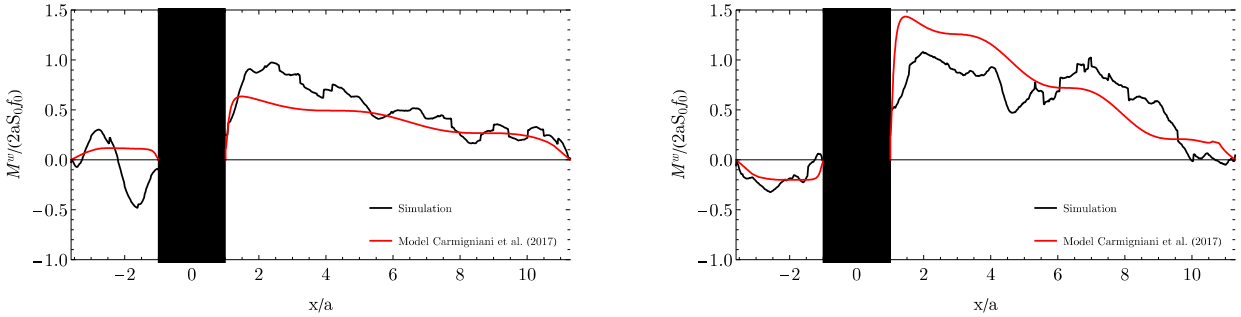

(a) $f_0 = 1.2$ Hz (b) $f_0 = 1.6$ Hz

Figure 11. Simulation measurement of the wave mass transport compared to the model of Carmigniani et al. (2017).

4 CONCLUSIONS

In this study, we looked at a free surface version of the Liebau pump. This was recently studied and proved to have similar behavior to the original Liebau beside the fact that there is no flexible tubing. The previous study (Carmigniani et al., 2017) focused on the frequency response of such pump and proposed a linear potential model with dissipation to explain the pumping. It was suggested that the Stokes wave mass transport is at the origin of the pumping.

This study provides PIV measurements of the flow near the surface layer for a case near a resonance frequency and small amplitude to be under the wave-breaking threshold. Instantaneous velocity field are shown and the dynamic between the left and right side of the paddle was described. It is particularly outlined that the two sides are out-of-phase. Next to the paddle on the left side, the water elevation is maximum while the paddle is near its lowest position. This led to a large transfer of mass under the paddle during its upward stroke and a strong travelling wave generated on the right side and away from the paddle. It is shown that the mean mass flux is strong in the surface layer on the right side of the paddle. This generated a clockwise circulation in the tank. The mass flux coming from under the paddle on the left side travels all the way up to the surface layer for this case.

Simulations are conducted using the open source code openFOAM 'interDyMFOAM' solver for larger paddle stroke amplitude. The simulations are validated. The mean mass flux was extracted from the simulations. Similar dynamic was found near the frequency that was studied experimentally. A different behavior was found for the next resonance frequency ($f_0 = 1.6$ Hz): the mass flux is away from the paddle on both sides as suggested by the Carmigniani *et al.* (2017) analytical model. There is a large circulation cells on the left (short) side of the paddle. The Stokes mass transport was measured in the simulations and compared to the model of Carmigniani et al. (2017) with good agreement.

This confirms the importance of the Stokes mass transport in the observed pumping mechanism.

ACKNOWLEDGEMENTS

The authors would like to acknowledge the Gordon and Betty Moore Foundation for their generous support. The authors would also like to thank Chris Roh his help in setting up the experiment at Caltech.

REFERENCES

Avrahami, I. & Gharib, M. (2008). Computational Studies of Resonance Wave Pumping in Compliant Tubes. *Journal of Fluid Mechanics,* 608, 139–160.

Carmigniani, R., Benoit, M., Violeau, D. & Gharib, M. (2017). Resonance Wave Pumping with Surface Wave *Journal of Fluid Mechanics*, 811, 1-36.

Carter, R.W., Ertekin, R.C. & Lin, P. (2006). On The Reverse Flow Beneath a Submerged Plate Due to Wave Action. *Proc. 25th International Conference on Offshore Mechanics and Arctic Engineering, Hamburg.*

OMAE Dick, T.M. (1968). On Solid and Permeable Submerged Breakwaters, *Kingston PhD Dissertation.* At Queens University.

Hasselmann, K. (1971). On the Mass and Momentum Transfer between Short Gravity Waves and Larger-Scale Motions. *Journal of Fluid Mechanics,* 50, 189–205.

Hickerson, A.I. & Gharib, M. (2006). On the Resonance of a Pliant Tube as a Mechanism for Valveless Pumping. *Journal of Fluid Mechanics,* 555, 141–148.

Liebau, G. (1954). Über ein ventilloses pumpprinzip. *Naturwissenschaften* 41, 327–327.

Liebau, G. (1955). Prinzipien kombinierter ventilloser Pumpen, abgeleitet vom menschlichen Blutkreislauf. *Naturwissenschaften* 42, 339–339.

Patarapanich, M. (1984). Maximum and Zero Reflection from Submerged Plate. *Journal of Waterway Port, Coastal, and Ocean Engineering.* 110(2) 71–181.

Poupardin, A., Perret, G., Pinon, G., Bourneton, N., Rivoalean, E. & Brossard, J. (2012). Vortex Kinematic Around a Submerged Plate under Water Waves. Part I: Experimental Analysis. *European Journal of Fluid Mechanics,* 34, 47-55.

Murakami, H., Hosoi, Y., Sawamura, Y. & Ikeda, R. (1992). Wave Induced Flow Around Submerged Vertical and Horizontal Plates. *Proc. 39th Coastal Engng. Conf. JSCE*, 39, 571-575. (In Japanese)

Thielicke, W. & Stamhuis, E. J. (2014a). PIVlab - Time-Resolved Digital Particle Image Velocimetry Tool for MATLAB. Figshare. *Journal of Open Research Software*, 2(1), e30.

Thielicke, W. & Stamhuis, E. J. (2014b). PIVlab - Towards User-Friendly, Affordable and Accurate Digital Particle Velocimetry in MATLAB. *Journal of Open Research Software,* 22(1), e30.

RECENT PROGRESS ON THE SUSTAINABLE ENERGY SYSTEMS IN SMART CITIES

HUI QIAN YOONG[1], LAI KUAN LEE[2], NOR AZAZI ZAKARIA[3] & KENG YUEN FOO[4]

[1,3,4] River Engineering and Urban Drainage Research Centre (REDAC),
Universiti Sains Malaysia, Engineering Campus, Nibong Tebal, Penang, Malaysia,
clarehuiqian@gmail.com; redac01@usm.my; k.y.foo@usm.my
[2] School of Industrial Technology, Universiti Sains Malaysia, Penang, Malaysia,
l.k.lee@usm.my

ABSTRACT

Sustainable development remains a comprehensive and complex interplay between the population growth, urbanization, economic development, and the living environment. During the last few years, the concept of "sustainability" has become the common interest among the scientific community. An important criterion for the translation of "sustainability" into the action plan is the establishment of the compatible energy supply and applications. This transition to sustainable energy systems has to be initiated in the urban areas, with the total energy consumption of up to 75%, and the emissions of greenhouse gases of 80%. Today, approximately 50% of the world's population are staying in urban cities, and the figure is expected to be exceeding 60% by 2025. In parallel to this development, the novel concept of "smart city", with the new integration of sustainable energy systems have been highly promoted. The present work was conducted to update the unique concept of smart cities, and the successive implementation of sustainable energy systems. The comprehensive profiles of the applications of a variety of green energy, including the solar, geothermal, wind, hydrogen fuel cell, and biomass energy are elucidated. Additionally, the available supporting practices, together with the major key barriers for the innovation of sustainable energy practice are outlined.

Keywords: Smart cities; smart energy system; sustainable energy; zero-energy building.

1 INTRODUCTION

Sustainable development can be regarded as the development that meets with the present needs without compromising the advantages of the future generations. The concept of sustainability has gained popularity with major focus being placed on the developing cities with dense population growth, fast economic growth and huge consumption of a variety of resources. In parallel to this evolution, the unique concept of "smart city' has been established, with the integration of information, communication technology (ICT) network and smart energy systems as the essential components to sustainability. Energy, a stimulus of the sustainable development, is a supporting tool contributing to the successive implementation of the concept of "smart city". According to International Energy Agency, a 53% increase in global energy consumption is foreseen by 2030, consisting mainly 34.8% of crude oil, 29.2% of coal and 24.1% of natural gas. These growth trends have attracted an aesthetic concern connected to the limitations of sustainable energy supply, and the resulting competition of natural resources (Foo, 2015).

Extensive researches have been directed to the exploration of renewable energy, to fulfill the global energy demand and ascertain the preservation of the natural environment. In particular, renewable energy has been put in the limelight in upgrading the efficiency of the existing power resources. Various efforts were undertaken to embark the development of renewable energy resources, notably solar, wind, geothermal, bioenergy, and hydrogen for energy generation in these smart cities. With the aforementioned, this present paper attempts to highlight the novel concept of smart cities. The unique linkages with the sustainable and renewable energy system, and the successive implementations of solar energy, wind power, geothermal, biomass and hydrogen are addressed. The supporting practices and major key barriers are outlined.

2 SMART CITIES

2.1 Conceptual understanding

In the early 1970s, the notion of "wired city", which stressed on the role of ICT network, was introduced to foster the rapid development of urban populations. The concept of "intelligent city", with the integration of cognitive sphere from "wired city", and primarily relies on top-down policies, was then introduced. This intelligent city vision excluded the element of the "people-centered" dimension. The emergence of "creative city" has highlighted the opposite trend (bottom-up participation), that relies mainly on the community-based and private sector initiatives, living labs and social entrepreneurship. Smart city is the hybrid model of both intelligent and creative cities (Ben Letaifa, 2015), with the consideration of "environmental sustainability"

(Andrea and Chiara, 2016). The common definitions of "smart city" are given in Table 1, and Figure 1 illustrates the map of the smart cities worldwide (Cocchia, 2014).

Table 1. Common definitions of "smart city".

Definition	Reference
Smart cities are the urban center of the future, made safe, secure, environmentally green, and efficient because all structures—whether for power, water and transportation, are designed, constructed and maintained making use of advanced, integrated materials, sensors, electronics, and networks, which are interfaced with computerized systems comprised of databases, tracking, and decision-making algorithms.	Bowerman et al. (2000)
Safe, secure and environmental efficient urban centre of the future with advanced infrastructures such as sensors, electronic devices and networks to stimulate sustainable economic growth and a high quality of life.	Hall (2000)
A smart community is a community that has made a conscious effort to use information technology to transform life and work within its region in significant and fundamental rather than incremental ways.	California Institute (2001)
A city connecting the physical, information technology, social, and business infrastructures to leverage the collective intelligence of the city.	Hartley (2005)
A city well performing in a forward-looking way in economy, people, governance, mobility, environment, and living, built on the smart combination of endowments and activities of self-decisive, independent and aware citizens.	Giffinger et al. (2007)
The use of Smart Computing technologies to design and improve the critical infrastructure components and services of a city- which includes city administration, education, healthcare, public safety, real estate, transportation, and utilities- more intelligent, interconnected, and efficient.	Hollands (2008); Belissent (2010)
Smart city is defined as the use of information and communication technology to sense, analyze and integrate the key information of core systems in running cities.	IBM (2010)
A city which implements ICT and Web 2.0 technology with other organizational design and planning efforts to dematerialize and speed up bureaucratic processes, identify new, innovative solutions to city management complexity, and to improve the sustainability and livability.	Toppeta (2010)
A city that monitors and integrates conditions of all of its critical infrastructures, to organize its resources, plan its preventive maintenance activities, and monitor security aspects while maximizing its services.	Washburn et al. (2010)
It is the implementation and deployment of information and communication technology infrastructures to support social and urban growth by improving the economy, citizens' involvement and governmental efficiency.	Caragliu et al. (2011)
A smart city is a healthy, energy-efficient city that applies renewable energy sources as much as possible, and is a pioneer in the deployment of advanced smart technologies.	EUROCITIES (2011)
Smart city is an integrated initiatives oriented at improving the quality of life, sustainability and efficient management of services, while innovating the materials, resources and models used, and using technology in an intensive manner.	CTECNO (2012)
Smart city is an urban laboratory, an urban innovation ecosystem, a living lab, and an agent of change.	Schaffers et al. (2012)
Smart City is a city with water recycling, advanced energy grids and mobile communications to reduce the environmental impacts, and offer the citizens for a better quality of life.	Setis-Eu (2012)
A smart city is a well-defined geographical area, in which high technologies such as ICT, logistic and energy production are cooperated for the benefits of well-being, inclusion and participation, environmental quality and intelligent development.	Dameri (2013)

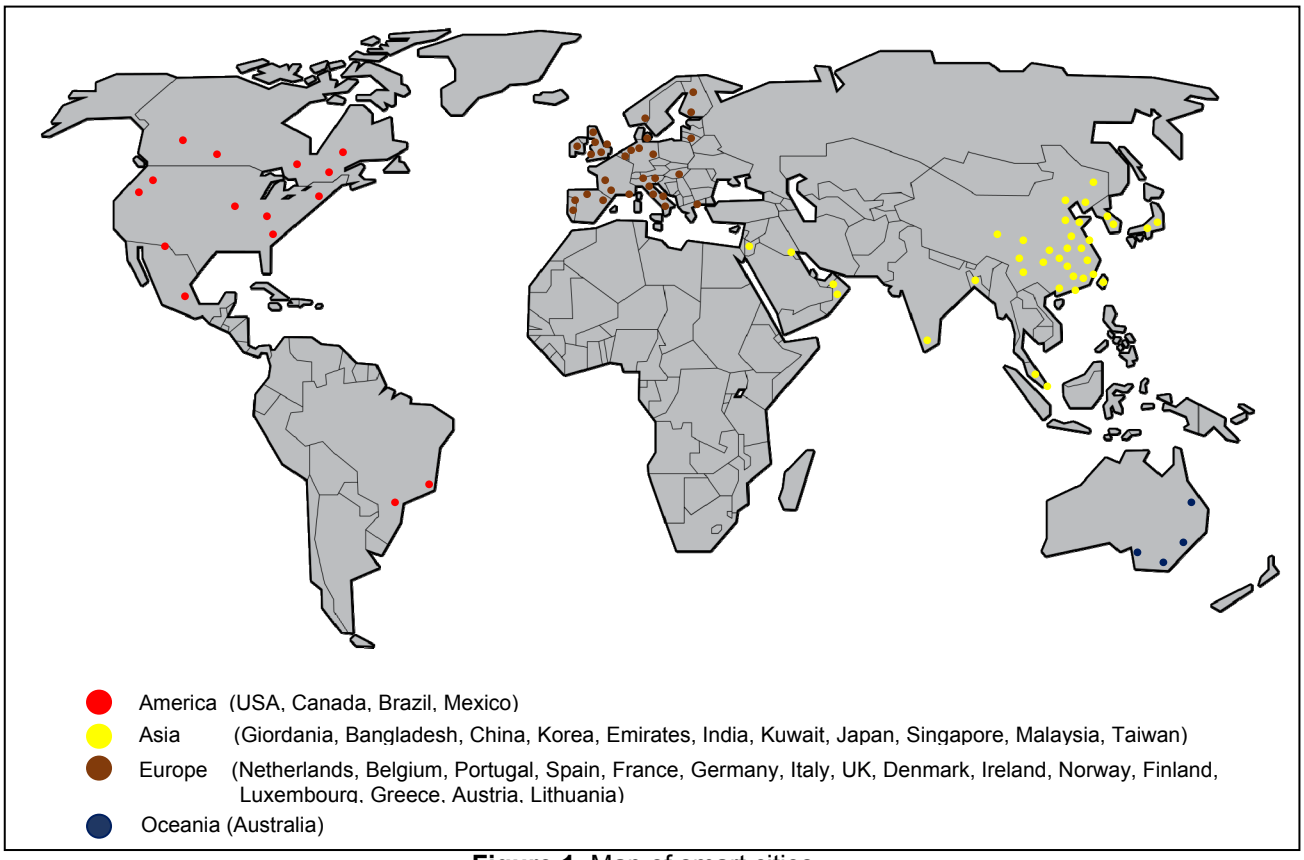

Figure 1. Map of smart cities.

According to Boyd (2013), the six common indicators of smart cities are smart economy, smart environment, smart governance, smart mobility, smart living and smart people. The six Cohen's domains could also be regarded as natural resources and energy, transport and mobility, buildings, living, government, economy and people, with each domain has its sub-domains (Neirotti et al., 2014). According to Madakam and Ramaswamy (2016), smart governance and smart education, smart healthcare, smart building, smart mobility, smart infrastructure, smart technology, smart energy and smart citizen are the major components of a smart city. It is also related to the five main building blocks: Economic, social and privacy implications; developing e-government; health, inclusion and assisted living; intelligent transportation systems; smart grids, energy efficiency and environment (Luis et al., 2015). The development of smart cities relies primarily on the essential principle backbones of the digital infrastructure, data management, renewable energy, smart buildings and smart transport (Deakin and Reid, 2017).

2.2 Smart cities and sustainable energy

From an energy modeling perspective, a smart city is a collection of nodes and links. The nodes represent energy sources or energy sinks, while the links are the conduits which energy flow between the sources and the sinks throughout the city. The relevant components in smart cities include energy supply, energy networks, energy demand and energy storage. The supply in smart cities is the energy sources that generate energy at distributed micro-generation sites (combined heat and power plants) or more contemporary renewable sites (solar and wind farms or hydroelectric dams) (William et al., 2014). Energy networks are the connecting links between the sources and the sinks, and smart grids are the electricity networks integrating the actions of consumers, producers and prosumers for a sustainable, economic and efficient electricity supply. A smart grid plays three major governing roles. Firstly, the power system is modernized by smart grid through automation, remote monitoring and control, self-healing designs and micro-grids (Mariacristina et al., 2013). Secondly, consumers are informed and educated by smart grid regarding their energy usage, costs and options. Thirdly, they provide safe, secure and reliable integration of distributed and renewable energy resources.

The energy demand, also known as energy sinks could be referred to buildings, electrified transport system or public services that implement the key focus of "zero-energy", "nearly zero-energy" or "net zero-energy" concept (Laura and Helder, 2014). Energy storage is related to facilities where energy could be retained for use at a later date, including batteries of electric vehicles and photovoltaic (PV) systems for discrete, local storage, and large-scale grid energy storage sites such as pumped storage hydroelectricity and compressed air and flywheels that are expected to integrate renewable source to be delivered to demand-

response schemes. Energy storage could be integrated at different levels of electricity system in smart city, mainly generation level (arbitrage, balancing and reserve power), grid level (frequency control, investment deferral, voltage control and capacity support) and customer level (peak shaving, time of use and cost management) (Calvillo et al., 2016).

The smart energy system is derived from 100% of renewable energy, with bioenergy and intermittent renewable energy as the two major forms of energy production. It may be divided into 3 main grid infrastructures: smart electricity grids which connect flexible electricity demands; smart thermal grids connecting electricity and heating sectors, and smart gas grids connecting the electricity, heating, and transport sectors to enable the utilization of gas storage, with additional flexibility (Borna, 2016). In the perspective, Internet of Energy (IoE) is the integrated dynamic network infrastructure that is established according to the standard and interoperable communication protocols, which interconnects the energy network with a variety of operational and energy measures, including smart meters, smart appliances, renewable energy resources, energy efficiency resources, and control of the production and distribution of electricity (Michal, 2016).

3 THE UNIQUE PROFILE AND IMPLEMENTATION OF SUSTAINABLE ENERGY

Solar energy is a renewable source that could be applied for electricity or heat production via the photovoltaic (PV) system when they are illuminated by solar radiation photons (Mourad et al., 2014). It could lower the energy demand, and minimize the use of new land by the integration into the envelope. In regards to this, there are two major options which PV could be applied: Building Added PV (BAPV) and Building Integrated PV (BIPV) (Scognamiglio et al., 2014). According to International Energy Agency, these PV applications could be divided into four main categories, namely off-grid domestic, off-grid non-domestic, grid connected distribution, and grid connected centralization (Khare et al., 2013). PV shingle (PV panel roof) systems provide the collection of considerable amount of solar energy from building and garage roofs, that could be applied for lighting at night and charging of electrical equipment, vehicles and air conditions (Murat et al., 2016). It is a reliable source for heating applications, and usually implemented as concentrated solar-power (CSP) plants for utility-scale electricity generation (Calvillo et al., 2013).

Whereas, wind energy is the kinetic energy associated with the movement of large masses of air, from the uneven heating of atmosphere by sun, resulting temperature, density and pressure difference. Wind power is the conversion of wind energy into a useful form of energy, for the operation of wind turbines to generate electrical power at top or between high buildings, skyscraper, towers and hills in the cities (Murat et al., 2016), windmills for mechanical power, and wind pumps for water pumping (Khare et al., 2013). Geothermal energy, derives from the thermal energy flux from the centre of the earth (Calvillo et al., 2013), is the resource identified for geothermal heating and cooling. The early type is the very low temperature, in the range of the mean air temperature of up to 30 °C, based on the relatively stable groundwater and ground temperatures at a shallow depth. Typically, heat pumps are applied for the extraction of energy from the ground, and raise to the desired temperature by the heating systems. Another type of geothermal energy, lies at low and medium temperature, ranging from 30 to over 100 °C, where heat is extracted from the ground and groundwater at higher temperatures, typically at a greater depth. The thermal heat from the geothermal resources is a key energy solution to a broad range of industrial activities through the underground thermal storage (Philippe, 2016).

Biomass, or defined as the residual sources of wood, crops, straws and biogas, is incinerated in a solid or gaseous form, mostly in combined heat and power (CHP) units for the generation of electricity and heat. Figure 2 illustrates a typical process of the biomass conversion technology (Aslani et al., 2013). Although biomass energy is regarded as a renewable energy source, the implementation has been conducted in a sustainable way that it will not induce large scale emission of the greenhouse gases (GHG) (Borna, 2016). Hydrogen is a worldwide-accepted clean energy carrier, and is considered to be the clean fuel of the future, particularly for energy storage and transport, as it is source-independent, and has a high energy content per mass as compared to petroleum (Becherif et al., 2015). The hydrogen technologies include electrolysis and gas storage. It can be produced by means of electrolysis of water without pollutants production that could be stored as chemical energy. The easiest and cheapest way to accumulate hydrogen is to compress it up to a pressure of 200-250-350 bar in special tanks, which is suitable for residential users' applications (Paolo et al., 2015). Table 3 shows a comparison of the most common distributed sustainable energy sources in the smart cities (Calvillo et al., 2016).

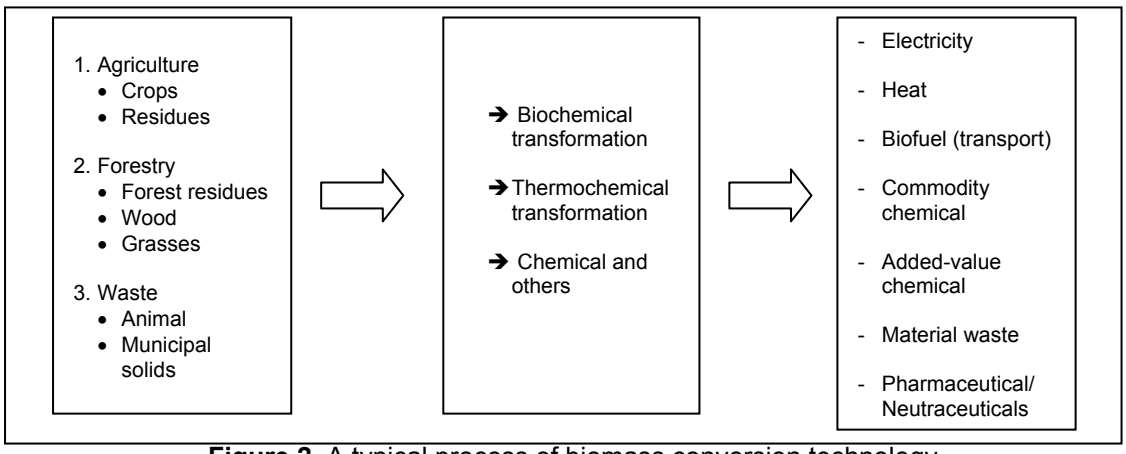

Figure 2. A typical process of biomass conversion technology.

Table 3. Comparison of the most common distributed renewable energy sources.

Type	Generated Power		Dispatchable	Efficiency	Common application
	Electric	Thermal			
Solar PV	Yes	No	No	Low (<30%)	Household, Buildings
Solar TC	No	Yes	No	Moderate (≤ 60%)	Household, Buildings
Solar PV/T	Yes	Yes	No	Moderate (≤ 60%)	Household, Buildings, District
Solar CSP	Yes (Indirectly)	Yes	Yes	Moderate (≤ 60%)	Thermal: District; Electricity: District, Power Plant
Windpower	Yes	No	No	Moderate (≤ 60%)	District, Power Plant
Biomass	Yes	Yes	Yes	Moderate (≤ 60%)	Thermal: Household, Buildings, District; Electricity: District, Power Plant
Geothermal	Yes (Indirectly)	Yes	Yes	High (>60%)	Thermal: Household, Buildings, District; Electricity: District, Power Plant

Masdar City in Abu Dhabi, United Arab Emirates is the world's first (proposed) smart and zero-carbon city. The city runs on wind (a wind turbine farm), solar, and hydrogen power, in addition to the traditional electricity. The solar power systems with smart lighting systems have been integrated to the central square of the city. Huge umbrella-bodies equipped with photovoltaic systems that feed the public lighting, and some neighbouring buildings were installed in the square. During daytime, these "umbrellas" are opened for heat storage and during nighttime, they will act as large lamp posts that slowly releases the heat for huge thermal excursion (Eleonora et al., 2015). Similarly, the International Renewable Energy Agency (IRENA)'s Global Head Quarter (HQ), located in Masdar Smart City, has been well known for the 1,000 m^2 of rooftop photovoltaic panels, together with "beam-down" concentrated solar power plants for electricity generation, to supply 75% of the total annual hot water usage. In addition to this, a solar-powered desalination plant and wind farms and hydrogen power plants, have been established outside the city's outer limits, capable of producing up to 20 megawatts of energy (Madakam and Ramaswamy, 2016). Dongtan, the sustainable design initiative of Shanghai, China, is a self-sufficient energy city featuring zero-energy buildings. The city will run exclusively on solar, wind, and biofuel energy, which the building roofs will hold PV cell arrays, with the installation of wind turbine farms outside and within the city. In Tongshan, China, a centralized biomass boiler running on rice husk for heat generation during winter months has been introduced in the development of new apartments. Zira Island, recognized by the application of sun, wind and water power, is a sustainable beach with the installation of heat pumps, which plunge into the surrounding of Caspian Sea. The solar hot water collectors are integrated into the architecture, while photovoltaics on strategically angled facades and roof tops would generate electricity for the total energy requirement (Aktuğlu Aktan, 2014).

In Bangladesh, Dhaka South City Corporation has installed solar panels on 61 street lamp posts from Kakrail to Notre Dame College via Fakirapool to reduce the large dependency on the power grid, under "Solar Photovoltaic-powered LED Street Lighting" project (Rahnuma et al., 2013). In Japan, the Smart Hydrogen Station (SHS) that supplies hydrogen produced from electrolysis of water, together with the solar photovoltaic panels, have been constructed in the Gotandacho district in Tottori City. Within this district, an existing Sekisui House exhibition building has been turned into a 'smart' house, with the total power consumption supplied from the fuel cells. Meanwhile, the carbon-neutral hydrogen supply chain powered by renewable wind energy is applied on its east coast, near to the cities of Yokohama and Kawasaki. In implementing the project, electricity generated by the Yokohama City Wind Power Plant is applied for hydrogen gas generation that would be transported to the Keihin region for the application of fuel cell powered forklift trucks and fresh produce markets (FCB, 2016). In Morahalom, Italy, a cascade system is designed to fully exploit the return water of the thermal bath at 28°C-35°C for the heating of domestic water for several cultural and administrative facilities in the town centre. The cascade system is fueled by a heat pump powered by a

combined heat and power unit that applies methane gas from the geothermal extraction well. In Galanta, Italy, an existing geothermal cascade system fueled by water at 90°C is extended to cover a broad variety of heating and domestic hot water demand of the recently retrofitted buildings (Valentina and Roberto, 2015). An overview of different collective or municipal production of renewable energy sources, and its application in some European cities is presented in Table 4 (Groth et al., 2016).

Table 4. Collective/municipal renewable energy generation in European cities.

Energy supply technologies	Eskilstuna, Sweden	Turku, Finland	Jyväskylä, Finland	Tartu, Estonia	Stoke-on-Trent, UK	Santiago de Compostela, Spain
Ground source heat pumps		✓	✓			
Deep geothermal					✓	
Solar (solar farms)	✓	✓	✓	✓	✓	✓
Wind	✓		✓			
Biogas from waste	✓		✓	✓		

4 SUPPORTING PRACTICE AND MAJOR KEY BARRIERS

4.1 Supporting practice

The concept of “smart city”, is a major movement between 1995 and 2005, with the notations of “creative city”, “digital city”, and “knowledge city” (Marsal-Llacuna, 2016). One of the great recognized smart cities initiatives is the “Smart Cities and Communities European Innovation Partnership”, which was launched in July 2012, with the major aim to stimulate the development of smart technologies in cities within the fields of energy, transportation and ICT (Crivello, 2015). The operational implementation plan of the European Innovation Partnership on Smart City and Communities has highlighted “Districts and Built environment” as the priority area for the implementation of new technical building solutions and building automations, holistic measures for smart energy networks, energy storages and final energy use management. Several pilot energy actions were established at community and district scale, within the CONCERTO initiative of the former European Research framework (FP6 and FP7), with the objective to enhance the growth of renewable energy in the built environment. The outcomes constitute a valuable background of applied solutions for the future Smart Cities and Communities projects (Valentina and Roberto, 2015). A typical example is the Geothermal Communities (GEOCOM) project that implements sustainable solutions for the exploitation of geothermal energy on a neighbourhood and community scale, with the innovation of renewable energy resources and retrofitting measures for the existing buildings. Under the 6FP (Priority 6.1-Sustainable Energy Systems), the POLYCITY project was introduced to promote the installation of combined heat and power (CHP) system for the medium voltage grid (Barbara et al., 2011). Nice Grid is a demonstration project led by ERDF (European Regional Development Fund), the main French distribution network operator to develop a smart solar neighbourhood in Carros, an urban city of Nice, France. It was partly sponsored by ADEME (*Agence de l'Environnement et de la Maîtrise de l'Énergie*- French Environment and Energy Management Agency) under the initiative “*Investissements d'Avenir*” and the European Commission, under the 7th framework program (7FP) (Michiorri et al., 2012). Under 7FP, the PLEEC (Planning for Energy Efficient Cities) project was funded with the general aim to build a sustainable, energy-efficient, smart city (Kullman et al., 2016).

The European Strategic Energy Technology Plan (SET-Plan) has commenced since 2010 through the European Industrial Initiatives, to provide the basis for planning and decision-making. The Industrial Initiatives within the SET-Plan are the Wind Initiative, Solar Europe Initiative–photovoltaic and Concentrated Solar Power, the Electricity Grid Initiative, Carbon Capture, Transport and Storage Initiative, the Sustainable Nuclear Initiative, the Industrial Bioenergy Initiative, the Smart Cities & Communities Initiative and the Joint Technology Initiative on Fuel cells and Hydrogen. Within the framework, fuel cells and hydrogen energy is one of the eight technology initiatives identified by the European Strategic Energy Technology Plan to stimulate the European energy system. Within the EU Energy and Climate Policy, the European Commission has initiated the Fuel Cell and Hydrogen Joint Undertaking in 2008, a European Task Force on Energy storage (2009) and the European Association for storage of Energy, among the manufacturers, utilities and academics bodies (2011). Energy Roadmap 2050, a new sense of collective responsibility was brought to the development of new energy infrastructures and storage capacities across the European smart cities (Becherif et al., 2015). EERA (European Energy research Alliance) JP (Joint Programme) on Smart Cities is one of the primary initiatives launched within the European SET-Plan, a technology pillar of EU's energy and climate policy to highlight the integration of new energy technologies in smart cities, that can be divided into 4 sub-programmes: Energy in Cities, Urban Energy Networks, Energy-efficient Interactive Buildings, and Urban City-related Supply Technologies (Laura et al., 2016). SET-Plan and the “Smart Cities & Communities Initiative” encourage cities and regions to progress by 2020 towards a 40% reduction of greenhouse gas (GHG) emissions through the sustainable use and production of energy. This initiative aims to pool resources to support the demonstration of energy, transport and information and communication technology in European

urban areas, and aspires that 25–30 European cities will be at the forefront of the transition to a low carbon economy by 2020. This target is expected to be achieved through the adoption of systemic approaches and organisational innovation, including energy efficiency, low carbon technologies and smart management of supply and demand, and focus more on buildings measures, local energy networks and transport. The progress of the indicative roadmap of the “Smart Cities & Communities Initiative” will be monitored and assessed through the Key Performance Indicators (KPIs), including the integration of RE in buildings, heating and cooling, electricity, transport and smart grids (Kylili and Fokaides, 2015).

Other initiatives relevant to the ideas of optimizing energy use or integration of renewable energy in smart cities are often promoted at the international level. In the framework of FINSENY (Future Internet for Smart Energy) initiative, future internet technologies are exploited for the development of Smart Energy infrastructures, to enable the new functionalities at reducing costs. In the framework of RESSOL-MEDBUILD (RESearch Elevation on Integration of SOLar Technologies into MEDiterranean BUILDings), simulation models are developed for the optimization of building energy management and energy performance. TRACE (Tool for Rapid Assessment of City Energy) is a DSS (Decision Support System) tool designed, and implemented by WorldBank within the Energy Sector Management Assistance Program (ESMAP) to assist municipal authorities in identifying and prioritizing Energy Efficiency actions, for the efficient management in passenger transport, municipal buildings, public lighting, power and heat in smart cities. SCEAF (Smart City Energy Assessment Framework) is another initiative directed "Smart Cities" to energy optimization by highlighting the strengths, vulnerabilities and the opportunities arising from the existing energy strategy, environmental policy, municipal facilities and related infrastructures. One of the critical components in SCEAF is the Energy & Environmental Profile. This profile evaluates the energy consumption intensity of the city, the penetration degree of renewable energy sources (RES), the efficiency of the city energy networks and its energy conservation features, and the emission intensity. The evaluation of these pillars is based on the city-level data, including energy consumption of municipal buildings, households, commercial buildings, public transport, municipal fleet, water treatment units, recycling centers and other related facilities. In the Turin city of Italy, “Sustainable Energy Action Plan” (TAPE—Turin Action Plan for Energy) was established in 2010, and three projects were presented: “EeCoFit”, concerning the energy upgrading of buildings and infrastructures; “Energy Smart Cities”, concerning the application of innovative energy storage; and “E.Plan”, concerning the development of databases on urban sustainable planning in the energy management (Crivello, 2015). Accordingly, in Belgium, the East Loop project which integrated renewable energy in an active network management technology, has been reported. In Spain, the projects SCALA, STAR and SMARTCITY, smart meters were installed in more than 190,000 households under the FutuRed initiative to facilitate the application of renewable and electric vehicles on the distribution network (Michiorri et al., 2012). The International Standards Organization (ISO) was the first international normalization body which has initiated the standardization works in the domain of smart cities. In parallel to the introduction of ISO, other organizations included AENOR in Spain and AFNOR in France have placed the steps to complete this development (Marsal-Llacuna, 2016.

4.2 Major key barriers

In conjunction to the successive development of smart city with the innovation of sustainable energy systems, the main barrier of the implementation is the investment cost barrier with inconsistent financial support. Companies, which are interested in implementing RE, have to bear with the upfront costs, and wait for a longer payback period to get returns on their investments. Fragmentation of legal and institutional frameworks is another significant initiative to be complied and integrated (Balaban and Puppim de Oliveira, 2016). Moreover, some of the relevant policies are not updated and developed in-time, to effectively provide a guideline for the sustainable energy applications. In present, regulatory requirements for RE in many countries are still not mandatory, and on voluntary basis (Shukla et al., 2015). Other blocks to the RE implementation, especially in developing countries, are seasonal fluctuations, weather, locations, limitation to the adoption of emerging technologies, limited technical supports and trainings, and requirement of additional studies and professional researches (Saleh and Faeiza, 2016). The improper services provided by the energy service companies that lead to poor perception and awareness about the viability of RE technologies, are some of the major drawbacks to retard the practical application of renewable energy. In addition, there are also arguments about the direct or indirect harmful implications of RE to the natural environment, ecosystem and human welfare, from some parties who are skeptical to the role of renewable energy (Foo, 2015).

5 CONCLUSIONS

To date, the depletion and the tremendous pressure on the fossil fuels has driven the global concern and the race to the alternative green energy, and evolution of sustainable energy systems. Together with the new introduction of the “smart city”, both government and non-governmental organizations (NGOs) continue to advocate a multidisciplinary of technical and non-technical efforts to adopt a new constructive framework to transform the new cities into a high quality and excellent level. The plan espouses the new implementation of solar, geothermal, wind, hydrogen fuel cell, and biomass energy. Subsets to this development, the

cooperation between different parties, international focus and a great deal of supporting policies need to be pursued continuously to speed up the process, in creating a sustainable oriented cities, toward building a sustainable future.

ACKNOWLEDGEMENTS

The authors acknowledge the financial support provided by the Ministry of Higher Education of Malaysia under the PRGS research grant scheme (Project No. 203/PREDAC/6740022).

REFERENCES

Aktuğlu Aktan, E.Ö. (2014). Carbon Reduction with Solar Energy in Cities. *WIT Transactions on Ecology and the Environment*, 190, 959-970.

Andrea, C. & Chiara, F.D.B. (2016). Do Smart Cities Invest in Smarter Policies? Learning from the Past, Planning for the Future. *Social Science Computer Review*, 34(6), 657-672.

Aslani, A., Helo, P., Feng, B., Antila, E. & Hiltunen, E. (2013). Renewable Energy Supply Chain in Ostrobothnia Region and Vaasa City: Innovative Framework. *Renewable and Sustainable Energy Reviews*, 23, 405-411.

Balaban, O. & Puppim de Oliveira, J.A. (2016). Sustainable Buildings for Healthier Cities: Assessing the Co-Benefits of Green Buildings in Japan. *Journal of Cleaner Production*, 1-11.

Barbara, B., Luca, G., Alessandara, G. & Paolo, L. (2011). Energy Networks in Sustainable Cities: Towards a Full Integration of Renewable Systems in Urban Area. *IECON 2011-37th annual conference on IEEE industrial electronics society*, 3146-3151.

Becherif, M., Ramadan, H.S., Cabaret, K., Picard, F., Simoncini, N. & Bethoux, O. (2015). Hydrogen Energy Storage: New Techno-Economic Emergence Solution Analysis. *Energy Procedia*, 74, 371-380.

Belissent, J. (2010). 'Getting Clever About Smart Cities: New opportunities Require New Business Models'. *Forrester Research*, 1-33.

Ben Letaifa, S. (2015). How to Strategize Smart Cities: Revealing the SMART Model. *Journal of Business Research*, 68, 1414-1419.

Borna, D. (2016). Research Project «Sunstore 4» 100% Renewable District Heating for Smart Cities. *MSc Thesis*, University of Zagred.

Bowerman, B., Braverman, J., Taylor, J., Todosow, H. & Von Wimmersperg, U. (2000) 'The Vision of a Smart City'. Paper presented at 2nd International Life Extension Technology Workshop, Paris, 1-7.

California Institute (2001). Available: http://smartcommunities.org/concept.php [Accessed 01/02/2017]

Calvillo, C.F., Sánchez, A. & Villar, J. (2013). Distributed Energy Generation in Smart Cities. *International Conference on Renewable Energy Research and Applications*. Madrid: IEEE, 161-166.

Calvillo, C.F., Sánchez, A. and Villar, J. (2016). Energy Management and Planning in Smart Cities. *Renewable and Sustainable Energy Reviews*, 55, 273-287.

Caragliu, A., Del Bo, C. & Nijkamp, P. (2011). Smart cities in Europe. *Journal of Urban Technology*, 18(2), 65–82.

Cocchia, A. (2014). *Smart and Digital City: A Systematic Literature Review*. Smart City, 1st ed. Switzerland: Springer International Publishing, pp. 14-43.

Crivello, S. (2015). Urban Policy Mobilities: The Case of Turin as a Smart City. *European Planning Studies*, 23(5), 909-921.

CTECNO (2012). 'Hoja de ruta para la smart city'. Available at http://www.ctecno.net/wp-content/uploads/2012/03/Hoja-de-Ruta-Smart-Cities_def.pdf (Accessed 25 Feb. 2017).

Dameri, R. P. (2013). Searching for Smart City Definition: a Comprehensive Proposal. *International Journal of Computers & Technology*, 11(5), 2544–2551.

Deakin, M. & Reid, A. (2017). Smart Cities: Under-Gridding the Sustainability of City-Districts as Energy Efficient-Low Carbon Zones. *Journal of Cleaner Production*, 1-10.

Eleonora, R.S., Gianluca, S., Valentina, V., Gaetano, Z. & Silvia, P. (2015). Smart City and Public Lighting. In *Environment and Electrical Engineering (EEEIC), 2015 IEEE 15th International Conference on*, 665-670.

EUROCITIES (2011). Response to Public Consultation on Smart Cities & Communities initiative. Available at www.eurocities.eu, (Accessed 25 Feb. 2017).

FCB (2016). Honda Joins Japanese Hydrogen Energy Demo in Tottori Prefecture. *Fuel Cells Bulletin*, p. 7.

Foo, K.Y. (2015). A Vision on the Opportunities, Policies and Coping Strategies for the Energy Security and Green Energy Development in Malaysia. *Renewable and Sustainable Energy Reviews*, 51, 1477-1498.

Giffinger, R., Fertner, C., Kramar, H., Kalasek, R., Pichler-Milanovic, N. & Meijers, E. (2007). *Smart cities. Ranking of European medium-sized cities*. Vienna: University of Technology, 1-28.

Groth, N.B., Fertner, C. & Grosse, J. (2016). Urban Energy Generation and the Role of Cities. *Journal of Settlements and Spatial Planning*, 5, 5-17.

Hall, P. (2000). Creative Cities and Economic Development. *Urban Studies*, 37(4), 633–649.

Hartley, J. (2005). Innovation in Governance and Public Services: Past and present. *Public Money & Management*, 25(1), 27-34.

Hollands, R. G. (2008). Will the Real Smart City Please Stand Up? *City: Analysis of Urban Trend, Culture, Theory, Policy, Action*, 12(3), 303–320.
IBM (2010). Smarter Thinking for a Smarter Planet.
Khare, V., Nema, S. & Baredar, P. (2013). Status of Solar Wind Renewable Energy in India. *Renewable and Sustainable Energy Reviews*, 27, 1-10.
Kullman, M., Campillo, J., Dahlquist, E., Fertner, C., Giffinger, R., Groose, J., Groth, N.B. & Haselberger, J. (2016). Note: The PLEEC Project –Planning for Energy Efficient Cities. *Journal of Settlements and Spatial Planning*, 5, 89.
Kylili, A. & Fokaides, P.A. (2015). European Smart Cities: the Role of Zero Energy Buildings. *Sustainable Cities and Society*, 15, 86-95.
Laura, A. & Helder, G. (2014). From Solar Building Design to Net Zero Energy Buildings: Performance Insights of an Office Building. *Energy Procedia*, 48, 1236-1243.
Laura, A., Ana, F., Claudia, S.M., Richardo, G., Helder, G., Susana, C. & Carlos, S. (2016). Smart City: A Systematic Approach Towards a Sustainable Urban Transformation. *Energy Procedia,* 91*,* 970-979.
Luis, G.M.B., Óscar, Á & Jan, M. (2015). Quality of Experience (QoE) in the Smart Cities Context: An Initial Analysis. *In Smart Cities Conference (ISC2), 2015 IEEE First International*, 1-7.
Madakam, S. & Ramaswamy, R. (2016). Sustainable Smart City: Masdar (UAE) (A City: Ecologically Balanced). *Indian Journal of Science and Technology*, 9(6).
Mariacristina, R., Michela, L. & George, C.L. (2013). Smart City By Multi-Agent Systems. *International Conference on Renewable Energy Research and Applications*. Madrid: IEEE, 371-376.
Marsal-Llacuna, M.-L. (2016). City Indicators on Social Sustainability as Standardization Technologies for Smarter (Citizen-Centered) Governance of Cities. *Social Indicator Research*, 128, 1193-1216.
Michal, L., Ondrej, P. & Miroslav, S. (2016). Industry 4.0 as a Part of Smart Cities. *Smart Cities Symposium Prague 2016*. IEEE, 1-6.
Michiorri, A., Girard, R., Kariniotakis, G., Lebossé, C. & Albou, S. (2012). A Local Energy Management System for Solar Integration and Improved Security of Supply: the Nice Grid Project*. 3rd IEEE PES Innovative Smart Grid Technologies Europe (ISGT Europe)*. Berlin, IEEE, 1-6.
Mourad, M.M., Ali, A.H.H., Ookawara, S., Abdel-Rahman, A.K. & Abdelkariem, N.M. (2014). An Energy-Efficient Smart Home for New Cities in Egypt. *WIT Transactions on Ecology on The Built Environment*, 142.
Murat, A., Asim, K., Abdulkerim, K., Serkan, A., Baris, B.A. & Cemal, K. (2016). Opportunities for Energy Efficiency in Smart Cities. IEEE, 1-19.
Neirotti, P., Marco, A.D., Cagliano, A.C., Mangano, G. & Scorrano, F. (2014). Current Trends in Smart City Initiatives: Some stylised facts. *Cities*, 38, 25-36.
Paolo, G.M., Roberto, B., Roberto, I. & Stefano, M. (2015). Solar Energy System in a Small Town Constituted of a Network of Photovoltaic Collectors to Produce Electricity for Homes and Hydrogen for Transport Services of Municipality. *Energy Procedia*, 78, 824-829.
Philippe, D. (2016). A European Perspective of the Development of Deep Geothermal in Urban Areas: Smart Thermal Grids, Geothermal Integration into Smart Cities. *Geomechanics and Tunnelling,* 9(5), 447-450.
Rahnuma, R.C., Muhammad, S.K. & Muhammad, A.A. (2013). Electrification of Streets of Dhaka City Using Smart Solar System. *In Informatics, Electronics & Vision (ICIEV), 2013 International Conference on*, 1-4.
Saleh, M.A. & Faieza, A.A. (2016). Review of Green Building Index in Malaysia: Existing work and challenges. *International Journal of Applied Engineering Research*, 11(5), 3160-3167.
Schaffers, H., Ratti, C. & Komninos N. (2012). Special Issue on Smart Applications for Smart Cities—New Approaches to Innovation: Guest Editors' Introduction. *Journal of Theoretical and Applied Electronic Commerce Research*, 7(3), ii-v.
Scognamiglio, A., Adinolfi, G., Graditi, G. & Saretta, E. (2014). Photovoltaics in Net Zero Energy Buildings and Clusters: enabling the smart city operation. *Energy Procedia*, 61, 1171-1174.
Setis-Eu (2012). *European Initiative on Smart Cities,* Strategic Energy Technologies Information System, European Comission.
Shukla, A., Renu, S. & Shukla, P. (2015). Achieving Energy Sustainability Through Green Building Approach. *Energy Sustainability through Green Energy*, 147-162.
Toppeta, D. (2010). The Smart City Vision: How Innovation and ICT Can Build Smart, "Livable", Sustainable Cities: The Innovation Knowledge Foundation. Available at http://www.thinkinnovation.org /file/research/23/en /Toppeta_Report_005_2010.pdf (Accesced 25 Feb. 2017).
Valentina, M. & Roberto, P. (2015). Chasing Smart Communities standards: Lesson Learnt from Geothermal Communities Project in Montieri (Italy). *Energy Procedia*, 78, 681-686.
Washburn, D., Sindhu, U., Balaouras, S., Dines, R.A., Hayes, N.M. & Nelson, L.E. (2010). *Helping CIOs Understand "Smart City" Initiatives: Defining the Smart City, its Drivers, and the Role of the CIO*. Cambridge, MA: Forrester Research, Inc, 1-17.
William, J.N.T., Oliver, K. & Biswajit, B. (2014). Demand-Side Characterization of the Smart City for Energy Modelling. *Energy Procedia*, 62, 160-169.

Proceedings of the 37th IAHR World Congress
August 13 – 18, 2017, Kuala Lumpur, Malaysia

UNDERGROUND PUMPED HYDROELECTRIC ENERGY STORAGE IN WALLONIA (BELGIUM) USING OLD MINES – HYDRAULIC MODELLING OF THE RESERVOIRS

SEBASTIEN ERPICUM[1], PIERRE ARCHAMBEAU[2], BENJAMIN DEWALS[3] & MICHEL PIROTTON[4]

[1,2,3,4] University of Liege - Argenco Department – Hydraulics in Environmental and Civil Engineering Research Group, Liege, Belgium
s.erpicum@ulg.ac.be; pierre.archambeau@ulg.ac.be; b.dewals@ulg.ac.be; michel.pirotton@ulg.ac.be

ABSTRACT

Pumped Storage Hydroelectricity (PSH) is a well-known and efficient technology to store and release various amounts of electricity. To overcome the problem of available land surface to create new reservoirs, an alternative consists in using underground volumes to build so-called Underground Pumping Storage Hydroelectricity (UPSH) plants. A research project is currently investigating the feasibility of such UPSH plants in Wallonia (Belgium) using abandoned mines and underground quarries. The paper presents the main features of this multidisciplinary project and focuses on the numerical models developed specifically to consider the reservoirs' hydraulics. Indeed, the detailed prediction of the water mass movements in the reservoirs is a key element of a feasibility analysis, as they may affect the turbomachines operation as well as the solicitations of the reservoirs limits. On the other hand, such prediction is challenging because of the complex geometry, the continuous discharge variations and the possible exchanges with the surrounding soil or the interaction with air in underground reservoirs. The application of the hydraulic model to an abandoned slate quarry highlights the usefulness of the approach and also its limitations.

Keywords: Pumped storage hydroelectricity; numerical model; lumped model; water transients; air-water interaction.

1 INTRODUCTION

Energy production from renewable sources is growing fast, taking over from classical fossil or nuclear power plants. At the scale of the electricity grid, the intrinsic intermittence of most of the renewable energies (wind, solar) cannot afford to regulate the produced electricity according to the irregular demand (Evans et al., 2012). Besides grids interconnection to smooth production and demand, means for electricity temporary storage are key elements to ensure the grid stability.

Pumped Storage Hydroelectricity (PSH) is a well-known and efficient technology to store and release various amounts of electricity in various periods of time. Large PSH plants are in operation all over the world, most of them use two surface reservoirs at different elevations. In most parts of Europe, appropriate sites for new classical PSH plants are getting scarce (Steffen, 2012). An alternative consists of using underground volumes as low level reservoirs to build so-called Underground Pumping Storage Hydroelectricity (UPSH) plants (Allen et al., 1984). Compared to the classical solution with two reservoirs at natural ground elevation, the UPSH plant configuration offers advantages such as decreasing the need for ground surface area, exploiting larger chutes than the ground elevation ones or giving a new life to industrial (abandoned) sites.

Such innovative plants are under study, for instance, in Germany, with the project of Prosper-Haniel mine (Alvarado Montero et al., 2015). In this project, new tunnels are planned in the existing coal mine to create a 200 MW plant. A drawback of this solution lies in the cost of excavation of the subterranean reservoir. Another option is then to use existing underground cavities. In this case, however, strong interactions with groundwater could occur (Pujades et al., 2016).

Wallonia, the Southern Region of Belgium, has a rich mining history. Numerous abandoned mines and quarries are located all over the territory, with various volumes and depths leading to storage capacities from a few to tens of MWh. In this context, the Smartwater project (GRID Innovation online, 2017) has been initiated to develop tools to assess the feasibility of the rehabilitation of such end-of-life mines and quarries into medium-size UPSH plants. The project aims at considering legal, environmental, economic, hydraulic, electro-mechanical and geological aspects of existing underground cavities or mines rehabilitation into UPHS plant. In this paper, the reservoirs hydraulics point of view is tackled.

After a brief presentation of the Smartwater project (section 2) and of the main types of underground cavities and mines identified in Wallonia (section 3), the paper presents the corresponding numerical tools which have been developed to model the hydraulics of the reservoirs (section 4). An application to a typical slate mine is presented in section 5 before some conclusions and perspectives.

2 THE SMARTWATER PROJECT

The multidisciplinary Smartwater project is a 3.7 M€ research project partly founded by the Public Service of Wallonia – Department of Energy and Sustainable Building (GRID Innovation online, 2017). It gathers 20 partners including industrials, applied R&D centers, academics and public bodies.

The project started in September 2014 for a period of 3 years. It aims at generating investigation tools to assess the feasibility of the rehabilitation of end-of-life Walloon quarries and mines into medium-sized UPHS plants. The project implements a global approach encompassing legal, environmental, economic, hydraulic, electro-mechanical and geological aspects through 7 work packages (WPs).

Among the 7 WPs, WP5's tasks are to perform an inventory of possible sites in Wallonia, identify typical geological and geometrical configurations and develop numerical tools to predict the groundwater interactions as well as the hydraulic and geomechanical aspects linked to the creation of an UPSH. Indeed, despite the concept of UPSH using existing cavities is attractive, several challenges have to be overcome to be able to assess its feasibility (Archambeau et al., 2016). One could, for instance, list the evaluation of

- The water exchanges between the surrounding soil and the underground reservoir whose sides are not watertight, and their influence on the one hand on ground water level and on the other hand on the UPSH chute,
- The head variation and discharge availability at the pump(s)/turbine(s) location or the pumped/turbined water volumes distribution within a reservoir with a complex geometry made of interconnected volumes distributed over long distances,
- The air/water interaction within a reservoir enclosed in a saturated soil,
- The geomechanical behavior of the underground reservoir sides when submitted to loading/unloading cycles.

The tools developed in the framework of WP5 should be able to provide objective answers to these questions. This paper presents the models specifically developed in this context to model the flows within the typical underground quarries and mines configurations.

3 TYPICAL SITES CHARACTERISTICS

Wallonia has a rich underground mineral extraction history, starting during Neolithic with flint extraction and ending at the end of the 20th century with the closure of the last slate quarry. In the meantime, coal, iron, chalk, slate, metallic ore, and others have been extracted at an industrial level all over the 16844 km² territory area (Archambeau et al., 2016).

An analysis and selection procedure considering the soil characteristics (cohesion, porosity), the geometric data availability, the date of closure and the expected volume of the low-level reservoir showed that coal mines and slate quarries are the most likely underground cavity types to be rehabilitated as UPSH in Wallonia. Their typical geometry can be depicted as, respectively, a network of interconnected galleries (Figure 1 - left) and shafts and large volumes (extraction pits) connected by limited section short tunnels (Figure 1 - right). High level reservoir is, in each case, a large shallow water area at ground level (Figure 1).

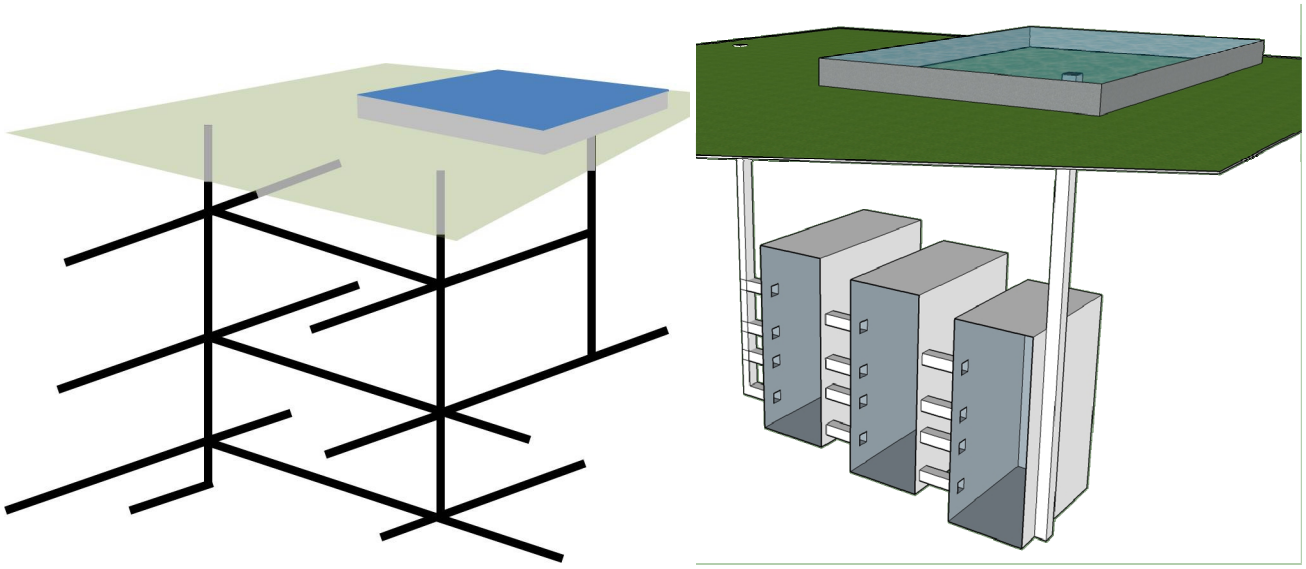

Figure 1. Typical geometry of a coal mine (left) and an underground slate quarry (right) in Wallonia

A mine is usually made of at least two vertical shafts with a circular cross section. Main galleries, with limited slopes and a half circle cross section, start from the shafts at varied elevations and link them to build an interconnected network. Several secondary exploitation galleries are connected to the main galleries.

Typical diameter of a shaft is 4 m, typical depth of a mine is 500 m. Typical diameter of a main gallery is 5 m, with length of several hundreds of meters. These elements were built to last and represent most of the expected available volume to store water. Indeed, besides, length and section of the secondary galleries are smaller (around 100 m and 1.2 m²) and they were not built to last more than the excavation period. They were then rapidly collapsing and should now look like soil areas with large porosity.

The order of magnitude of the available volume is 40,000 m³. With a mean chute of 250 m, this provides an energy storage capacity of 27 MWh.

Such a description of a Walloon mine is very simplified but it highlights the main characteristics of the system.

An underground slate quarry is typically made of several large exploitation pits (15 m wide, 45 m long and 100 m high) separated by 10 m wide pillars. 6 m² short galleries connect the pits at regular elevations. Two rectangular vertical shafts (aeration and extraction) are located on each side of the pits system and connect it to the ground surface. With a global volume of 400,000 m³ and a mean chute of 50 m, such a system enables to store 55 MWh of energy.

4 HYDRAULIC NUMERICAL MODELS

4.1 Objectives and method

In each case depicted in the previous section, the detailed prediction of the water mass movements is a key element of a feasibility analysis. Indeed, they may affect the turbomachines operation (head variation, discharge limitation) as well as the solicitations of the reservoirs sides. On the other hand, such prediction is challenging because of the complex geometry, the continuous discharge variations and the possible exchanges with the surrounding soil or the interaction with entrapped air.

To achieve an accurate prediction of the flow movements in the reservoirs in each configuration, dedicated numerical models have been developed. They are ranging from a lumped model for underground quarries (large interconnected volumes) to a 2D model for shallow water high level reservoir and a 1D model for galleries network (mines).

4.2 2D model

For large shallow water reservoirs, hydraulic modeling is performed by solving the classical depth integrated mass and momentum conservation equations (2D shallow water equations). The reservoir has a free surface at atmospheric pressure. The finite volume WOLF2D model is used with an explicit time integration scheme. Details about the model can be found in Erpicum et al. (2009; 2010a; 2010b).

4.3 1D model

To model the conduit network of a mine, a model solving the mass and momentum conservation equations integrated over the flow cross section is solved. In order to be able to deal with both free surface and pressurized flows and the associated transitions, a mathematical shock-capturing method generalizing the Preissmann slot concept is applied (Kerger et al., 2011). The numerical scheme is the same as the one used to solve the 2D model.

The above depicted approach does not consider air-water interactions. In a next step, the model will evolve to a set of equations dealing with an air-water mixture (drift flux model), similarly to existing models developed by the authors for other applications (Kerger et al., 2012).

4.4 Lumped model

The modeling of large volumes connected by limited section short galleries (underground slate quarry) required the development of a new model. Indeed, despite the system is fully 3D and cannot be simplified considering preferential flow directions, there is no need for a fine spatial discretization in order to model the time evolution of the water levels in the pits, in particular, over very long periods.

The principles of the lumped model are sketched in Figure 2. The knowledge of the pit water depth/volume/sides surface relation and a simple mass conservation equation are enough to predict the time evolution of the surface level and of the area of interaction between the water in the pit and the surrounding ground water. For the short galleries with a limited cross section connecting the pits, the momentum conservation equation can be simplified to a Bernoulli equation written from side to side of the gallery completed by inertia terms.

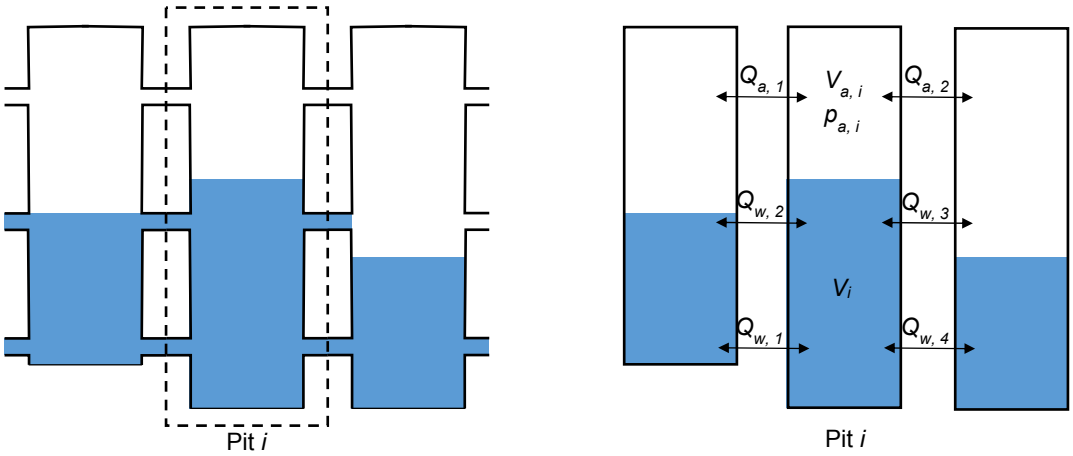

Figure 2. Sketch of the lumped hydraulic model developed for large underground interconnected cavities

For each pit, the water mass conservation equation is

$$\frac{dV}{dt} - \sum_{i=1}^{n_{in}} Q_{w,i} + \sum_{i=1}^{n_{out}} Q_{w,i} - \mu V = 0 \quad [1]$$

with V as the water volume in the pit, t as the time, n_{in} as the number of galleries discharging water into the pits, n_{out} as the number of galleries taking water discharge from the pit, Q_w as the water discharge in the galleries and μ as a Karush-Kuhn-Tucker multiplier (Qi & Jiang, 1997) enabling the equation to consider constraints on the fluid volume in the pit (higher or equal to 0).

Similarly, a mass conservation equation can be written for the air in the pit:

$$\frac{dm_a}{dt} - \sum_{i=1}^{n_{in}} \rho_{a,i} Q_{a,i} + \sum_{i=1}^{n_{out}} \rho_{a,i} Q_{a,i} - \mu m_a = 0 \quad [2]$$

with m_a as the air mass, ρ_a as the air density and Q_a as the air discharge. As the air is a compressible fluid, its pressure is computed from the air mass and the air volume V_a=V_{pit}-V using a state relation

$$\rho_a = \frac{m_a}{V_a} ; \frac{p_a}{\rho_a^{\gamma}} = C \quad [3]$$

where C is a constant equal to 78,500 (air density is 1.2 kg/m³ at a pressure of 1013.25 Pa) and γ is equal to 1.4 in adiabatic conditions.

In each gallery, a transient Bernoulli can be written for both the entrapped air and the water flow

$$\frac{dQ}{dt} + \frac{gS}{L}\left[\frac{Q|Q|}{2gS^2}\left(\frac{fL}{D} + k\right) - \Delta H\right] = 0 \quad [4]$$

with L as the gallery length, g as the gravitation acceleration, S as the gallery cross section, f as the friction coefficient, D as the gallery equivalent diameter, k as the local head loss coefficient (inlet and outlet) and ΔH as the head difference from side to side of the gallery, with the head, H calculated as

$$H = \frac{p}{\rho g} + Z \quad [5]$$

where p is the pressure in the fluid at the gallery extremity, ρ is the fluid (air or water) density and Z is the elevation of the gallery extremity. The friction coefficient is computed using the Barr-Bathurst formula (Machiels et al., 2011).

The model is solved using a first order implicit time integration scheme in an object oriented programming environment (Archambeau et al., 2016).

5 APPLICATION TO AN UNDERGROUND SLATE QUARRY

5.1 Geometry

The lumped model described in section 4.3 has been applied to the case of the Martelange slate quarry. This underground quarry, located in the South part of Wallonia, has been close since 1995. It counts for 9

exploitation pits connected by an unknown number of small galleries. A 170 m deep extraction shaft goes down to the bottom of the deeper pit while an aeration shaft and gallery connect the top of the pits to the ground surface. Despite this quarry has not been abandoned for a long time, a lot of uncertainties exist on its exact geometry. Assumptions have thus been done, and is sketched in Figure 3. The total pits volume is evaluated to be 550,000 m³.

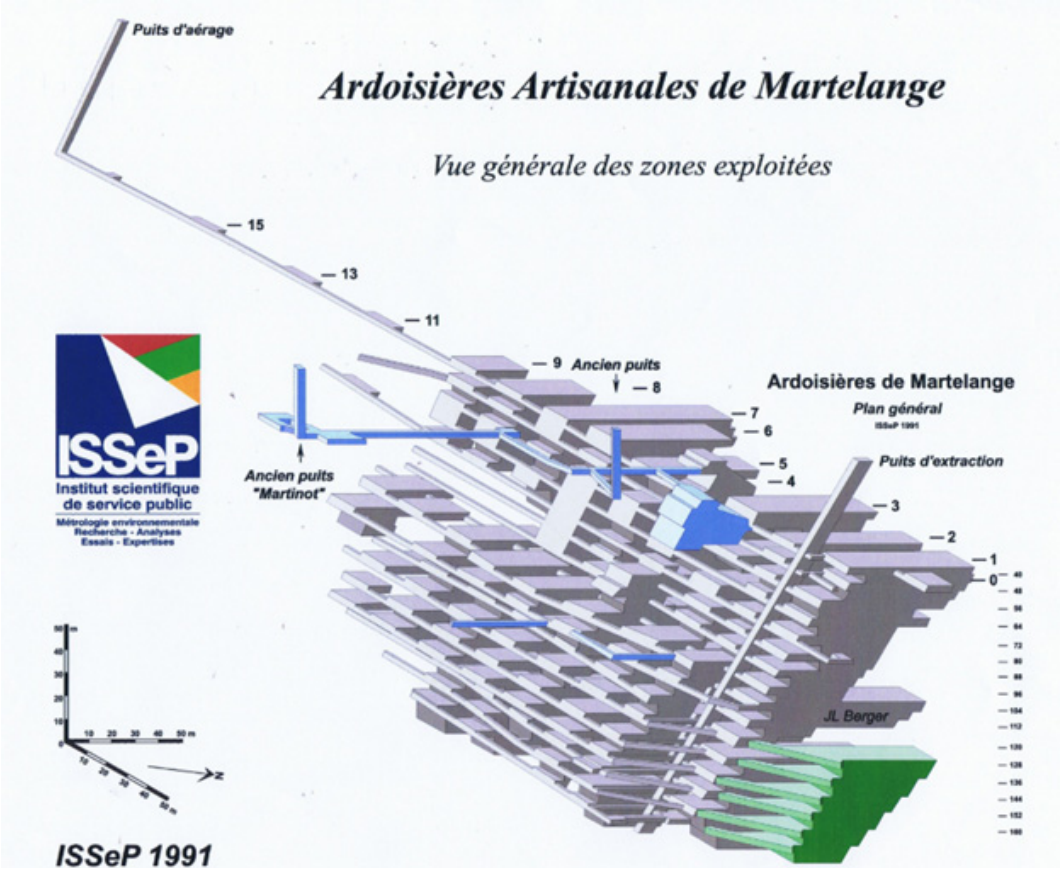

Figure 3. Sketch of the Martelange quarry as considered for the application of the lumped hydraulic model.

In order to perform the computation, the quarry geometry, and in particular the 9 pits geometry, has been simplified as follows: the ground level is 0 m; the maximum depth is -150 m (bottom level of the deepest pit); the top level of each pit is -40 m; the pits bottoms are located along a 5° slope (slope of the slate layer). In addition, the pits horizontal area is constant and equal to 15x45 m². The resulting pits bottom elevation and heights are detailed in table 1.

Connecting galleries are 10 m long (pillars width) and have a 2x2.5 m² cross-section. The aeration shaft is 40 m deep and has a 1.5x1.5 m² cross-section. It is linked to the top of pit 9. Water is injected / removed through the main shaft, connected to the bottom of pit 1.

Table 1. Pits geometric characteristics

Geometric parameters	Pit								
	1	2	3	4	5	6	7	8	9
Bottom level (m)	-150	-145	-140	-135	-130	-125	-120	-115	-110
Height (m)	110	105	100	95	90	85	80	75	70

5.2 Characteristics of the UPSH plant

To create an UPSH, a high level reservoir is needed. Given the quarry location, it seems possible to increase the chute by 100 m if building the second reservoir 500 m North-West of the quarry, on the top of a ground elevation. A 100,000 m² reservoir 4 m deep will create the 400,000 m³ volume necessary to use most of the underground quarry volume. In this configuration, the estimated energy storage capacity would be around 200 MWh per cycle.

5.3 Results and discussion

Simulation of the water levels in the system has been performed, considering a typical 14-days operation scenario defined from current electricity prices variation in Belgium, with complete filling/emptying of the reservoirs over a 24 h period in a maximum of 5 consecutive hours. Such an operation scenario is shown in figure 4c.

The main unknown in this application is the number of the connecting galleries between the pits. 2 configurations have been tested:

- Configuration A with 2 galleries in each pillar (one on the bottom of the lowest pit and the other one 60 m higher) and
- Configuration B with a gallery every 10 m in elevation in each pillar (the number of gallery in each pillar decreases then from pit 1 to pit 9).

Another unknown is the effect of the air volume in the pits. If the aeration shaft enables to completely vent each pit at its top, the air pressure will be almost constant at atmospheric pressure and the amount of air in a pit will vary depending on the water volume. This situation has been considered for configurations A and B. On another hand, if the aeration shaft vents the pits at a level lower than their top, a part of the pits volume might be confined (no possibility for air to escape the pit) and the entrapped air might affect significantly the water movements, with an air pressure different than atmospheric pressure. This has been tested in configuration C, similar to configuration A but with a full computation of the airflow (no assumption of an atmospheric pressure in the pits).

Figure 4 shows the results of the computation for configurations A and B over 3 days of operation, starting from empty pits. The computation time was 90 s for 14 days of operation.

During the turbining phase (pits filling), the water level increases gradually in each pit with an inertia effect leading to temporary overfilling the pits close to the main shaft. The closer the pits from the main shaft, the higher the inertia effects. In case of pumping, the opposite occurs. This induces variation in water level from side to side of a pillar, and thus the solicitation of these structural elements.

The number of connecting galleries directly affects the amplitude of the inertia effects, and thus the maximum water level difference from side to side of a pillar (Table 2). With a high number of connecting galleries (configuration B), the solicitations on the pillars decrease significantly.

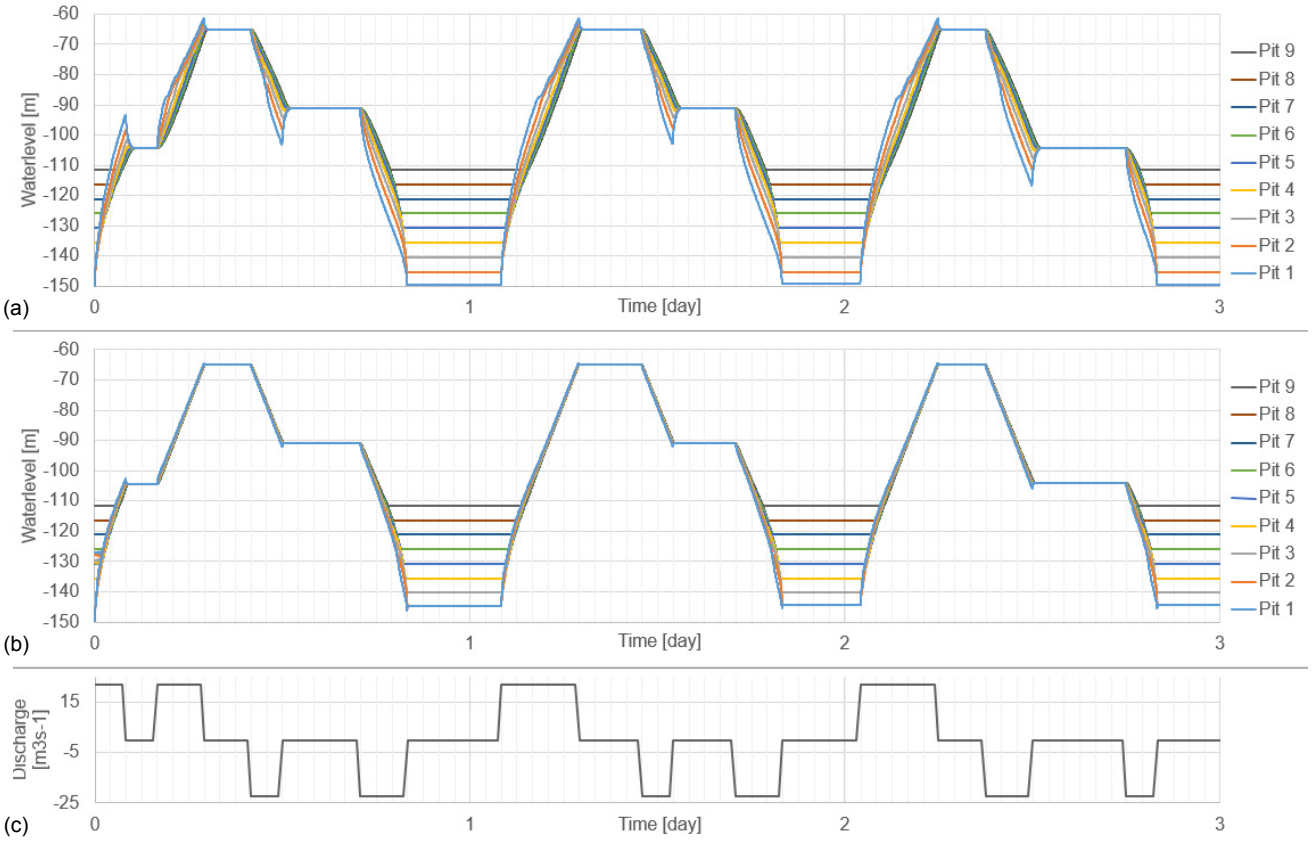

Figure 4. Effect of the number of connecting galleries - Water elevation in the pits over time for configurations A (a) and B (b) and discharge scenario (c)

Table 2. Maximum free surface elevation difference between adjacent pillars for configurations A and B

Nb of connecting galleries	ΔZ_{max} between pillars (m)							
	1-2	2-3	3-4	4-5	5-6	6-7	7-8	8-9
2	5.4	4.8	4.0	3.0	2.0	1.2	0.5	0.1
10	2.9	1.8	1.3	1.0	0.8	0.7	0.4	0.1

Figure 5 shows the results of the computation for configurations A and C over 3 days of operation, starting from empty pits. The computation of air phase was much more time consuming as 3 h were required to model 14 days of operation.

With entrapped air (above level -90 m in each pits – configuration C), the water volume repartition between the pits is much more different than with pits at atmospheric pressure (configuration A). Indeed, entrapped air volumes in each pit limit the water elevation. This directly influences the solicitations the pillars (table 3).

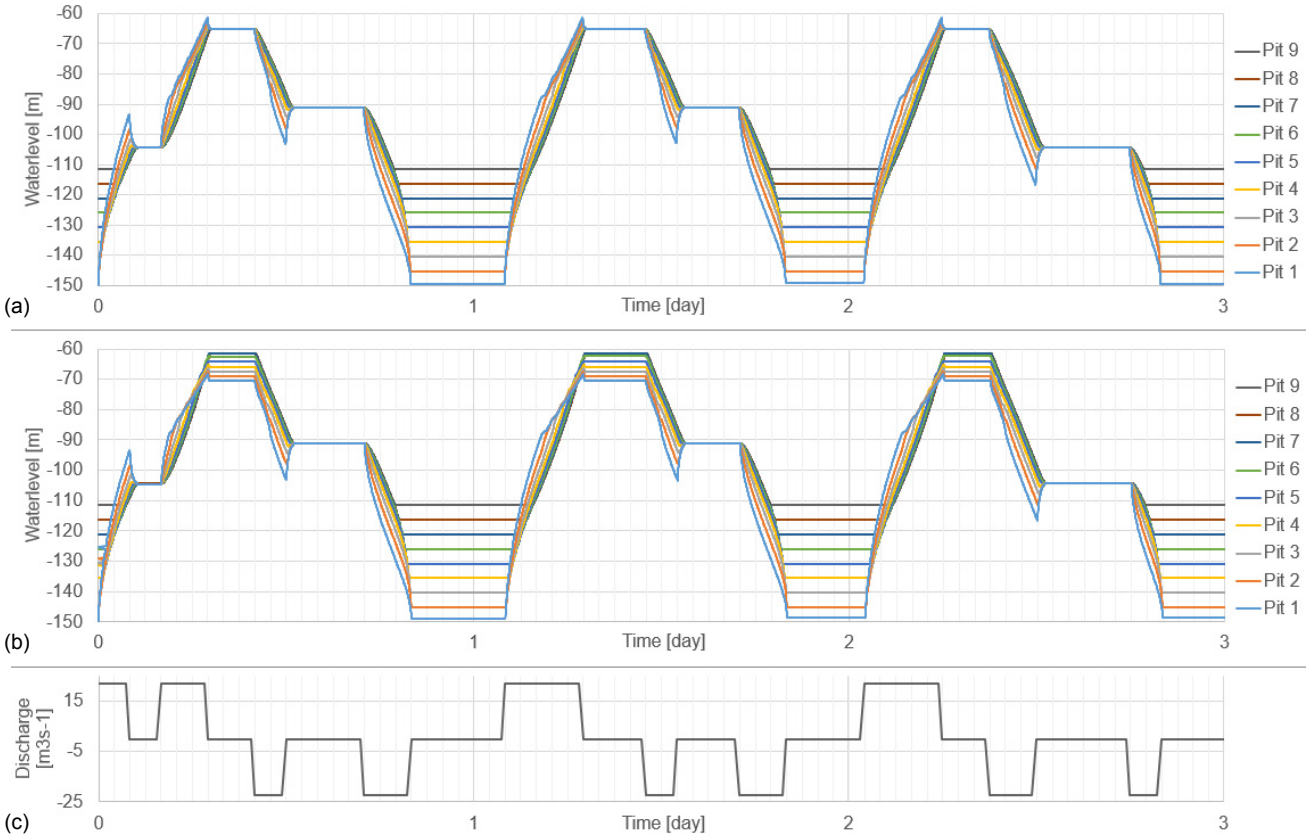

Figure 5. Effect of entrapped air - Water elevation in the pits over time for configurations A (a) and C (b) and discharge scenario (c)

Table 3. Maximum free surface elevation difference between adjacent pillars for configurations A and C

Air in pits	ΔZ_{max} between pillars (m)							
	1-2	2-3	3-4	4-5	5-6	6-7	7-8	8-9
Atmospheric pressure	5.4	4.8	4.0	3.0	2.0	1.2	0.5	0.1
Entrapped	4.8	4.1	3.3	2.5	1.7	1.0	0.2	0.2

6 CONCLUSIONS AND PERSPECTIVES

UPHS is an attractive concept to get new energy storage capacities while rehabilitating abandoned industrial sites. It remains, however, very challenging on several points of view, in particular when the characteristics of the existing underground cavities are not well documented.

In this context, this paper depicts that numerical models are able to help in analyzing the water mass movements in the reservoirs. Considering the simplified configuration of an existing abandoned slate underground quarry in Wallonia, identified as a possible site to build an UPSH, the application of the models

show how sensitive the results can be to the geometry of the underground volume as well as the possible interaction between water flows and the air in the cavities.

Besides, the hydraulic computations presented in the paper are only a small step towards a feasibility study of such an UPSH using existing underground reservoirs. Among other topics, the interaction with ground water or the resistance of the reservoir sides to cyclic pressure variations are key phenomena to be analyzed. The development of tools able to provide objective answers to these problems is part of the Smartwater project in the framework of which the study presented in this paper has been conducted.

ACKNOWLEDGEMENTS

This research was founded by the Public Service of Wallonia – Department of Energy and Sustainable Building in the framework of the ENERGINSERE call.

REFERENCES

Allen, R.D., Doherty, T.J. & Kannberg, L.D. (1984). *Underground Pumped Hydroelectric Storage*, Pacific Northwest Lab., Richland, WA., USA, 78 pp.

Alvarado Montero, R., Niemann, A. & Wortberg, T. (2015). Underground Pumped-Storage Hydroelectricity using Existing Coal Mining Infrastructure. *Proceedings of the 36th IAHR World Congress*, The Hague, Netherland.

Archambeau, P., Bodeux, S., Cerfontaine, B., Charlier, R., Dassargues, A., Erpicum, E., Frippiat, C., Goderniaux, P., Pirotton, M., Poulain, A., Orban, P., Pujades, E., Ronchi, N., Stassen, F. & Willems, T. (2016). *Smartwater project - Sites de stockage hydraulique – Inventaire, Analyses géomécanique, hydrogéologique et hydraulique*. Convention n° 1450316. Report D1.2. (In French).

Erpicum, S., Meile, T., Dewals, B.J., Pirotton, M. & Schleiss, A.J. (2009). 2D Numerical Flow Modeling In a Macro-Rough Channel. *International Journal for Numerical Methods in Fluids*, 61(11), 1227-1246.

Erpicum, S., Dewals, B., Archambeau, P. & Pirotton, M. (2010a). Dam-Break Flow Computation Based On an Efficient Flux-Vector Splitting. *Journal of Computational and Applied Mathematics*, 234, 2143–2151.

Erpicum, S., Dewals, B., Archambeau, P. & Pirotton, M. (2010b). Detailed Inundation Modelling using High Resolution Dems. *Engineering Applications of Computational Fluid Mechanics*, 4(2), 196–208.

Evans, A., Strezov, V. & Evans, T.J. (2012). Assessment of Utility Energy Storage Options for Increased Renewable Energy Penetration. *Renewable and Sustainable Energy Reviews*, 16 (6), 4141-4147.

GRID Innovation online. (2017). SMARTWATER - PHES Energy Storage Using End of Life Quarries and Mines – Belgium Wallonia specific use-cases, http://www.gridinnovation-on-line.eu/Articles/Library/SMARTWATER---PHES-Energy-Storage-Using-End-Of-Life-Quarries-And-Mines---Belgium-Wallonia-Specific-Use-Cases.kl (accessed February 6, 2017)

Kerger, F., Archambeau, P., Erpicum, S., Dewals, B. & Pirotton, M. (2011). An exact Riemann Solver and Godunov Scheme for Simulating Highly Transient Mixed Flows. *Journal of Computational & Applied Mathematics*, 235, 2030-2040.

Kerger, F., Archambeau, P., Dewals, B., Erpicum, S. & Pirotton, M. (2012). Three-phase Bi-layer Model for Simulating Mixed Flows, *Journal of Hydraulic Research*, 50(3), 312-319.

Machiels, O., Erpicum, S., Archambeau, P., Dewals & Pirotton, M. (2011). Theoretical and Numerical Analysis of the Influence of the Bottom Friction Formulation in Free Surface Flow Modelling. *Water SA*, 37(2), 221-228.

Pesesse, C. (2013). *Faisabilité De Projets De Pompage-Turbinage Basés Sur L'anciennes Galeries Minières*. *Master Thesis*, University of Liège: Liège, (in French).

Pujades, E., Willems, T., Bodeux, S., Orban, P. & Dassargues, A. (2106). Underground Pumped Storage Hydroelectricity Using Abandoned Works (Deep Mines Or Open Pits) And The Impact On Groundwater Flow. *Hydrogeology Journal*, 24(6), 1531-1546.

Qi, L. & Jiang, H. (1997). Semi-smooth Karush-Kuhn-Tucker Equations and Convergence Analysis of Newton and Quasi-Newton Methods for Solving these Equations, *Mathematics of Operations Research*, 22, 301-325

Steffen, B. (2012). Prospects for Pumped-Hydro Storage in Germany. *Energy Policy*, 45, 420-429.

Proceedings of the 37th IAHR World Congress
August 13 – 18, 2017, Kuala Lumpur, Malaysia

A NOVEL FREE JET TURBINE FOR USING KINETIC ENERGY IN THE FIELD OF NANO-HYDROPOWER

JENS METZGER[(1)], JÖRG WIELAND[(2)], JENS BENDER[(3)], JÜRGEN JENSEN[(4)] & MD ABID HASAN[(5)]

[(12,3,4,)] Research Institute for Water and Environment (fwu), Dept. of Hydraulic and Coastal Engineering (University of Siegen)
jens.metzger@uni-siegen.de
[(5)] Department of Mechatronics (University of Siegen)

ABSTRACT

The potential of Germany´s hydropower is nearly exhausted and almost all locations where large hydropower plants can be applied have been developed. Due to missing application areas for large hydropower plants, potentials of less than 250 W (nano-hydropower) are becoming more and more important. In order to use the potentials efficiently, technical implementations are hardly available thus far. The free jet turbine developed for the location of Netphen converts kinetic energy in the range of nano-hydropower to electricity. Due to its simple construction, it is possible to produce this turbine cost-effective and to apply it at various different application areas. On the grounds that a complex and loss-intensive transmission is not needed, the maintenance efforts of the turbine can be reduced to a minimum. After investigating the free jet turbine regarding its performance and efficiency in the laboratory, currently it is being used at a power station for supplying loads (e.g. LED-lights) with electricity. A maximum mechanical efficiency of 25 % and an electrical power of 10 W by using a discharge of 3.0 l/s were achieved. Due to the simple turbine components, a larger dimension to generate an electrical power of several hundred watts is conceivable.

Keywords: Sustainable Energy; Turbine; Kinetic Energy; Small Drop Heights; Blade Optimization.

1 INTRODUCTION

The use of hydropower in Germany is focused on larger drop heights and greater discharges, e.g. hydropower plants at dams and barrages on rivers. Renewable energy has been produced profitably for more than 100 years by applying large and medium hydropower plants.

The classification of small, medium and large hydropower and its corresponding power limits is distinguishing worldwide as well as in Germany. According to the Federation of German hydropower plants (BDW), the field of small and medium hydropower contains power plants with an installed capacity of more than 5 MW. In Germany, only 21 out of about 7200 totally installed hydropower plants exceed this criteria. Around 6900 hydropower plants are operating in the performance range of less than 1 MW and are defined as micro hydropower plants. Application areas for large-scale hydropower plants are almost completely in use. Therefore, the economically potential of Germany is nearly exhausted. Technical realizations for the use of hydropower potentials of less than 250 W (so called nano-hydropower) are currently not available, but could provide a valuable contribution to the energy revolution if installed in a vast number.

Due to the Water Framework Directive of the European Union (Directive 2000/60/EC), new constructions of transverse structures, in the manner of weirs and dams to create artificial drop heights, are excluded. Considering its baseload capacity hydropower is still regarded as an important part of the energy revolution in Germany. Therefore, using hydropower potentials with low drop heights and small discharges becomes increasingly important. Particularly, appropriate solutions for the efficient energetic use of potentials in the drop height range below 2 m are currently in the focus of further development.

2 PROJECT IN NETPHEN

The municipality of the city of Netphen (Germany) plans to create an educational energy station to endorse different forms of renewable energy. In the course of this purpose, the municipality would like to build an energy station with the use of wind power, hydropower and photovoltaic. The aim of this energy station is to inform interested people especially student groups, about the generation of electricity by renewable energy techniques and the comparison of different energy technologies. The Research Institute for Water and Environment (fwu) was commissioned to design a nano-hydropower plant for this specific project. In the interest of producing the energy supply of a teaching station, there is no economic consideration for the hydropower plant.

In Netphen, there is a penstock which supplies a wading pool with a small discharge of the stream “Sohlbach”. The inflowing water is fed back to the Sohlbach with a height difference of about $\Delta h = 1.50$ m. It was decided to use the existing drop height energetically by installing the designed nano-hydropower plant.

2.1 Maximum physical performance

According to the first measurements, the upper limit of the usable discharge at the outlet of the wading pool is Q = 3.0 l/s. Increasing the resulting power by raising the discharge of the penstock is not possible, on the grounds that the Sohlbach would dry out, which would disagree with the environmental objectives of the EU Water Framework Directive. A power increase is therefore only possible by increasing the drop height or by using a larger diameter of the turbine. The amount of discharge is led back to the Sohlbach from the wading pool via a DN 125 outlet pipe and a drop height of Δh = 1.50 m. For determining the resulting maximum gross power, P_{max} can be calculated as:

$$P_{\max} = \frac{1}{2} \cdot \rho \cdot Q \cdot \left(\sqrt{2 \cdot g \cdot \Delta h}\right)^2 \qquad [1]$$

$$P_{\max} = \rho \cdot g \cdot Q \cdot \Delta h = 1000 \frac{kg}{m^3} \cdot 9.81 \frac{m}{s^2} \cdot 0.003 \frac{m^3}{s} \cdot 1.50 m = 44 W$$

with: ρ = density of the water [kg/m³]
g = acceleration of gravity [m/s²]
Q = discharge [m³/s]
Δh = drop height [m]

3 PRODUCTION OF THE HYDROPOWER PLANT

For the utilization of such very small hydropower potentials, no technical solutions are available so far. Due to the absent of suitable solutions, a free jet turbine with a vertical axis was developed at fwu. For an efficient usage of the discharge, the emerging water from the outlet has to be precisely concentrated by a distribution box with a slit nozzle. An overview of the planned power plant setup at the outlet of the wading pool is shown in Figure 1.

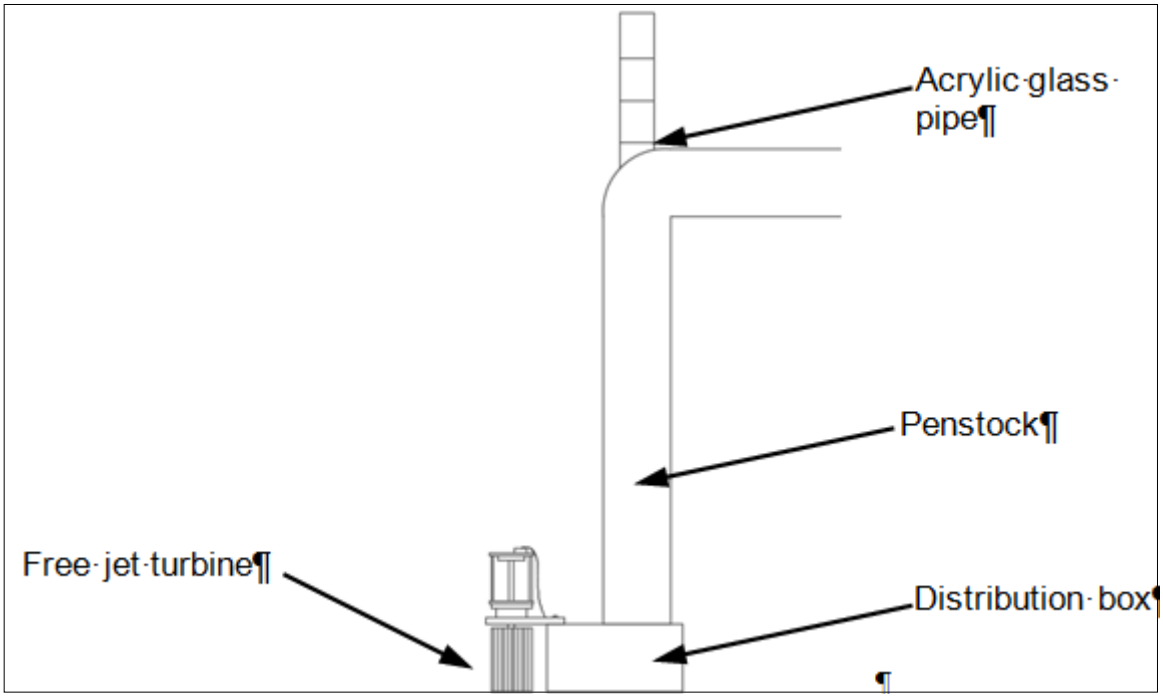

Figure 1. Planned power plant setup in Netphen.

The penstock of the setup in Figure 1 is connected to the outlet of the wading pool and supplies the distribution box with water. The free jet turbine is installed in front of the slit nozzle. Concentrated by the slit nozzle, the discharge emerges from the distribution box and transfers its jet power to the rotor of the turbine. By using an acrylic glass pipe, the drop height can be easily measured.

3.1 Construction of the distribution box

Due to seasonal fluctuations, the discharge varies. To enable a correspondingly high and continuous water pressure on the turbine, the construction of a special distribution box with adjustable slit nozzle was necessary. Figure 2 shows the section view of the distribution box.

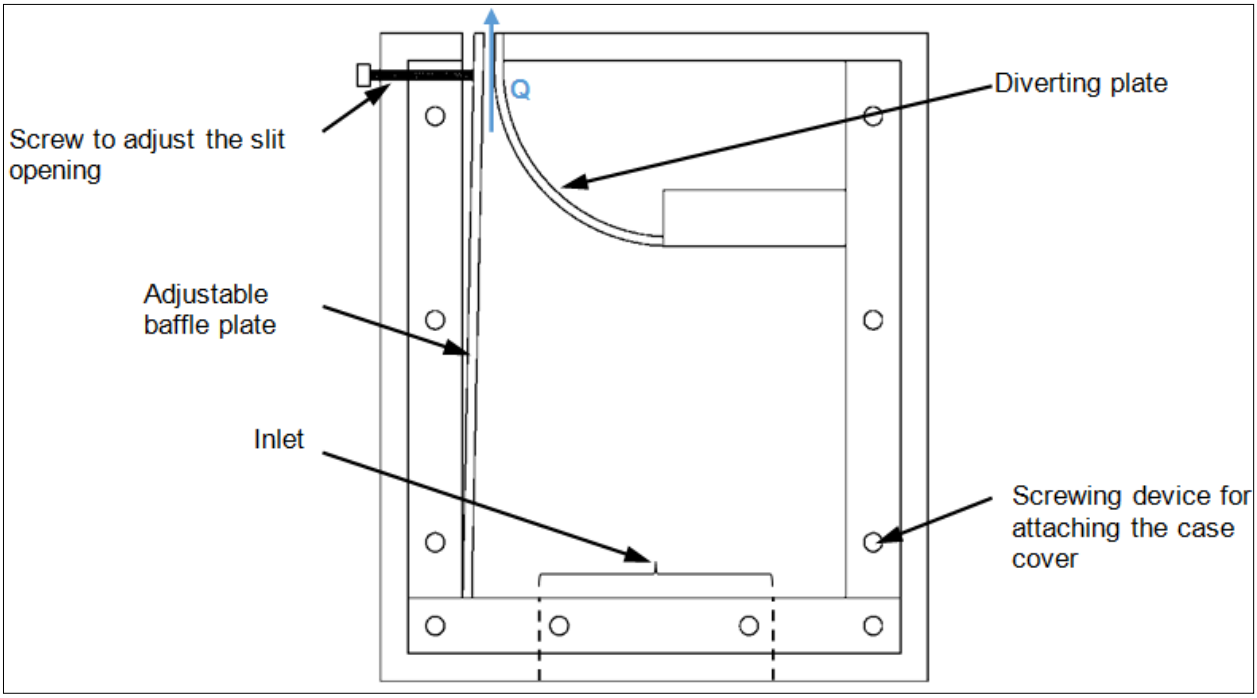

Figure 2. Distribution box for feeding the free jet turbine (section view).

The distribution box is connected to the outlet tube of the wading pool at its inlet. On the opposite side, a nozzle in the form of a slit is installed, which distributes the emerging discharge uniformly over the entire slit height. The slit height corresponds to the rotor height of the turbine to admit the turbine uniformly. For ensuring a continuous water pressure on the rotor, the slit width can be adjusted by a screw mechanism which allows an adaption to variable flow rates. The required slit width of the distribution box for the given drop height of Δh = 1.50 m and a discharge of Q = 3 l/s can be calculated as follows:

$$Q = \mu \cdot v \cdot A \qquad [2]$$

$$0.003 \frac{m^3}{s} = \mu \cdot A \cdot \sqrt{2 \cdot g \cdot h}$$

$$0.003 \frac{m^3}{s} = 0.93 \cdot 0.13 \cdot b \cdot \sqrt{2 \cdot 9.81 \cdot 1.50}$$

$$\Rightarrow b = 0.0046 \approx 5mm$$

with:
μ = outflow coefficient [-]
b = slit width [m]
A = cross section of the slit [m²]
g = acceleration of gravity [m/s²]
Q = discharge [m³/s]
Δh = drop height [m]

According to Aigner and Bollrich (2015), the outflow coefficient, μ can be set to approximately 0.93, because of the very good rounding conditions at the upper-water opening edges.

The used slit opening width of b = 5 mm for installing in Netphen was calculated for a discharge of Q = 3 l/s.

3.2 Construction of the rotor

The water flows into the rotor from the distribution box with a high velocity. To use the total water jet height, a turbine with the rotor height of h = 13 cm, a rotor diameter of D = 8.5 cm and 16 rotor blades was constructed. It was designed vertically, because the generator has to be sealed in order to protect the electric parts at high flow time. The rotor was drawn using the CAD software CADVance and extruded with the BLENDER software (Figure 3, left). The resulting 3D body could be printed by the program of a 3D printer (Figure 3, right). Acrylonitrile-butadiene-styrene copolymer (ABS) was used as a printing filament, which is particularly suitable for this application because of its weather resistance.

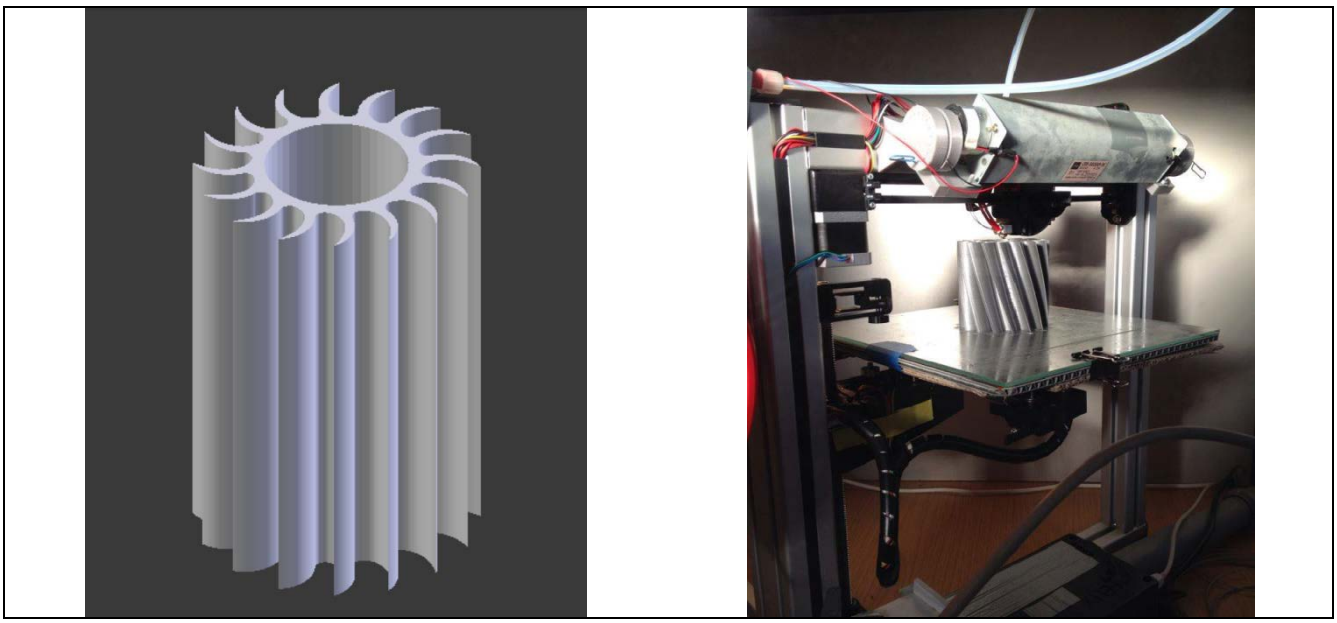

Figure 3. Extruded design drawing of a straight rotor (left), 3D printing of a turbine rotor with 60° twisted blades (right).

At the beginning of the tests, a rotor with straight blades was constructed (Figure 3, left). The blades of the rotor are inclined in the direction of the impinging water jet which enables an increase of water absorption capacity of the turbine. For comparison, a further rotor variant with blades twisted by 60° around the turbine axis was also produced. The advantage of twisting the blades is that the rotor surface A, which is impinged by the slit nozzle, increases. Hence, the resulting force, F increases due to larger rotor area (Pascal's law):

$$F = p \cdot A \qquad [3]$$

Due to this design, a higher resulting power and efficiency is expected from the free jet turbine by using the rotor with twisted blades.

3.3 Construction of the free jet turbine

To increase the rotor stability, two discs were mounted at the ends of the rotor and connected with the rotor blades. In the center of these discs (rotor axis), thread passes were installed, whereby the rotor can be screwed onto the turbine axis. Two nuts were used to fasten the rotor, with which the screw connection was locked. The turbine setup is shown in Figure 4.

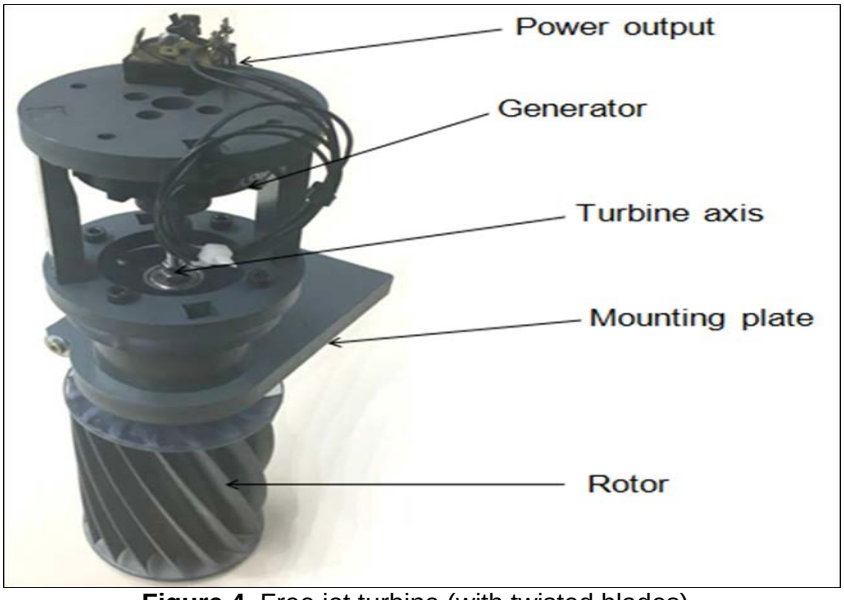

Figure 4. Free jet turbine (with twisted blades).

The adjustable installation of the free jet turbine onto the distribution box (Figure 5) allows the free jet turbine to be aligned in its optimum angle to the slit nozzle. For an energetically optimized usage of the water jet emerging from the slit nozzle, the free jet turbine is aligned in such a way that the jet impinges on the blade center of the rotor. Due to the rotor blade curvature, the greatest transmission forces are generated by impinging the blades in their center, whereby the rotational speed of the turbine reaches its maximum without generating any power.

Figure 5. Mounting of the free jet turbine on the distribution box.

3.4 Generator

The rotor of the free jet turbine was connected to the generator via the ball-beard turbine axis. A brushless three-phase gimbal motor was used as a generator, which provides a maximum voltage of 12 V and a maximum power of P = 60 W. This type of motor is generally used for model constructions and promises a simple use for the free jet turbine by its vertical axle implementation without any additional structural needs. The advantage of using this brushless technology is that the generator operates free from wear to reduce the required maintenance work on the turbine. Additionally, this type of motor can even convert small power into electric current.

The current generated by the generator is transferred to the bridge rectifier, which converts the existing alternating current into direct current. A 12 V voltage regulator, which limits the voltage for the used loads was connected downstream of the rectifier. The loads (e.g., LED lighting), connected to the voltage regulator were operating at a maximum DC voltage of 12V. This results in a total electrical loss in the range of 0.25 to 0.8 W versus the mechanical power of the turbine.

In order to protect against flooding, spray water and rain, the rotor axis was extended and the generator was additionally enclosed.

4 INVESTIGATIONS IN THE LABORATORY OF FWU

Before using the free jet turbine under natural conditions, investigations were carried out regarding their efficiency and performance behavior at different boundary conditions in the laboratory of fwu. One aspect of the test was to find out if the calculated slit opening width is optimal for the given hydraulic conditions ($Q = 3$ l/s; $\Delta h = 1.50$ m).

4.1 Experimental setup

For conducting the investigations on the free jet turbine, the experimental setup was constructed corresponding to the natural conditions in Netphen based on the planned setup in Figure 1. The setup consists of a 1.30 m long penstock, the distribution box and the turbine. As a structurally facilitating device, a pipe connection was integrated into the distribution box on the upper side. In this connection, the downpipe was inserted and sealed. At the other end of the tube a 90 ° tube bend connects the experimental setup with the water supply of the laboratory. A vertical 40 cm long acrylic glass tube is located in this buckling, whereby the drop height acting on the turbine can be adjusted by changing the pressure level and measured on a scale of the acrylic glass tube.

4.2 Implementation of the laboratory experiments

The aim was to examine the free jet turbine regarding to its performance and efficiency at different drop heights along with its working rotational speed range for both rotor variants (straight and twisted blades). At the beginning, the turbine was adjusted to its optimum inflow position and the slit width on the distribution box was corrected. Since the maximum usable discharge of the experimental setup is limited to about $Q = 2$ l/s, the natural conditions in Netphen could not be fully reached and all investigations were carried out by a

discharge of about Q = 2 l/s. The discharge was regulated by a magnetic inductive flow meter (MID) connected to the downpipe in conjunction with a DN50 motor valve.

The load on the turbine is influenced by an interposed 100 Ω sliding resistor. Increasing the electrical resistance resulted in a decrease in rotational speed of the turbine. The intermediate resistance was increased in 10 Ω steps, so that the rotational speed was reduced continuously. After each increase in resistance, the electrical voltage, U and amperage, I on the resistor were measured over a period of five seconds after homogenization of the resulting power. The averaged values were formed for every measuring point and were used to calculate the electrical power, P_{el} of the turbine by:

$$P_{el} = U \cdot I \qquad [4]$$

To calculate the mechanical turbine power, the efficiency of the generator and the rectifier must be considered:

$$P_{mech} = \frac{U \cdot I}{\eta_{Gen} \cdot \eta_{GR}} \qquad [5]$$

with: η_{Gen} = efficiency of the generator = 0.90 [-]
η_{GR} = efficiency of the ACDC converter = 0.97 [-]

The gross power occurring at the experimental setup was calculated according to equation [2]. In this case, the given drop height and discharge (read at the MID) were used for further calculation. The electrical and mechanical efficiency can be calculated by using the electrical (mechanical) power, $P_{el(mech)}$ and the gross power, P_{gross} at the respective point in time of the measurement:

$$\eta_{el(\text{mech})} = \frac{P_{el(mech)}}{P_{gross}} \qquad [6]$$

In order to compare the measured performances and efficiencies, the ratio of the wheel peripheral speed to the inflow velocity u/v was computed. The wheel peripheral speed is depending on the rotational speed as well as the radius of the rotor and can be calculated by:

$$u / v = \frac{N \cdot 2\pi \cdot R}{\sqrt{2 \cdot g \cdot \Delta h} \cdot 60} \qquad [7]$$

with: u = wheel peripheral speed [m/s]
N = rotational speed of the turbine [1/min]
R = radius of the turbine [m]
Δh = drop height [m]
g = acceleration of gravity [m/s²]
v = inflow velocity [m/s]

The used radius refers to the distance between the turbine axis and the middle of a blade. Typically, the highest values for converters of kinetic energy are obtained at u/v = 0.5. It will be expected, that the highest performance and efficiency values will be generated in this range as well.

The investigations of the performance and efficiency behavior were based on three different drop heights. In this case, the rotational speed was varied by operating the sliding resistance at drop heights of 1.40, 1.50 as well as 1.60 m. In this way, a statement about the development of the power and the efficiency could be made by increasing the kinetic energy acting on the turbine.

5 EVALUATION OF THE RESULTS

The calculated power and efficiency values of both rotor types were initially compared and determined as to which rotor variant has the highest efficiency and which will be used for the power station in Netphen. The electrical performance and efficiency values of the two rotor types measured in the laboratory tests were compared with the entire rotational speed range of the turbine. Due to the braking influence of the sliding resistance, the same rotational speed range was achieved for each test run. The measured electrical power and efficiency values of the two rotor types for a drop height of Δh = 1.60 m are shown in Figure 6.

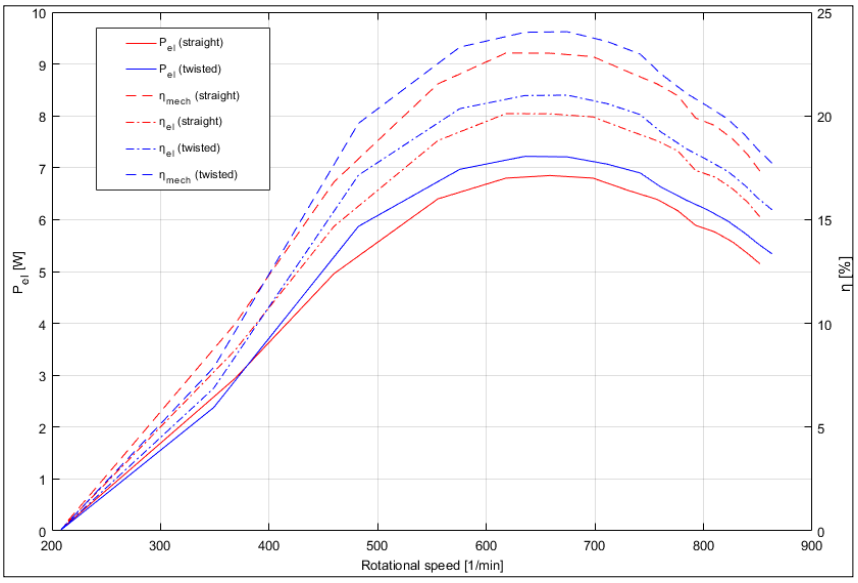

Figure 6. Electrical performance and efficiency as well as mechanical efficiency values of both rotor variants at Δh = 1.60 m and Q = 2.2 l/s.

It can be seen in Figure 6 that the rotor variant with 60° twisted blades can achieve consistently higher electrical performance and efficiency values compared to the rotor with straight blades. Therefore, at relatively high and low rotational speeds, there is only a minor difference in performance and efficiency, because an excessively different jet impact force is lost in this case. In the range of the ratio of the wheel peripheral speed to the inflow velocity of u/v = 0.50, the highest power and efficiency values could be achieved for both rotor variants. While a maximum output of 7.2 W could be reached for the twisted rotor variant, only 6.95 W could be produced with the straight rotor variant. The maximum efficiency of the twisted rotor variant was also higher (η_{el} = 21%). By dividing the electrical efficiency with the efficiencies of the rectifier and the generator, the mechanical maximum efficiency of the rotor variant with 60° twisted blades could be calculated as η_{mech} = 24.1%.

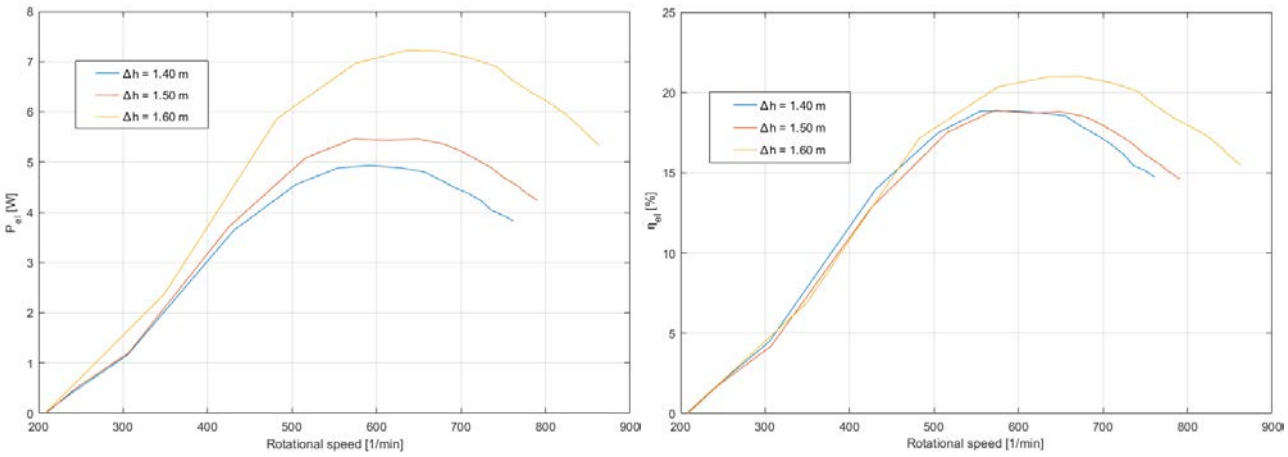

Figure 7. Electrical power (left) und electrical efficiency (right) of the rotor variant with twisted blades during all investigated drop heights.

An increase in the drop height, as shown in Figure 7 (left), causes an increase in the resulting electrical power. In the range of low rotational speeds, only a small power difference is present. The reason for the small difference is that the wheel peripheral speed is almost equal to the inflow velocity and hardly any power is extracted from the system. Only the performance curve of a drop height of Δh = 1.60 m allows a higher performance even at high rotational speeds because a higher discharge (Q = 2.2 l/s) was used to enable a larger drop height. However, the determined performance curves are equal to each other over their investigated rotational speed range and result their maximum at a ratio of the wheel peripheral speed to the inflow velocity of u/v = 0.5.

In Figure 7 (right), the efficiency curves for all investigated drop heights are shown in comparison. It is visible that the gradients for the drop heights of Δh = 1.40 and 1.50 m are almost equal, because the same discharge was used. To reach a drop height of Δh = 1.60 m, the discharge had to be increased to Q = 2.2 l/s.

This increase the available potential energy in the downpipe. Due to the higher efficiency, it can also be concluded that the optimum operating discharge of the free jet turbine exceeds the previously tested Q = 2.0 l/s. However, it was not possible to carry out further measurements at higher discharges because the experimental setup did not permit any higher flow rates. It is, however, to be assumed that the free jet turbine operates more efficiently at a flow rate of Q = 3 l/s in Netphen.

6 INSTALLATION OF THE FREE JET TURBINE

After completion of the laboratory tests, the free jet turbine was installed at the outlet of the wading pool in Netphen. The structure of the hydroelectric power plant is shown in Figure 8.

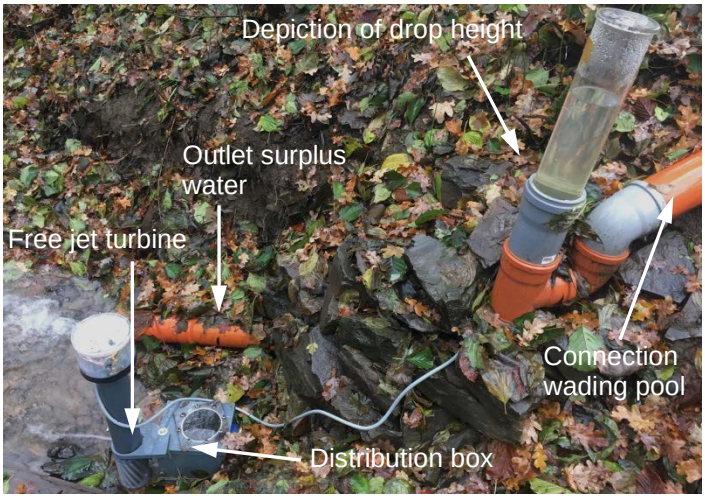

Figure 8. Installed hydroelectric power plant at the outlet of the wading pool in Netphen.

From the bottom of the wading pool, an outlet pipe leads down to the Sohlbach with a drop height of Δh = 1.50 m. There is a pipe junction at half of the pipe height, on which a vertical acrylic glass cylinder is attached. In this cylinder, the water rises to the upper limit of the drop height which makes the measuring of the drop height acting on the free jet turbine easier. On the other side of the pipe junction, a pipe connection is connected and opens into the distributing box of the turbine. This connection was realized with a 90 ° pipe piece located in the subsoil. An additional surplus discharge pipe was also connected to the pipe junction, which returns the occurring surplus water back to the Sohlbach. The free jet turbine is continuously charged with Q = 3 l/s. In the case of a higher quantity of discharge leaving the bottom of the wading pool, the residual water is directed directly into the Sohlbach via this surplus discharge pipe.

The axis of the free jet turbine was extended by 30 cm, which allows a greater protection of the generator against over flooding. In addition, the generator is protected against rainwater by using an acrylic glass cover.

At the installation site in Netphen, electrical performances in the range of P_{el} = 10 W and electrical efficiencies in the range of η_{el} = 25 % were measured after completing the hydroelectric power plant.
The electricity generated by the free jet turbine supplies an energy station for teaching purposes, where a USB charging station for mobile phones, LED lighting for switching on and a transistor radio were integrated.

7 SUMMARY AND OUTLOOK

In the field of large-scale hydropower, the potential locations in Germany are almost completely developed. Due to the nearly exhausted potential of hydropower, technical solutions for the utilization of the smaller potentials have obtained an increased importance. In the field of nano-hydropower (less than 250 W), technical solutions for using such small potentials are hardly available, but could contribute a large part to the energy revolution.

The free jet turbine is such a technical realization, with which nano-hydropower potentials can be used energetically efficiently. Due to its simple construction, the production costs can be kept to a minimum and necessary maintenance work is almost excluded. The simple attachment to the distribution box, a separation of the turbine for maintenance purposes is also unproblematic. Due to the very simple turbine components, a development of larger model variants can be realized without any problem.

The first laboratory tests of this small-scale kinetic energy converter yielded an electrical maximum efficiency of η_{el} = 21 % and a maximum power of P_{el} = 7.2 W at a discharge of Q = 2.2 l/s. By producing a large-scale realization of this free jet turbine and the usage of greater discharges, resulting performances in the range of several 100 W are conceivable.

After completion of the project, a larger free jet turbine with a resulting electrical output of more than 100 W is to be produced and will be investigated regarding its performance as a part of a student thesis, and

will be investigated regarding its performance and efficiency in the laboratory. The goal of this study work is the use of the turbine under real conditions and supplying loads with higher current requirement.

ACKNOWLEDGEMENTS

We would like to thank the Südwestfalen-Agentur, which has enabled the development of the free jet turbine. We also thank the Energieagentur.NRW and the local community of Netphen for their support during the project.

REFERENCES

Aigner, D. & Bollrich, G. (2015). *Handbuch der Hydraulik* – für Wasserbau und Wasserwirtschaft 1. Auflage. Beuth Verlag Berlin. 1-514, (In German).

Water Framework Directive of the European Union (Directive 2000/60/EC*): Directive 2000/60/EC of the European Parliament and of the Council Establishing a Framework for the Community Action in the Field of Water Policy*. 12/2000.

Proceedings of the 37th IAHR World Congress
August 13 – 18, 2017, Kuala Lumpur, Malaysia

BUOYANT ENERGY – MULTIFUNCTIONAL OFFSHORE ENERGY STORAGE AND GRID BALANCING SYSTEM FOR FUTURE REQUIREMENTS

BERND STEIDL[(1)], ROBERT KLAR[(2)] & MARKUS AUFLEGER[(3)]

[(1,2,3)] Department of Civil Engineering Sciences, Unit of Hydraulic Engineering, University of Innsbruck, Austria
bernd.steidl@uibk.ac.at

ABSTRACT

Using one of the basic concepts of Buoyant Energy (BE), a new energy storage solution for future requirements was experimentally tested in the Laboratory of the University of Innsbruck. The main aim is to determine and to validate the principle functionality and applicability for energy storage. For the tests, a deep-water basin without disturbing influences like turbulences was chosen. This calm surrounding is important to focus on the main research parameters. As shown in the results, the body proportion (height/length or height/diameter) has a major influence on the floating stability. The physical model test was able to prove the concept of BE.

Keywords: Renewable; energy storage; decentralized; pumped storage hydropower (PSH); physical model.

1 INTRODUCTION

The importance of electricity, as a good major of our society rapidly increases. More and more of our daily use devices need electrical power. At the same time, with regard to the strong growth of this need, many countries, especially in Europe, try to force power production out of renewables. As a consequence, electricity production is a parameter of the supply given by the renewables and no longer a parameter of demand (Nacht, 2014). Therefore, the peak of production and the peak of supply differ more and more from each other. Furthermore, grid stability is negatively affected by the intermittent power input of volatile renewables (wind and solar energy). According to these facts, efficient energy storage solutions that allow a controlled power charging and feeding have to be developed.

Buoyant Energy (BE), a new decentralized storage approach, could define one possible part of the solution. The very simple concept of BE is based on the well-established technology of pumped storage hydropower solutions (PSH) as described in Chapter 2. Energy could be stored through converting electrical to potential energy and reversed by raising and lowering, e.g. a massive body, also called Buoyant Body. A scientific research project of the Hydraulic Engineering Unit of the University of Innsbruck in cooperation with the Vienna University of Technology (Institute for Energy Systems and Thermodynamics) and the University of Edinburgh (Institute for Energy Systems) is actually in progress. As described by Klar et al. (2016) the aim of this research program is to clarify the potential of BE for future requirements of energy storage solutions. Although the advantages of BE in comparison to other concepts (simpler, equal or even more efficient, more durable, etc.) should be highlighted in this research program. But before the potential of BE could be evaluated, some essential tasks like the conceptual design, the floating structure design, the mechanical and electrical engineering, the multifunctional use, etc. (Klar et al., 2016; Neisch et al., 2015) have to be investigated in the form of experimental tests and numerical calculations. The interpretation of the results should allow a scientific funded evaluation of the most suitable concept of BE afterwards.

One advantage of the BE concept is defined by the independence of possible locations where it can be installed. As BE can be placed offshore or nearshore, it is also conceivable to place BE storage solutions onshore (e.g. lakes with sufficient depth near big cities). Due to the freedom of choice and the possibility of multifunctional use of the BE solution, different societal, political, industrial and/or economic interests that every location offer poses a challenge but is also a huge chance for solution in the future. This paper deals with first experimental tests of Type A (Chapter 2, Figure 1) to verify the functionality and to determine the main stability parameters.

2 BUOYANT ENERGY STORAGE CONCEPT

The core idea of Buoyant Energy is well described as "floating pumped storage power plant" (Figure 1 and Figure 2). The major differences are the basic arrangement and the location of the reservoirs at such plants. While conventional pumped storage hydropower systems consist of an upper and a lower reservoir, Buoyant Energy uses a smaller reservoir (the inside space of a floating structure), located within a larger reservoir (the sea or a lake). Water can be transferred from one reservoir to the other by means of pumps and turbines or a pump turbine. The BE storage concepts can be classified into two major types: Type A and Type B.

2.1 Type A

The required head (the vertical difference between an upper water level and a lower water level) is created by the weight and the shape of a floating structure. The inside space of the structure serves as lower reservoir. A pump turbine is installed in the lower part of the structure. For storing energy, water will be pumped out from the inside space to the sea. The structure is moving up (Figure 1). While producing energy, water will flow into the structure, driving the turbine. The structure moves down. Typically the head remains approximately constant all the time.

Buoyant Energy Type A is a robust system with a floating platform built from a suitable construction material, typically concrete. Floating concrete structures are economical to build and maintain. The existing offshore industry (oil and gas) as well as coastal construction industry (e.g. submerged tunnel construction) has a lot of experience with large floating concrete structures. While weight is a disadvantage for many floating structures, it is essential in this case for maximising the energy storage capacity.

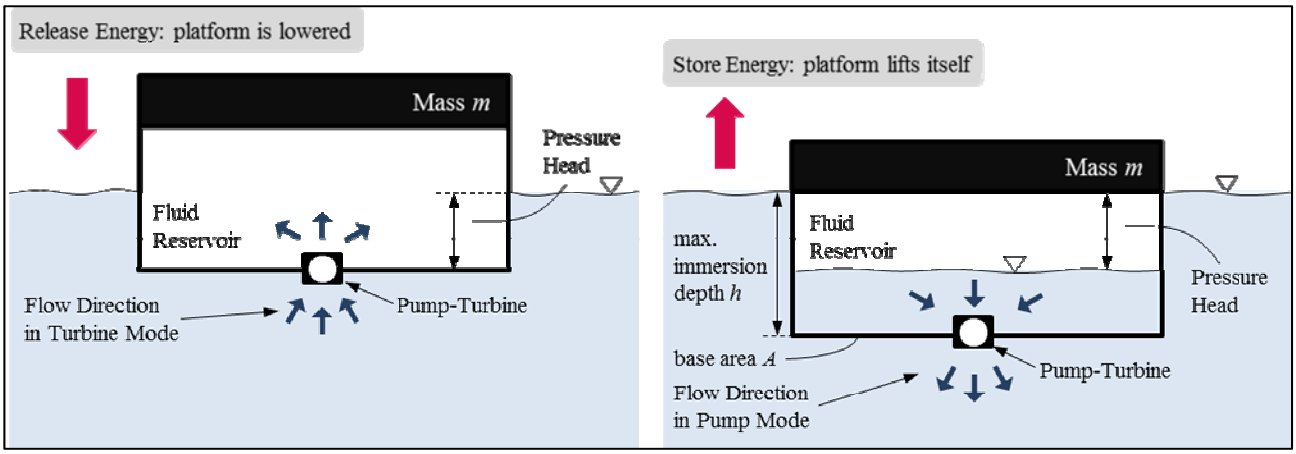

Figure 1. Buoyant energy storage solution Type A.

The structure weight and the geometry ensure an appropriate initial immersion depth. The water level inside is significantly lower compared to the outer sea level. The water level difference with its available head respectively is a decisive parameter for the pump/turbine system. The inside volume and the head difference are critical parameters in determining the energy storage capacity.

Structure weight as well as geometry contributes to better wave damping properties. Research is required to ensure floating stability and station keeping during operation under different metocean conditions. A physical model test was performed to validate the floating stability on a small prototype (Chapter 3) at the laboratory of University of Innsbruck.

2.2 Type B (the ´Light´ version)

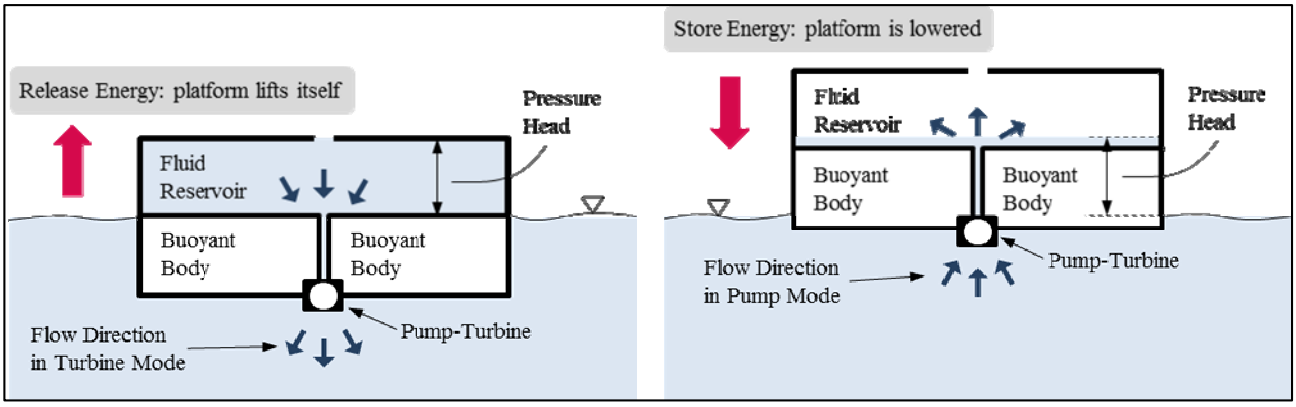

Figure 2. Buoyant energy storage solution Type B (light version).

Type B is characterized by a lower water level of the surrounding water compared to the inner water level of the energy storage device (Figure 2). In contrast to the original concept, the direction of energy conversion is reversed. For this purpose, the hydraulic energy storage plant is equipped with buoyant bodies within the structure that are underneath the water reservoir, which typically raise the bottom of the water reservoir above the water level of the outer reservoir. In turbine operation mode, the floating structure rises, working against

gravity. The potential energy is converted into electric energy and is released. In pump operation mode, the floating structure moves down, thereby converting the electric energy into potential energy and storing it. This variation needs less construction material, which could result in significantly reduced investment costs compared to the Type A Buoyant Energy solution. Anyhow, most probably there will be more stability problems due to the relatively high elevation of the center of mass in bad weather and sea conditions.

3 PHYSICAL MODEL EXPERIMENTS

The development of BE structures is in a very early stage. Until now, much elementary research work about fundamental issues like different storage possibilities, their capacity and effectiveness, possible designs of BE structures depending on varying requirements, etc. have been done. Nevertheless, it is necessary to answer the question of whether the concept of the Type A solution is working. Therefore, a series of different experiments have been made with a physically built model (Figure 3).

The experimental tests were performed in a deep-water flume under calm water conditions in the laboratory of University of Innsbruck. Due to that, the experiments deal mainly with static conditions without any dynamic influences like waves or streams. This model test configuration allowed concentration on basic floating design parameters. The anchoring of the body and dynamic movement due to external forces like waves and wind were not part of the investigations.

All performed physical model tests aim to validate the principles of BE for the first time. The used model was a non-scaled version of a BE storage solution for actual storage needs. Therefore, different parameters such as installed machinery elements, required storage capacity, influence of static and dynamic forces on the construction (wind and waves), multifunctional use and others would have to be specified first. This will be part of future research.

3.1 Model Setup

The setup of model Type A shown in Figure 3 consists of the following basic elements:

- Floating Body
- Weight
- Pump
- Magnet valve (symbolizes the turbine)
- CPU (controller)
- Water level indicator

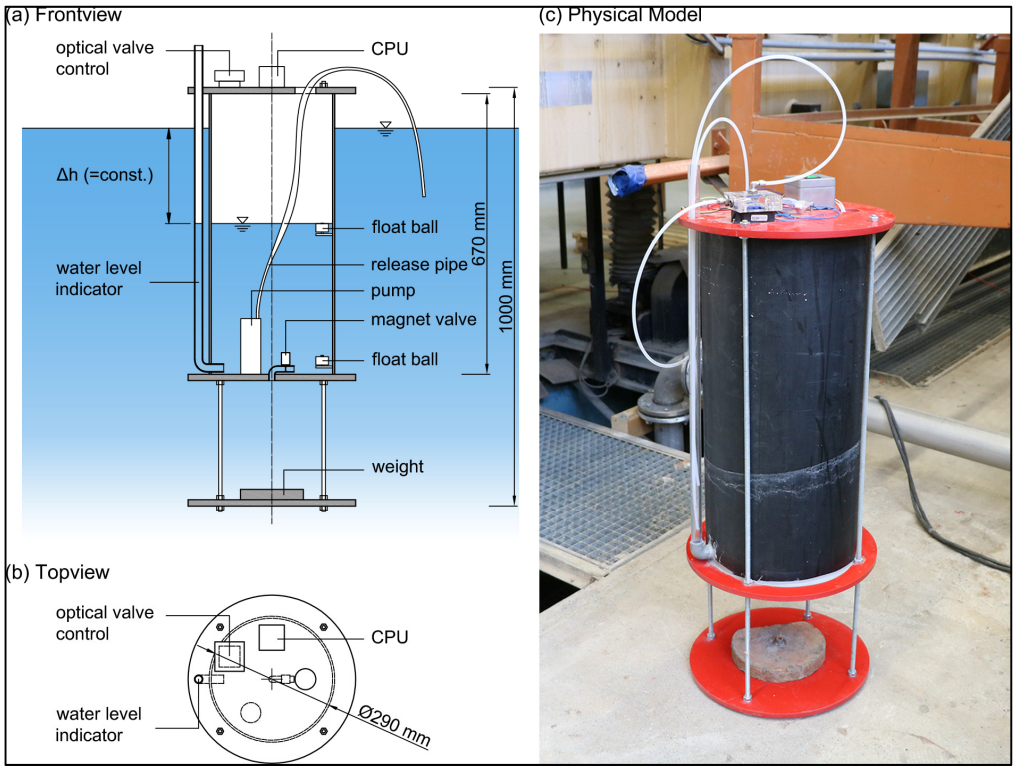

Figure 3. (a) and (b) Type A - model setup. (c) Physical Model.

The inner reservoir diameter was d_{ir} = 0.3 m and the inner height was about h_{ir} = 0.7 m. The maximum water volume in case of a fully discharged storage was about V_{dis} = 0.028 m³ (≈ 30 l). The total model height was about h_{tot} = 1.0 m.

3.2 Experimental procedure

The aim of the experimental tests of Type A is to verify the concept. Although no larger doubts existed, it was also very important to show that the floating stability is given at any stage of energy storage or production. This could become the defining stability issue especially in the case of a fully charged storage when the floating body juts out of the water. In order to avoid tilting of the body, some basics of hydro mechanic knowledge was used.

Swimming stability depends on the location of the center of gravity, S_G of the floating body, the center of buoyance, S_b of the displaced water volume and the metacenter, M to each other. The metacenter is defined as the point of intersection between the line of action of the buoyance force, S_b when the body is leaned and the connection line between the center of gravity and the center of buoyance when the body is in neutral position. As long as the metacenter is arranged above the center of gravity, the floating body is in a stable position. If it is arranged beneath, the floating structure becomes unstable and tilts. Figure 4 shows the basic concept for swimming stability.

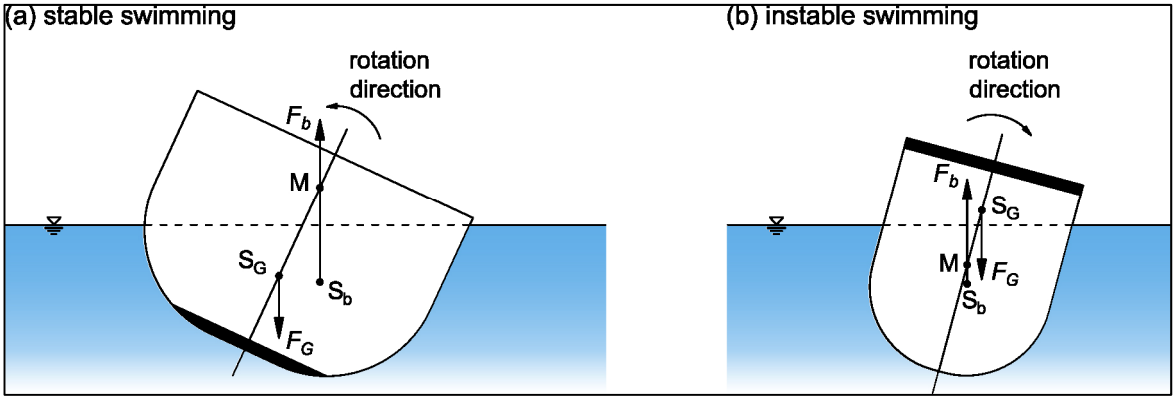

Figure 4. (a) stable and (b) unstable swimming of floating bodies. (adapted from Jirka, 2007).

4 RESULTS

Figure 5 shows diverse time steps during the draining process of the inner reservoir (energy storage). During the test, the body raised (draining water) and lowered (filling with water) itself several times without any problems. Hence, it can be said that the basic concept works well. Furthermore, the risk of tilting was not observed at any time. The floating body was always in a stable position.

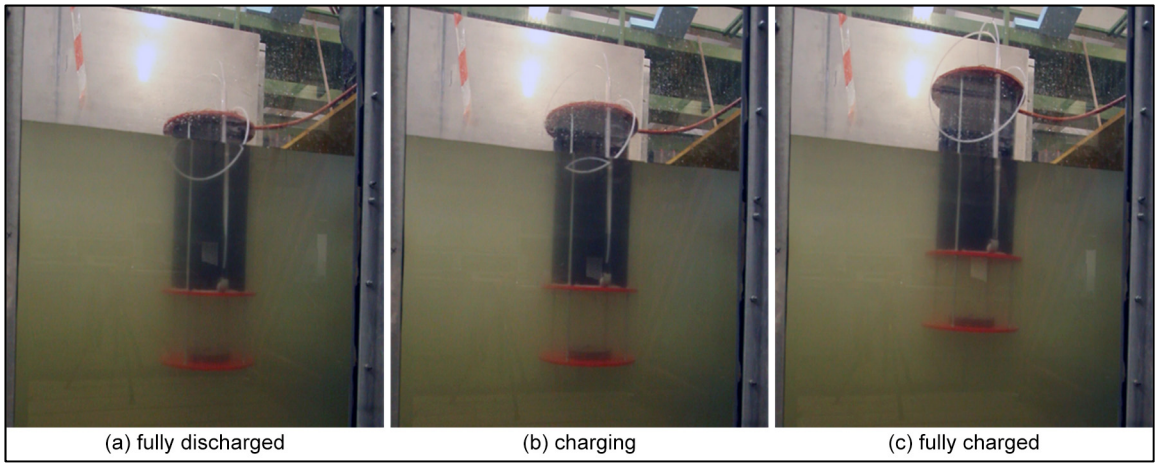

Figure 5. Model Type A – Energy storage by draining the inner reservoir.

One of the reasons for this straight lifting is certainly due to the calm water conditions but even in the case of rough water conditions, tilting should not occur. The model design that even after a significant displacement, the body moved back to its initial position as shown in Figure 6. The presented pictures show selected time steps during the stabilization process after a mechanically indicated displacement.

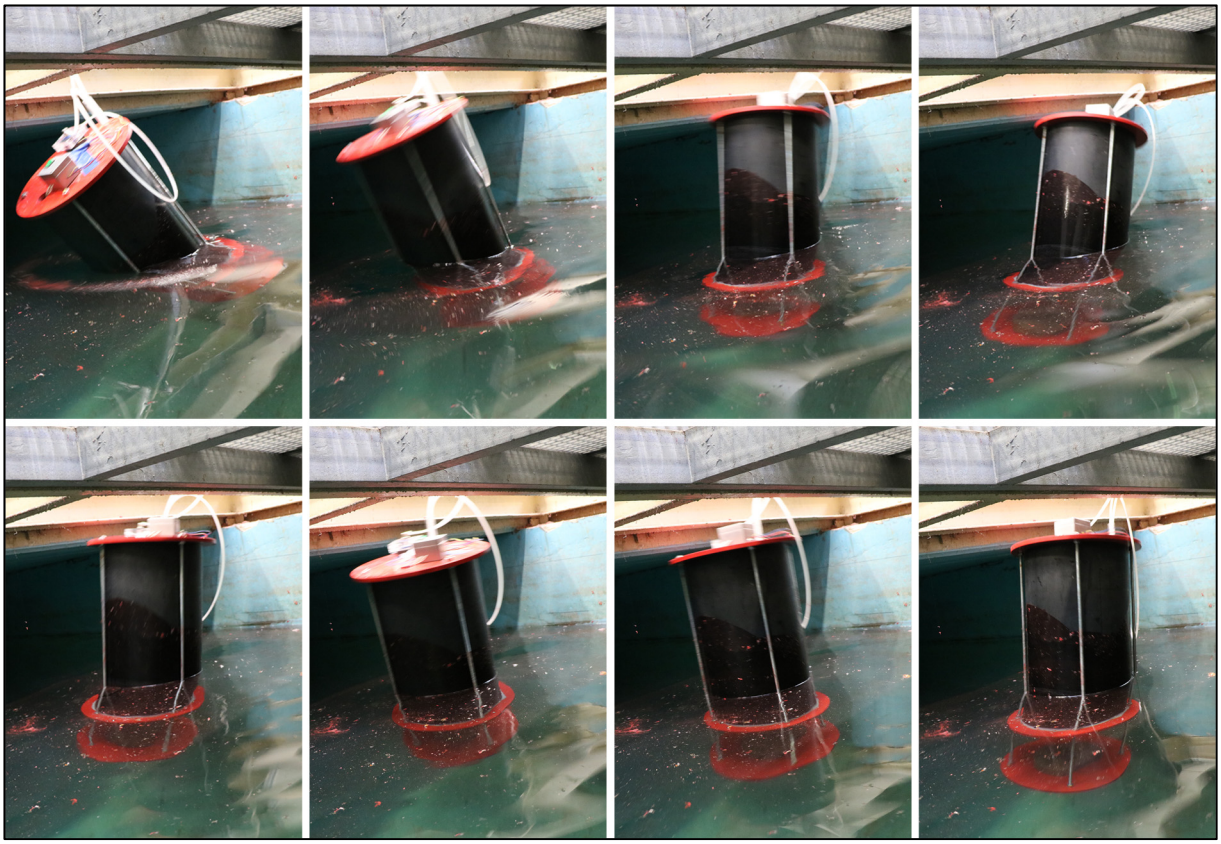

Figure 6. Tilting experiment.

As apparent from Figure 4 (b), long and slim bodies tend to tilt much more easily than broad and shorter bodies. In the case of the experiments, the crucial factor was the weight at the bottom. As shown in Figure 3, it was arranged about 0.3 m beneath the reservoir. Consequently, the center of gravity was always arranged beneath the metacenter even if there were a strong deflection caused by wind, waves, etc. Nevertheless, a single solution of this setup is unrealistic because with regard to multifunctional use in reality, it is probable that most of the weight is arranged at the top or at least much higher than that in the model. A possible solution for this problem is a cluster layout. If the cluster were to be arranged in a matrix, e.g. with quadratic layout, then the ratio of h/l (h…body height, l…length) would be much smaller. This would have a positive effect on the system stability even if the center of gravity of the single solution is above the metacenter. Other advantages could be that the cluster is built up modularly, it can be adapted to change energy storage needs and its service and maintenance might be easier.

5 CONCLUSION AND OUTLOOK

The experiments have shown that the main concept of the Buoyant Energy principle works. Concerning the floating stability, the most important characteristics are the position of the center of gravity and the metacenter to each other. As long as the metacenter is arranged above the center of gravity, the system is stable. Due to the intention of multipurpose use of the upper deck of Type A BE platforms, shallow and wide structures are preferable in comparison to slim bodies. There are important potential synergies of large Buoyant Energy structures (Figure 7) and directly linked technologies (e.g. additional use as service and operation platform for offshore wind farms) or other economic sectors (industry, fishery, leisure, housing). For a reliable economic assessment, these aspects have to be considered.

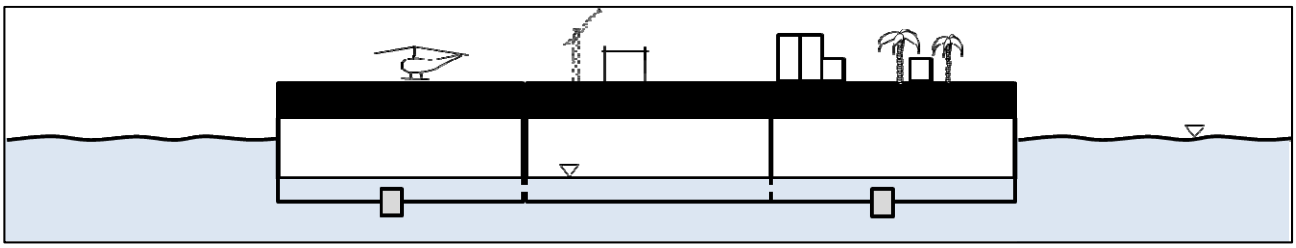

Figure 7. Potential synergies with other directly linked technologies (e.g. wind farms) or other economic sectors.

The next important task is to evaluate application fields and locations with energy storage need and demand of multipurpose floating platforms. Based on the respective situations, the location determines the BE dimension, design, mooring, possible multifunctional use, etc. The exploratory project PrepareBE (Klar et al., 2016), which will end in Nov. 2017 will clarify whether the Buoyant Energy principle is technically feasible and economically viable.

REFERENCES

Jirka, G.H. (2007). *Einführung in die Hydromechanik*. Institute of Hydromechanics (IfH), KIT Scientific Publising, Germany, Karlsruhe, 40.

Klar, R., Aufleger, M., Schneide, G. & Neisch, V. (2016). PrepareBE (Buoyant Energy) – Exploratory Project Prensentation. *OSES 2016 – Offshore Energy and Storage Symposium,* Malta, At Vallettaa, 3.

Nacht, T. & Stigler, H. (2014). Die Erhöhung des Wertes erneuerbarer Einspeisung durch Pumpspeicherkraftwerke. 13*. Symposium Energieinnovation,* Austria, Graz.

Neisch, V., Aufleger, M., Klar, R. & Lumassegger, S. (2015). A Comprehensive Hydraulic Gravity Energy Storage System – Both for Offshore and Onshore Applications. *E-proceedings of the 36th IAHR World Congress* "Deltas of the Future and what happens upstream"*.* 28 June – 3 July, 2015, The Hague, the Netherlands. Madrid: International Association for Hydro-Environment Engineering and Research (IAHR), 1-7.

IMPACTS OF GLACIER RECESSION ON THE HYDROENERGY PRODUCTION, SANTA AND PATIVILCA BASINS (PERU)

MARISA SILVA DAVILA[(1)]

[(1)] Universidad Nacional de Ingeniería, Lima, Perú,
marisi@uni.edu.pe

ABSTRACT

The effect of climate change in Peru is evident in the melting of glaciers, with a significant reduction in snow coverage. Studies show that there is a relationship between deglaciation of existing snow and the availability of water resources. The observed decrease of base flows indicates that it would have passed from the stage of the contribution of high water flow originated by the accelerated melting of snowy mountains due to the rising temperatures. Analysis of flow trends at seasonal level confirms a downward trend of the flow in the dry and transition periods, which are linked to the glacier contribution. The expected magnitude of the flow decrease is herein calculated in relation to the decrease of glacier coverage. The analysis was conducted every four months: in the start of the wet season, the end of the wet season and the dry season. The influence of glacier retreat on the hydrological regime by the destabilizing effect of rising temperatures on glaciers located at altitudes where previously they had permanent snow or glacier coverage for longer periods was also analyzed. Results show that by losing storage capacity in the snowy peaks, there is an increase in the flood peaks and a reduction of the flows in the dry season. Trends considering the historical records and future scenarios on the hydropower production of plants belonging to the national grid located in the basins of the Santa and Pativilca Rivers (Pacific Ocean basin) are analyzed and discussed.

Keywords: Tropical glaciers recession; hydroenergy production.

1 INTRODUCTION

The increase in the average air and ocean temperatures, snow melting of glaciers and poles, and rising sea levels are some of the effects of climate change, as found in the Intergovernmental Panel on Climate Change, IPCC, (2007). For this study, sub-basins located in the upper portion of the Santa and Pativilca river basins have been selected, whose location is shown in Figure 1. Both basins belong to the Pacific Ocean basin and are located in the northern region of Peru. In the Santa basin, the watershed controlled by the Quitaracsa station was chosen, while in the Pativilca basin the basins of the Huayllapa and Pumarinri rivers were chosen, the latter two, when joined together, form the Rapay River. These basins are also shown in Figure 2.

Different studies carried out in the Santa River Basin show the effect of climate change, mainly affecting the important glacier coverage of the basins. This variation would be directly related to the acceleration of snowfall melting due to the increase in temperature attributable to climate change as the following observations appear to suggest:

- An increasing tendency has been found in the maximum and minimum temperatures (Francou and Pouyaud, 2004) and a decrease in glacier coverage has been observed (Francou and Pouyaud, 2004; Pouyaud et al.,2002);
- The higher basins have a deglaciation velocity that is much lower than the lower basins, as found in Pouyaud et al. (2002)
- A high correlation has been found between the global warming process, the increase in temperatures in the high Andean areas of the Santa River basin and the glacier retreat with the consequent impact on the availability of water resources (SENAMHI, 2005; Francou and Pouyaud, 2004);

These observations can be extrapolated to the basin of the Pativilca River, located in Pacific Ocean Basin as Santa basin since it has a similar surface, drainage, and geomorphic characteristics.

The objectives of this paper are as follows:

- To determine the water supply of glaciers;
- To examine the effects of the glacier recession on the water availability in the selected basins;
- To calculate the variation of energy production produced by the change in water availability.

The analysis carried out based on the glacier coverage area meets the requirements for its representativeness. It is not possible to make the calculation according to the volume since there are no glacier deposits thickness and density measurements of the basin and its variation in the accumulation and ablation areas.

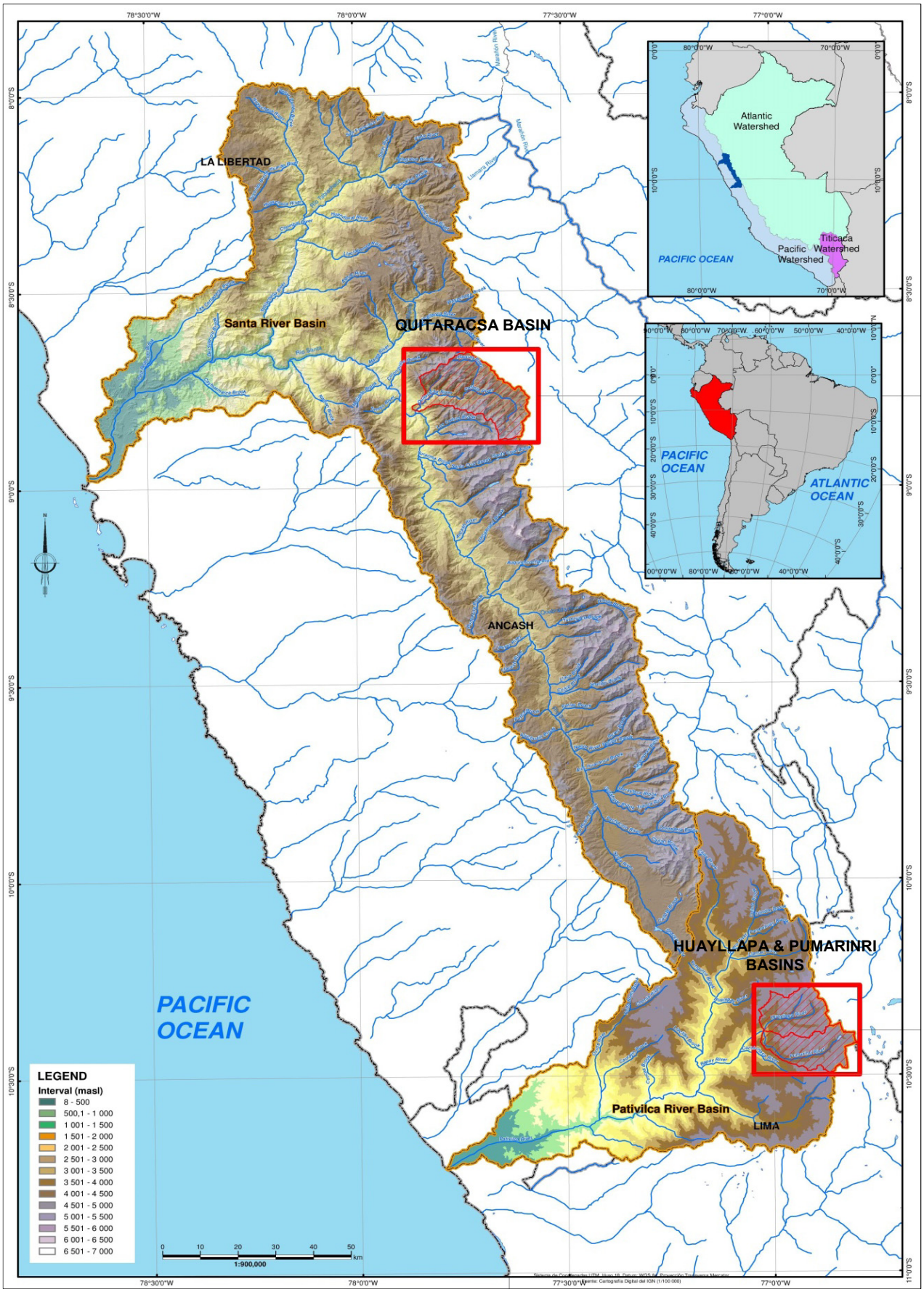

Figure 1. Location of the Santa and Pativilca basins in Peru.

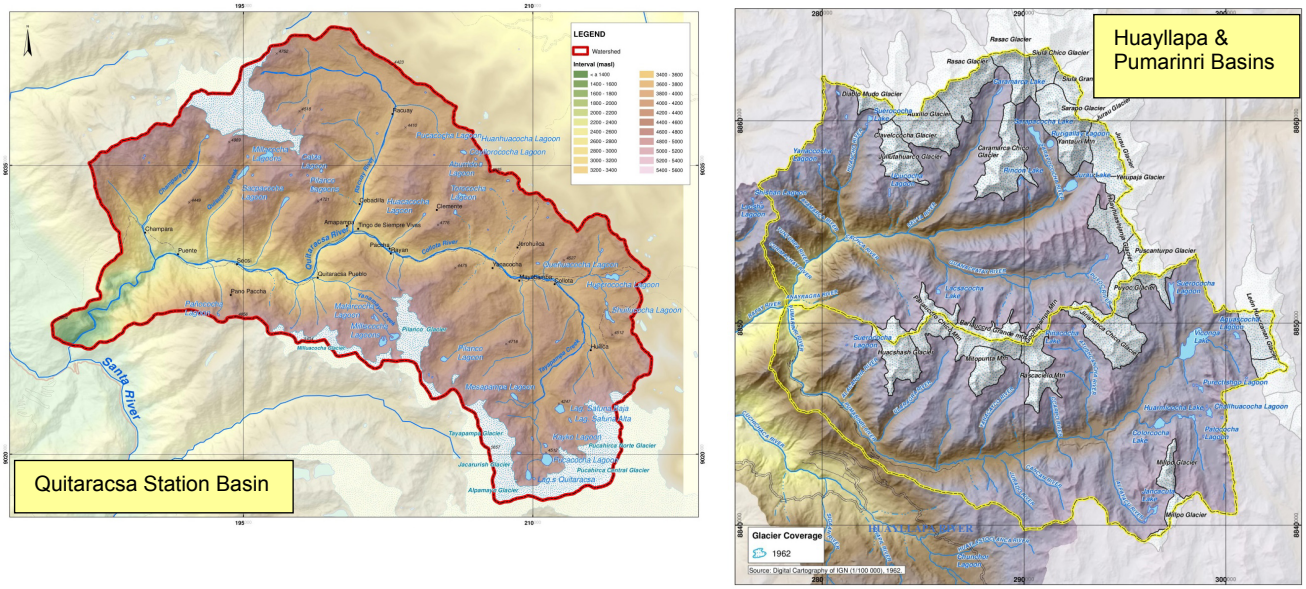

Figure 2. Location of the Quitaracsa, Huayllapa and Pumarinri basins.

2 WATER RESOURCES FROM GLACIERS

2.1 Effect on water availability

The results of the study "Métodos de Observación de Glaciares en los Andes Tropicales, Mediciones de Terreno y Procesamiento de Datos (Methods of observation of Glaciers in the Tropical Andes, Field Measurements, and Data Processing)" by Francou and Pouyard (2004) were used for determining the effects on water availability. The study was based on the observations of 13 basins of the Santa River, between 1953 and 1997, the data are in Table 1.

Table 1. Sheets of run-off vs. percentage of glacier area (Francou and Pouyard, 2004).

		Wet season	Start of Wet season	End of Wet season	Dry Season	
			Sheets of run-off, 1953-1997			
Hydrometric Station	**% Glacier area**	**Sep-Apr mm**	**Sep-Dec mm**	**Jan-Apr mm**	**May-Aug mm**	**Year mm**
Recreta	2	0,266	0,044	0,222	0,037	0,305
Querococha	6	0,703	0,216	0,487	0,114	0,822
Quitarasca	9	0,684	0,233	0,451	0,188	0,876
Pachacoto	12	0,539	0,172	0,367	0,097	0,64
La Balsa	12	0,496	0,14	0,356	0,093	0,592
Olleros	16	0,724	0,267	0,457	0,141	0,869
Colcas	22	0,604	0,216	0,388	0,165	0,772
Los Cedros	22	0,688	0,278	0,41	0,238	0,928
Chancos	33	0,811	0,302	0,509	0,2	1,015
Quillcay	37	0,731	0,271	0,46	0,171	0,905
Llanganuco	40	0,807	0,321	0,486	0,272	1,082
Parón	51	0,86	0,319	0,541	0,333	1,197
Artesoncocha	83	1,56	0,744	0,816	0,329	1,893
Source: "Métodos de Observación de Glaciares en los Andes Tropicales, Mediciones de Terreno y Procesamiento de datos", Francou and Pouyard (2004).					**AVERAGE**	**0,915**

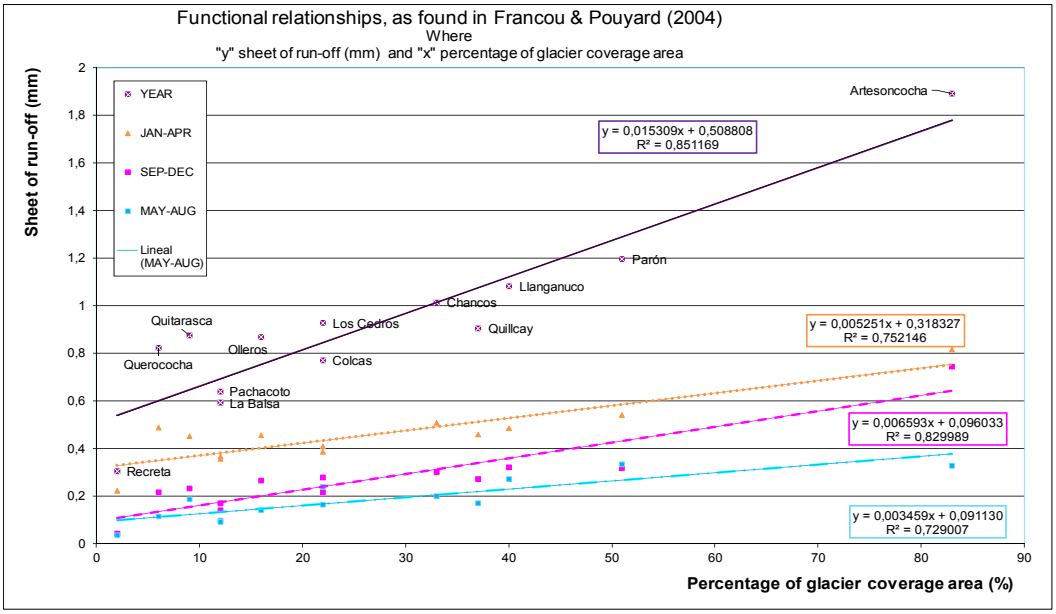

Figure 3. Runoff sheet based on percentage of glacier area, Francou and Pouyard (2004).

Francou and Pouyard (2004) determined functional relationships between the sheet of run-off volume and the percentage of glacier area for the three-quarters of the year, as shown in Figure 3. Their study confirms the following reports:

- A flow variation has been observed since the 1970s, as found in Pouyaud et al. (2002);
- There is a relationship between the re-analysis temperatures above the Cordillera Blanca and the flows in the glacier micro-basins (SENAMHI, 2005; Pouyaud et al., 2002);
- It is possible to predict the evolution of water resources in watersheds by taking advantage of the relationship between sheets of run-off and the percentage of glacier coverage, as found in Pouyaud et al. (2002);
- It is also possible to estimate the date when the water resource will decrease with the expected disappearance of the glaciers, as found in Pouyaud et al. (2002);
- Suárez (2007) made a comparison between the sheet of run-off of all Santa glacier sub-basins and percentage of glaciers (relationship between the glacier area and the total area of the sub-basin) of each sub-basin for three different years (1970, 1991 and 2003), and under different periods linked to different times of the year (wet season, dry season and transition). He found that the glacier contribution is not decisive in the wet season, but in the season of transition the dependence begins to increase and for the dry season a strong influence of the glacier coverage in the runoff is observed.

2.2 Change of the hydrological regime related to the climate change

Another important aspect of climate change is its influence on the hydrological regime change. This effect is due to the snowy mountains characteristic of storing water during the cold season, so that water becomes snow and is stored instead of draining down the soil surface. Thus, glacier basin hydrographs are characterized by having slightly pronounced flood peaks.

During the hot season, there is snow melting contributing to deglaciation, which usually occurs from the beginning of spring and becomes greater as the temperature increases. Fortunately, in Peru this increase does not meet the maximum produced by rainfall which usually occurs in February or March.

As shown in the study by Francou and Pouyard (2004):

- In all basins the maximum contribution is in the four-month period: Sep-Dec, that is, in the spring thaw. It is slightly greater than the warmest four-month period Jan-Apr, which coincides with the rainy season. The lowest contribution is in the four-month period: May-Aug, i.e. in autumn and winter, which is both the period of accumulation and the dry season.
- As can be observed, the greatest loss of the glacier contribution occurs in the spring and summer period, after the period of minimum flows of the basins, so the impact on the production of firm energy is not very great. However, the importance of deglaciation in energy production lies in the loss of water storage in the snowy mountains from early spring to the end of the rainy season and this reduction should be replaced by storage in surface water reservoirs.

This same effect of the contribution by the snow melting is observed throughout the day since it increases in the hours of higher temperature.

Although the described performance is, and always has been, typical of glaciated basins, climate change has a destabilizing effect since at rising temperatures the effects are observed at levels where previously it was possible to have perpetual snows or mountains covered by snow for a very long time.

Having lost the storage capacity, an increase of the flood peaks and a decrease in the water flows are observed.

3 STUDY IN THE SANTA BASIN

In this study, the glacier contribution to the superficial flows in Quitaracsa hydrometric station basin was determined. Figure 4 shows the functional relationship between the glacier surface and time and Figure 5 shows the maps of snowy mountains in the basin and its evolution over time.

Using this expression and taking the year 1962 as the starting point with the measured value, it is estimated that the glacier coverage, following the same climatic conditions, would be zero in the year 2081, that is to say only 19 years after the last period of 50 years that was previously considered.

Using the functional relationships between the glacier coverage and the snowfall contributions, the glacier contribution runoff sheets were calculated for the future years as shown in Table 2. The average annual flow was also calculated, which would be maximum in 1962 and equal to 7,9 m^3 / s.

A decreasing trend of 0,70 m^3/s in a lapse of 50 years is also observed in Table 2. The availability of water and hydro energy production are directly related. Therefore, production of energy will decrease as flow water decreases.

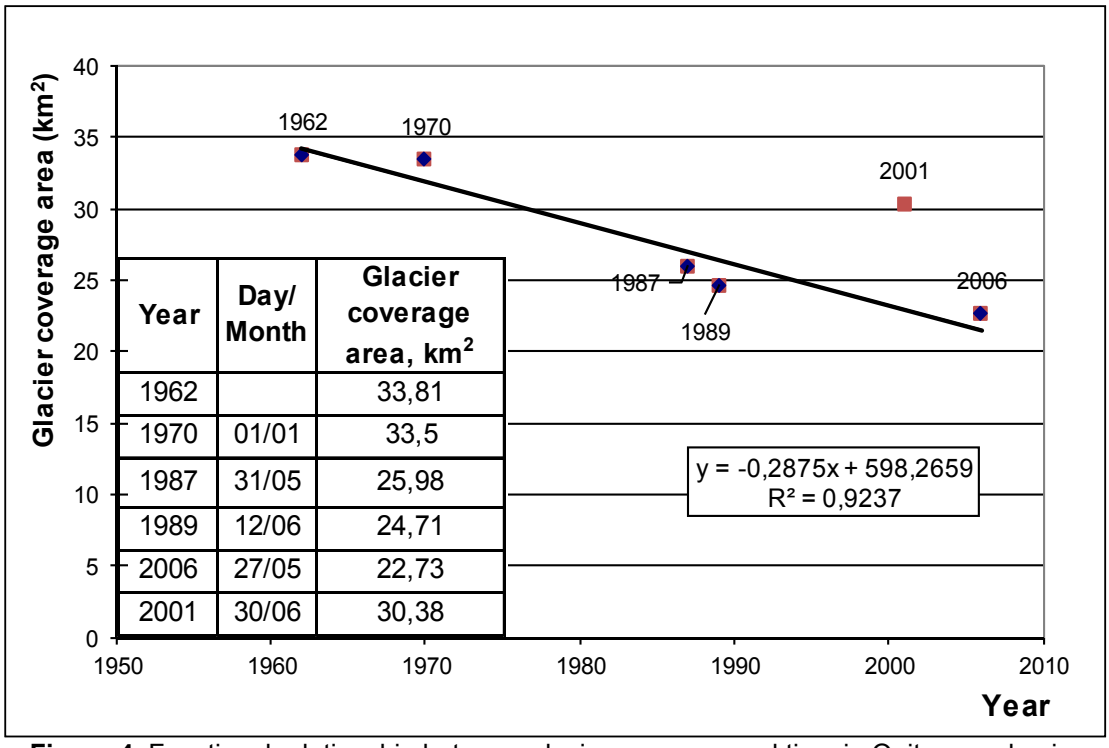

Year	Day/ Month	Glacier coverage area, km²
1962		33,81
1970	01/01	33,5
1987	31/05	25,98
1989	12/06	24,71
2006	27/05	22,73
2001	30/06	30,38

Figure 4. Functional relationship between glacier coverage and time in Quitaracsa basin.

Table 2. Estimated sheets of run-off by glacier contribution in Quitaracsa basin.
Total area of Quitaracsa basin: 385,92 $km^{2.}$

Year	Glacier coverage area km^2	% Glacier coverage area %	Jan-Apr mm	May-Aug mm	Sep-Dec mm	Year mm	Annual Average Flow m^3/s	Variation in 50 years m^3/s
1962	33,81	8,761	4,919	3,121	5,872	13,912	7,868	
2012	19,82	5,135	3,015	1,867	3,481	8,363	7,188	-0,679
2062	5,44	1,410	1,059	0,579	1,026	2,663	6,491	-0,698
2081	0,00	0,000	0,318	0,091	0,096	0,505	6,226	-0,264*

* There is a period only of 19 years

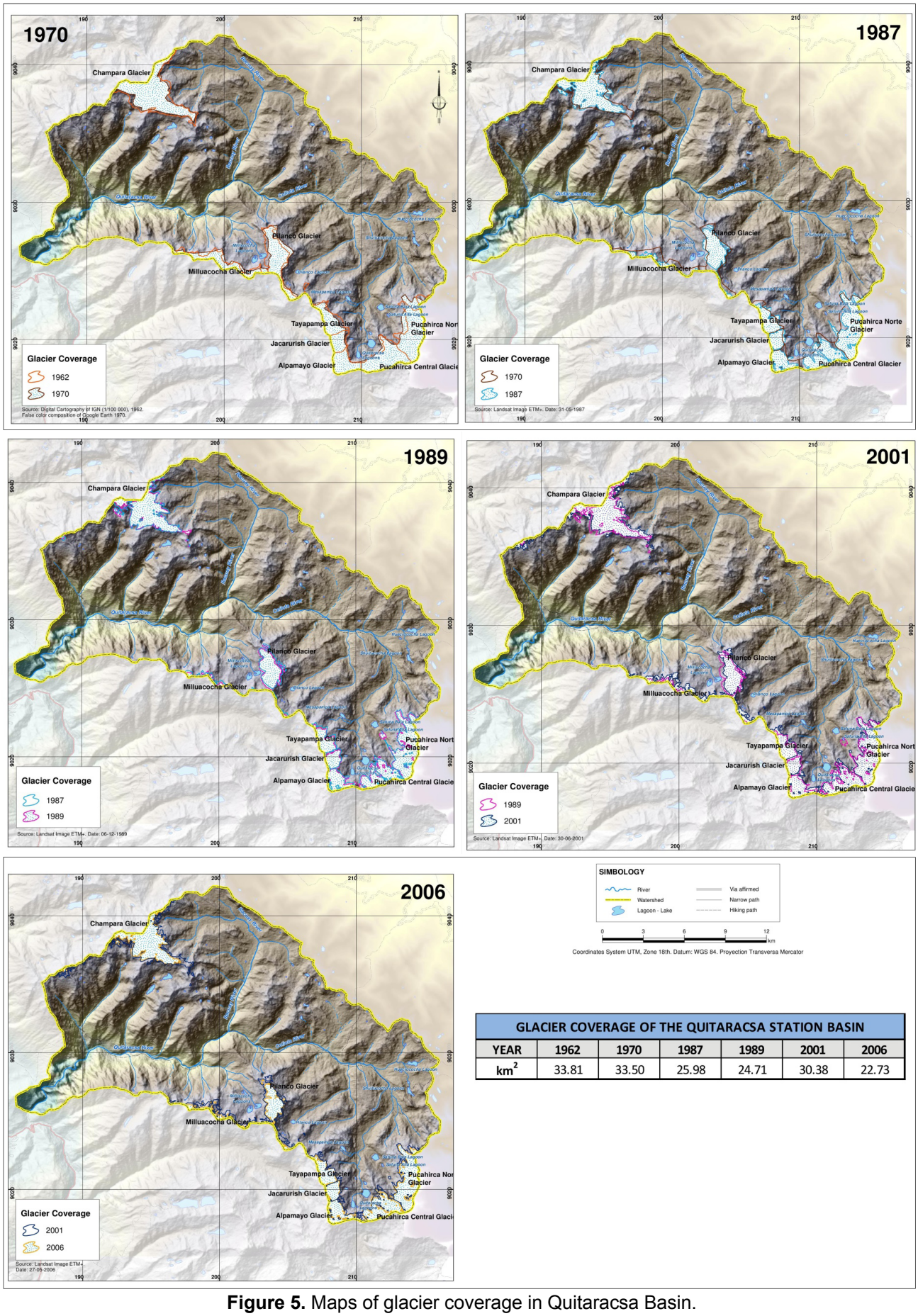

GLACIER COVERAGE OF THE QUITARACSA STATION BASIN						
YEAR	1962	1970	1987	1989	2001	2006
km^2	33.81	33.50	25.98	24.71	30.38	22.73

Figure 5. Maps of glacier coverage in Quitaracsa Basin.

4 STUDY IN THE PATIVILCA BASIN

The area corresponding to the basins of the Huayallapa and Pumarinri rivers was selected as the study area. There is a remarkable decrease in glacier coverage area over time as shown in Figure 6. Figure 7 shows the maps of snowy mountains in the basin and its evolution over time.

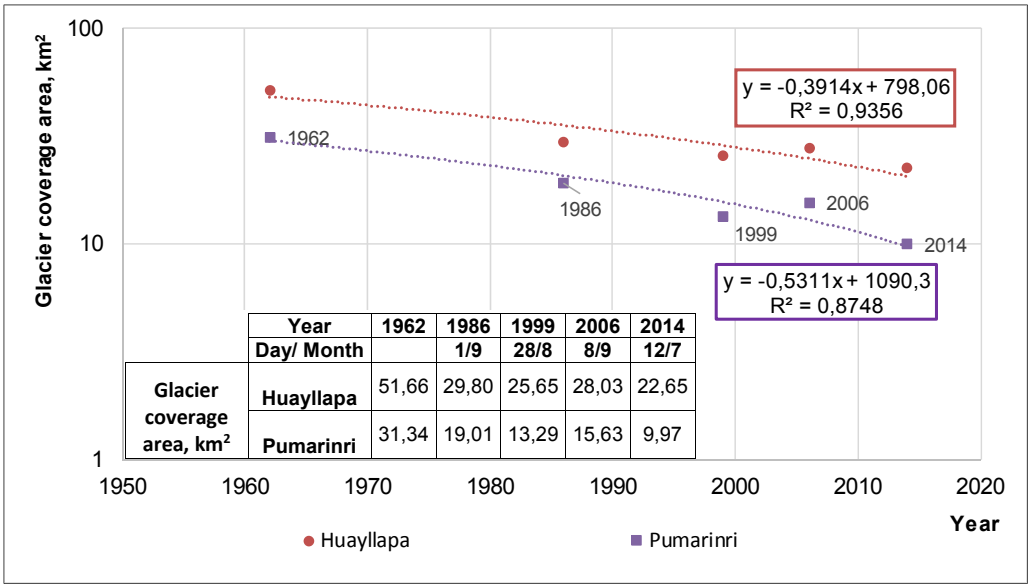

Year		1962	1986	1999	2006	2014
	Day/ Month		1/9	28/8	8/9	12/7
Glacier coverage area, km²	Huayllapa	51,66	29,80	25,65	28,03	22,65
	Pumarinri	31,34	19,01	13,29	15,63	9,97

Figure 6. Glacier coverage vs. time, Huayllapa and Pumarinri Basins.

It can also be seen that in the Huayllapa basin, the glacier coverage loss is lower than in Pumarinri basin which could be due to its highest elevation. When Pumarinri glacier coverage disappears, the Huayllapa glacier coverage will continue to decrease. Using the expression of best fit, the year in which the glacier coverage could disappear was calculated, assuming that the current conditions of climate change remain the same.

In Huayllapa basin, the snowy mountains shall disappear approximately in 2053, while in Pumarinri basin, they shall disappear in 2039.

Using the estimated functional relationships between the glacier coverage area and the sheet of run-off, the glacier contribution sheets of run-off in the selected basins planned for future years were calculated as shown in Table 3.

Table 3. Estimated sheets of run-off by glacier contribution in Pativilca basin.

Year	Glacier coverage area km^2	% Glacier coverage area %	Jan-Apr m	May-Aug m	Sep-Dec m	Year m	Annual Average Flow m^3/s	Variation in 50 Years m^3/s
Total area of Huayllapa basin: 196,02 km^2								
1962	51,66	26,353	14,156	9,207	17,471	40,834	2,539	
2012	21,73	11,084	6,139	3,925	7,404	17,467	1,086	-1,453
2053	0,00	0,000	0,318	0,091	0,096	0,505	0,032	-1,055
Total area of Pumarinri basin: 204,36 km^2								
1962	31,34	15,335	8,370	5,395	10,206	23,972	1,554	
2012	10,56	5,169	3,033	1,879	3,504	8,416	0,546	-1,008
2039	0,00	0,000	0,318	0,091	0,096	0,505	0,033	-0,513

Table 3 shows a decreasing trend that increases proportionally to the area of the basin. In a lapse of 50 years, before disappearing, it is expected an average annual flow decrease of maximum 1,0 m^3/s and 1,4 m^3/s in the Pumarinri and Huayllapa basins, respectively.

The availability of water and hydro energy production are directly related. Therefore, production of energy will decrease as flow water decreases.

5 EFFECT ON THE HYDROPOWER PLANTS

5.1 Historical effects on energy production

In 2009, the Committee on Operations of the National Interconnected System (Comité de Operaciones del Sistema Interconectado Nacional, COES), through the Subcommittee on Generators, commissioned the

study "Analysis of historical series of flows used for the hydroelectric production of Peru." Historical series from the period 1954-1955 to 2007-2008 of 13 hydrometric stations representing the available flow of the main

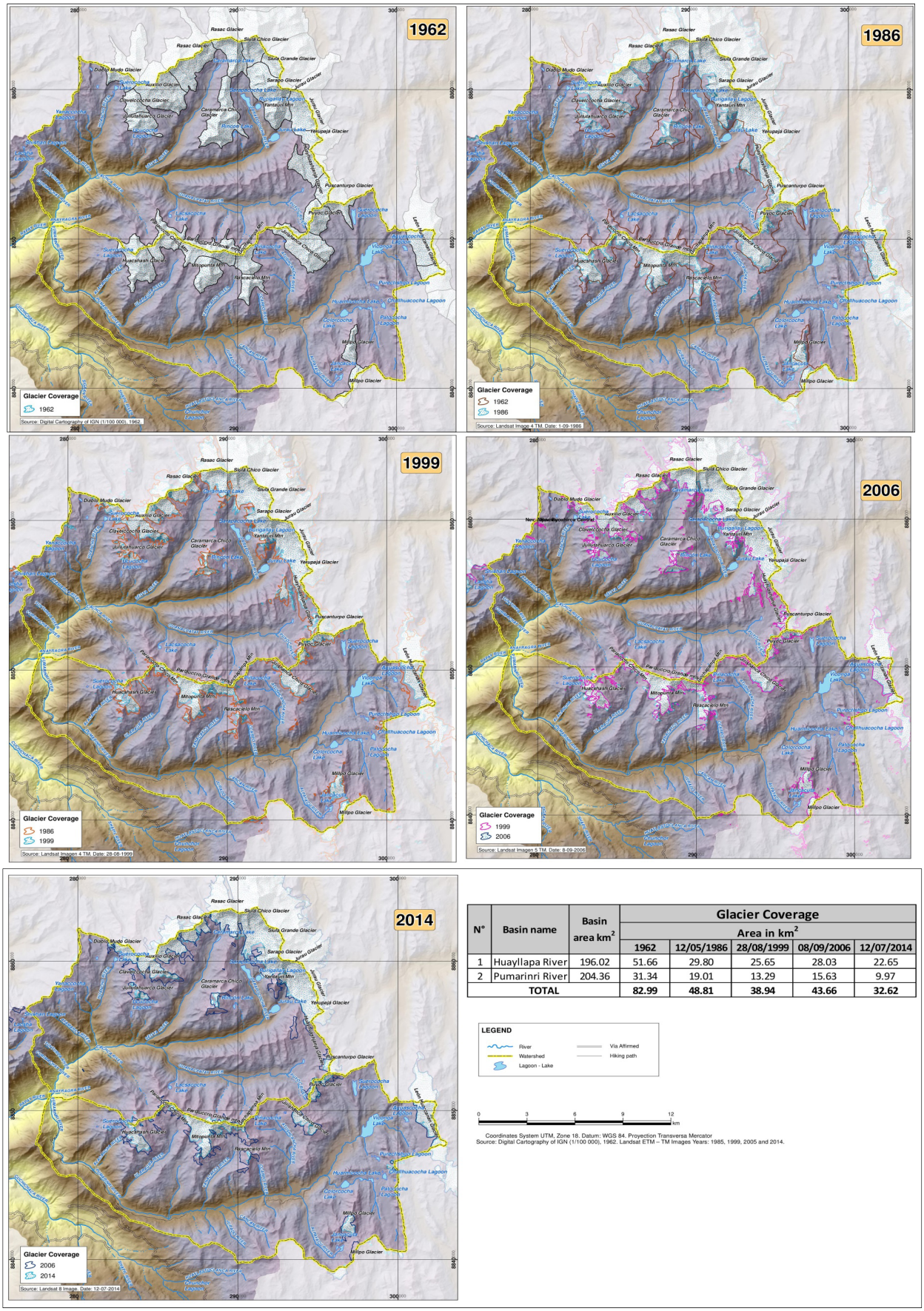

N°	Basin name	Basin area km²	Glacier Coverage Area in km²				
			1962	12/05/1986	28/08/1999	08/09/2006	12/07/2014
1	Huayllapa River	196.02	51.66	29.80	25.65	28.03	22.65
2	Pumarinri River	204.36	31.34	19.01	13.29	15.63	9.97
TOTAL			82.99	48.81	38.94	43.66	32.62

Figure 7. Maps of glacier coverage (Cobertura glaciar) of the Huayllapa and Pumarinri Basins.

power plants of the National Interconnected Electrical System were reviewed; the results for the Santa and Pativilca basins are summarized below, as found in Suárez (2009):

- For the Santa basin, the sum of the flow rates measured in the Las Balsas and Cedros hydrometric stations was selected. This sum represents the available flow rate for the Cañón del Pato hydroelectric plant. For the Pativilca basin, the Cahua station was selected, which represents the available water flow for Cahua hydroelectric plant;
- Analysis of the statistical characteristics shows that in the Pacific basin the Santa river has the highest average flow and there are strong variabilities in its monthly and annual flows. In the Santa and Pativilca basins, the monthly maximum flows are observed in the autumn. In general, the rivers located in the northern and southern part of the Pacific slope show the greatest variability, which may be associated with the El Niño phenomenon in the northern part and the intermittent character of the flows in the southern zone;
- From the analysis of independence of the series and ruptures, it can be seen that all series analyzed are random. There are mainly negative ruptures and mainly in the 1980s. In the case of the Pativilca basin, there are ruptures in the maximum flows in September, October and November (SON) while in the Santa basin in the minimum flows, June, July and August (JJA);
- Analysis of trends using parametric and non-parametric methods with a significance level of 95% shows that the Santa basin has negative trends in the flows of SON and JJA, as well as the minimum flows. In the Pativilca basin, negative trends are observed in the average flow, in the flows of SON and March, April and May (MAM) and the maximum flow;
- The conclusions explain that the temporal variations in the observed flows occur mainly in the period 1987-1992, which may be due to climatic factors or external factors (naturalized flows or synthetic series).

5.2 Decrease in hydroenergy production due to reduction of the glacier area

The hydroelectric power produced by the hydroelectric plant is a function of the available flow rate for the power plant, as well as the characteristics of the topographic difference and the electromechanical equipment. Other factors, such as ecological flow, minimum and maximum flow rates and addition, if any, of the basin's daily and/or seasonal regulation conditions, should be considered.

It is possible to calculate the energy difference produced according to the historical conditions of a stationary hydrological series and according to the hydrological series derived from the decrease of the glacier coverage. The availability of water and hydroenergy production are directly related. Therefore, production of energy will decrease the flow water decreases.

5.3 Analysis of future climate change scenarios

In order to explain the effect of future scenarios of climate change on energy production, the document "The Economics of Climate Change in Peru - Synesthesia", by the Inter-American Development Bank and ECLAC, Economic Commission for Latin America, was revised. The analysis of the hydropower sector was based on the research "The economics of climate change in Peru: hydroenergy" whose authors are Homero Miranda Coll-Cárdenas and Carlos Alberto Arnillas. Their results are summarized below, as found in BID (2016); Miranda and Arnillas, (2014):

- The study analyzed the impact of climate change by measuring the reduction of revenues from the hydropower market through the variation of electricity production for each of the most relevant hydroelectric plants in the National Interconnected System (SINAC) in three climatic scenarios until the year 2100;
- 16 hydroelectric plants were selected, representing approximately 85% of installed hydropower capacity. The Pato Canyon hydroelectric plant located in the Santa basin is the second most important while Cahua hydroelectric plant located in the Pativilca basin is in the 13th position;
- The rate of increase in hydroelectric energy production in the period 1990 to 2011 is 5,3%, which indicates the importance of the sector;
- A loss of 5% of the sectoral GDP is observed at the year 2100 in contrast to the 0,10% of the national GDP at the year 2010;
- Accumulated costs reveal losses in all climate scenarios analyzed;
- A lower hydroelectricity production due to lower availability of water in watersheds is observed;
- Even without climate change, hydroelectricity production would tend to decrease due to the expansion of agriculture.

It should be noted that the effects of the climate change analyzed are not only associated with deglaciation, which is not significant in all 16 hydroelectric plants studied, but also with the occurrence of the El Niño phenomenon and the decrease of precipitation associated with the increase in temperatures, among others reasons.

In addition, to explain the effects of climate change on energy production, SENAMHI (2005) proposes to establish a relationship between the temperatures in 500 hPa calculated with the different climatic scenarios

and the sheets of run-off. Pouyaud et al. (2005) showed that this relationship has significance and can be used to determine projected sheets of run-off for different climatic scenarios.

Also, it would be possible to establish a relationship between the reduction of glacier coverage and temperatures at 500 hPa.

6 CONCLUSIONS

- The influence of climate change on the basin was reiterated, which is clearly evident in the decrease in glacier coverage and the continuous increase in temperature;
- Deglaciation will affect the water availability of the project. The greatest impact will be in the spring and summer months, i.e. after the period of minimum flows;
- Glacier coverage reduction effect, due to its water storage capacity, has been and will also be observed in the hydrological regime of the rivers, causing an increase of the flood peaks in wet season and a decrease in the flows of dry season;
- The glacier coverage in Quitaracsa basin could be null in the year 2081, assuming that the current conditions of climate change would remain the same;
- The contribution to the annual average flow of Quitaracsa basin is estimated to be reduced, with a maximum calculated value of 0,7 m3 / s in a lapse of 50 years;
- In the Huayllapa basin the glacier coverage will disappear in about 2053, while in the Pumarinri basin it will do so in 2039, assuming that the current conditions of climate change would remain the same;
- In a lapse of 50 years, a maximum reduction of the contribution to the average annual flow of 1,0 m^3/s and 1,4 m^3/s in the Pumarinri and Huayllapa basins, respectively, is foreseen;
- The availability of water and hydro energy production are directly related. Therefore, production of energy will decrease as flow water decreases;
- The effect of climate change on water availability occurs not only due to deglaciation but also other factors such as the occurrence of the El Niño phenomenon, the decrease in temperatures, the increase in agricultural areas, and the construction of storage infrastructure. All this together makes it difficult to study the effect of deglaciation in particular;
- It is necessary to establish a relationship between the temperature of 500 hPa and deglaciation to evaluate the effect of different climatic scenarios on the production of hydroelectric power.

ACKNOWLEDGEMENTS

Thanks to the consulting company CESEL S.A. in the Hydraulic and Irrigation Management, for allowing me to be part of the study groups in different studies of hydroelectric power plants in which the concepts developed in this publication were reviewed and applied.

The author would like to thank the engineers, Nancy Reyes and Fernando Dávila for determining the areas of glacier coverage in the watersheds studied using the GIS.

REFERENCES

BID (2016). *La economía del cambio climático en el Perú*: Impactos en el Sector Hidroenergía, Banco Interamericano de Desarrollo, Comisión Económica para América Latina, Ministerios del Ambiente, de Economía y Finanzas y de Relaciones Exteriores del Perú, 1-152.

Francou B. & Pouyaud B. (2004). Métodos de observación de glaciares de los Andes Tropicales. Mediciones de terreno y procesamiento de datos. Versión I. IRDI-HH-INAMHI-INRENA-SENAMHI-EMAAPQ-INGEOMINASLGEE.

IPCC, Intergovernmental Panel on Climate Change, (2007). *Climate Change 2007*, Impacts, Adaptation and Vulnerability. Cambridge University Press, 1-13.

Miranda H. and Arnillas C. (2014). *La economía del cambio climático en el Perú*: hidroenergía en el Documento: La economía del Cambio Climático en el Perú- Sintésis, Banco Interamericano de Desarrollo y Comisión Económica para América Latina, 1-152.

Pouyaud B., Yerren J., Zapata M. et al. (2002). Glaciares y Recursos Hídricos en la Cuenca del río Santa. *INRENA*, 1-14.

SENAMHI (2005) Escenarios Climáticos Futuros y disponibilidad del recurso hídrico en la cuenca del río Santa. *CONAM*, 1-11.

Suárez W. (2007), Le bassin versant du fleuve Santa (Andes du Pérou): dynamique des écoulements en contexte glacio-pluvio-nival. *Thèse de doctorat*, de l'Universite Montpellier II Sciences et Techniques du Languedoc.

Suárez W. (2009). Análisis de series históricas de caudales utilizados para la producción hidro energética del Perú. Subcomité de Generadores del Comité de Operaciones del Sistema Interconectado Nacional, (COES).

